

Titre: River ice tracking and velocity estimation using remote sensing
Title: method and numerical modelling

Auteur: Farnaz Samsamipour
Author:

Date: 2022

Type: Mémoire ou thèse / Dissertation or Thesis

Référence: Samsamipour, F. (2022). River ice tracking and velocity estimation using remote
Citation: sensing method and numerical modelling [Master's thesis, Polytechnique
Montréal]. PolyPublie. <https://publications.polymtl.ca/10317/>

 **Document en libre accès dans PolyPublie**
Open Access document in PolyPublie

URL de PolyPublie: <https://publications.polymtl.ca/10317/>
PolyPublie URL:

**Directeurs de
recherche:** Ahmad Shakibaeinia
Advisors:

Programme: Génie civil
Program:

POLYTECHNIQUE MONTRÉAL

affiliée à l'Université de Montréal

**River ice tracking and velocity estimation using remote sensing method and
numerical modelling**

FARNAZ SAMSAMIPOUR

Département des génies civil, géologique et des mines

Mémoire présenté en vue de l'obtention du diplôme de *Maîtrise ès sciences appliquées*

Génie Civil

Mai 2022

POLYTECHNIQUE MONTRÉAL

affiliée à l'Université de Montréal

Ce mémoire intitulé:

River ice tracking and velocity estimation using remote sensing method and numerical modelling

Présenté par **Farnaz SAMSAMIPOUR**

en vue de l'obtention du diplôme de *Maîtrise ès sciences appliquées*

a été dûment accepté par le jury d'examen constitué de :

Elmira HASSANZADEH, présidente

Ahmad SHAKIBAEINIA, membre et directeur de recherche

Tew-Fik MAHDI, membre

DEDICATION

To my parents Zahra and Ali, and my beloved brother Mohammad Mahdi.

For their love and unlimited support.

RÉSUMÉ

En raison du temps très froid au Canada, les rivières gèlent pendant les saisons froides et des banquises apparaissent à la surface de la rivière, ce qui modifiera les principes hydrauliques de la rivière. Les rivières gelées affectent considérablement l'environnement et l'économie, par exemple en endommageant les infrastructures hydrauliques, et elles causent des pertes financières de millions de dollars par an.

Un paramètre clé pour déterminer le rôle des banquises dans l'hydrodynamique des rivières est leur vitesse. La quantification du mouvement de ces banquises peut fournir une opportunité unique d'estimer la vitesse d'écoulement des rivières pour compléter ou remplacer les mesures in situ, qui sont coûteuses et souvent difficiles, en particulier en présence de glace. Par conséquent, pour quantifier le mouvement des banquises, des images satellites quasi-simultanées peuvent être utilisées.

Les données d'imagerie satellitaire ont reçu beaucoup d'attention dans différentes spécialités ces dernières années. La technique de télédétection s'est avérée utile pour détecter les banquises à la surface de la rivière. Le déplacement des banquises peut être fourni en les suivant dans des images satellites quasi simultanées. Ici, nous analysons des paires d'images quasi simultanées co-enregistrées à partir d'acquisitions stéréo du capteur satellite GEOEYE-1 avec une résolution d'imagerie spatiale de 0,5 m obtenue auprès de la société Maxar. Un algorithme de corrélation d'images est nécessaire pour suivre les banquises dans deux images séquentielles. Nous utilisons le logiciel Correlation Image Analysis (CIAS) pour quantifier les déplacements des banquises dans la section inférieure de la rivière Athabasca (LAR) en Alberta, au Canada, le 11 Novembre 2009. Ici, en supposant que les champs de vitesse de la glace et de l'eau sont similaires, nous estimer la vitesse de la rivière pour différentes sections transversales de la rivière.

La modélisation numérique est un autre moyen d'estimer efficacement les caractéristiques du débit fluvial, y compris la vitesse moyenne en profondeur dans la recherche et l'ingénierie fluviales. Le modèle numérique de cette étude est Delft-3D, et il a d'abord été calibré et validé à l'aide des mesures de terrain disponibles. Le modèle a été calibré par le coefficient de Manning. Cette valeur a déjà été mesurée pour la rivière Athabasca dans différents tronçons. Puisqu'il n'y a pas de données mesurées pour le moment où nous étudions la rivière, les données mesurées disponibles (profondeur_vitesse moyenne et niveau d'eau) pour Septembre 2004 ont été utilisées comme source

Les résultats révèlent que les champs de vitesse du suivi de mouvement et de la modélisation numérique concordent généralement, en particulier dans les sections rectilignes de la rivière lorsque les banquises se déplacent sans aucune restriction. Néanmoins, des écarts locaux sont observés, en particulier dans les zones à forte accélération/décélération et agrégation de glace (lorsqu'il y a une restriction de mouvement).

ABSTRACT

Due to the severe cold weather in Canada, rivers experience freezing in cold seasons, and ice floes appear on the river's surface, which will change the hydraulic principles of the river. Frozen rivers significantly affect the environment and the economy, for instance, by damaging the hydraulic infrastructures, and they cause financial loss of millions of dollars yearly.

A key parameter to determine the role of ice floes in river hydrodynamics is their velocity. Quantifying the movement of these ice floes can provide a unique opportunity to estimate river flow velocity to complete or replace in-situ measurements, which are costly and often challenging, especially in the presence of ice. Therefore, to quantify the movement of ice floes, near-simultaneous satellite images can be used.

Satellite imagery data have received much attention in different specialties in recent years. The Remote-Sensing technique has been found to be useful in detecting ice floes on the river's surface. The displacement of ice floes can be provided by tracking them in near-simultaneous satellite images. Here, we analyze co-registered near-simultaneous image pairs from stereo acquisitions of the GEOEYE-1 satellite sensor with a spatial imaging resolution of 0.5 m obtained from the Maxar Company. An image correlation algorithm is needed to track ice floes in two sequential images. We use the Correlation Image Analysis software (CIAS) to quantify the ice floes' displacements in the Lower Athabasca River (LAR) section in Alberta, Canada on 11 November 2009. Here, by assuming that the ice and water velocity fields are similar, we estimate the river velocity for different river cross-sections.

Numerical modelling is another way to estimate river flow characteristics effectively, including the depth-averaged velocity in fluvial research and engineering. The numerical model of this study is Delft-3D, and it has been first calibrated and validated using the available field measurements. The model has been calibrated by the manning coefficient. This value has been already measured for the Athabasca River in different reaches. Since there is no measured data for the time that we study the river, the available measured data (depth_averaged velocity and water level) for September 2004 has been used as a source for evaluating the functionality of the model. Finally, the velocity fields quantified through image processing are compared to those from a 2D depth-averaged numerical model to assess the feasibility and limitations of water velocity computation from the movement of ice floes.

The results reveal that the velocity fields from motion tracking and numerical modelling generally agree, especially in straight river sections when ice floes move without any restriction. Nevertheless, local discrepancies are observed, particularly in areas with strong acceleration/deceleration and ice aggregation (when there is a restriction in movement).

TABLE OF CONTENTS

DEDICATION	III
RÉSUMÉ.....	IV
ABSTRACT	VI
TABLE OF CONTENTS	VIII
LIST OF TABLES	X
LIST OF FIGURES.....	XII
LIST OF SYMBOLS AND ABBREVIATIONS.....	XVI
LIST OF APPENDICES	XVII
CHAPTER 1 INTRODUCTION.....	1
1.1 Context and Motivation.....	1
1.2 Study Area: Lower Athabasca River.....	4
CHAPTER 2 LITERATURE REVIEW	7
2.1 Motion tracking using image processing	7
2.2 Remote Sensing.....	8
2.3 Hydraulic Model	11
2.4 Problems and Research objectives	12
2.5 Structure of the thesis	13
CHAPTER 3 METHODOLOGY	14
3.1 Remote Sensing.....	14
3.1.1 Acquisition of the imagery data	14
3.1.2 Motion detection algorithm in images	18
3.1.3 Image pre-processing	19
3.1.4 Implementation.....	23

3.2	Hydraulic Model	30
3.2.1	Governing equations	30
3.2.2	Bathymetry and topography data	31
3.2.3	Model settings	32
CHAPTER 4	RESULTS CALIBRATION, VALIDATION, AND EVALUATION	41
4.1	Hydraulic model	41
4.1.1	Calibrating Delft3D hydraulic model.....	41
4.1.2	Validating Delft3D hydraulic model with collected water level and depth-averaged velocity data	41
4.1.3	Reynolds number calculation	45
4.1.4	Converting the depth-averaged velocity to water surface velocity	47
4.2	Remote sensing	50
4.2.1	Dry surface	50
4.2.2	Error elimination	50
4.2.3	Smoothing the results	55
4.3	Result comparison	56
4.3.1	Comparing the results in different cross-sections	56
4.4	Conclusion.....	78
CHAPTER 5	CONCLUSION AND RECOMMANDATIONS	79
5.1	Conclusion.....	79
5.2	Discussion	80
5.3	Future work	81
REFERENCES.....		82
APPENDICES.....		88

LIST OF TABLES

Table 1.1 Geographical information of the main tributaries in the LAR (Data collected from WSC).	5
Table 3.1 Characteristics of the obtained images from Maxar company on 11 November 2009. .	15
Table 3.2 Product MBR (Minimum Bounding Rectangle) Geographical Coordinates (the maximum extents of the image).	15
Table 3.3 The values of MRT by using different co-registration algorithms.	21
Table 3.4 The RMSE values measured by comparing the results of CIAS with the operator- measured movements for different search area sizes and reference block sizes (Sensitivity Analysis).....	27
Table 3.5 The mean value and standard deviation of the C_{\max} for different reference block sizes and search area sizes.	28
Table 3.6 Time frame of the model. The river has been simulated for one week and our study day is in the middle of this week.....	36
Table 3.7 Boundary Condition for Downstream.	38
Table 3.8 Boundary Condition for Upstream.	38
Table 3.9 The type and location of the Boundary Conditions in upstream and downstream.	38
Table 3.10 The Athabasca River's bed roughness characteristics.	39
Table 3.11 The flow on the start and end date of the simulation for main Athabasca River tributaries.....	40
Table 4.1 The hydrometric data obtained from the WSC as a boundary condition for downstream (from 13 September 2004 to 18 September 2004).	42
Table 4.2 The hydrometric data obtained from the WSC as a boundary condition for upstream (from 13 September 2004 to 18 September 2004).	42
Table 4.3 The hydrometric data for the main tributaries of the Athabasca River (from 13 September 2004 to 18 September 2004).	42

Table 4.4 Physical Parameters of the water for measuring the Reynolds number.....	46
Table 4.5 Reynolds number for different types of flow regimes in open channel flow.....	46

LIST OF FIGURES

Figure 1.1 Examples of river ice. a) Peace River, Alberta in early March 2016 (image source: [3]). b) Mackenzie River at Inuvik, NWT in May 2008 (image source: [4]).....	1
Figure 1.2 Example of river ice. Ice pans near the Dunvegan Bridge on the Peace River, Alberta (image source: [5]).	2
Figure 1.3 a) Athabasca River Basin located in the province of Alberta, Canada [30]. b) The extent of the simulated river. c) The extent of the river with available satellite imagery.....	6
Figure 3.1 GeoEye-1 collection modes. The sensor takes simultaneous panchromatic (0.5 m resolution) and multispectral (1.84 m resolution) images in 15.2 km swaths.....	17
Figure 3.2 Motion estimation using block matching algorithm.	18
Figure 3.3 The location of two tie points in the reference image (GCP #1 and #2).	22
Figure 3.4 The location of the tie points in the unregistered image (GCP #1 and #2).....	22
Figure 3.5 The location of two ice floes #230 and #231 a) in the reference image and b) in the target image. The distance between the location of points in the first and second image shows ice floes' movements.	26
Figure 3.6 High-resolution computational grids (coarse grid: 75 m x 75 m).....	33
Figure 3.7 Staggered grid in DELFT3D-FLOW	34
Figure 3.8 Grids and bathymetry data imported in QUICKIN before (upper image) and after triangulate interpolation (lower image). The lower image demonstrates the bathymetry in main channel and flood plain.	35
Figure 4.1 Validation of the Delft3D hydraulic model with collected water level and velocity data for the cross-section 01 in September 2004.	43
Figure 4.2 Validation of the Delft3D hydraulic model with collected water level and velocity data for the cross-section 03 in September 2004.	43
Figure 4.3 Validation of the Delft3D hydraulic model with collected water level and velocity data for the cross-section 05 in September 2004.	44

Figure 4.4 Validation of the Delft3D hydraulic model with collected water level and velocity data for the cross-section 07 in September 2004.	44
Figure 4.5 Velocity profile in open channel flow.	47
Figure 4.6 The movement value of the ice floe obtained by the CIAS plotted against the expected movement value of the ice floe obtained manually for the points with $C_{max} > 0.6$	52
Figure 4.7 The movement value of the ice floe obtained by the CIAS plotted against the expected movement value of the ice floe obtained manually for the points with $SNR > 15$	53
Figure 4.8 The movement value of the ice floe obtained by the CIAS plotted against the expected movement value of the ice floe obtained manually for the points with $dif > 0.6$	54
Figure 4.10 Velocity values (m/s) were obtained from a) the numerical model (DELFT3D), and b) the remote sensing method (CIAS).	55
Figure 4.11 Simulated water level and comparison of simulated and measured surface water velocity in Cross-Section 2.	57
Figure 4.12 Simulated water level and comparison of simulated and measured surface water velocity in Cross-Section 3.	57
Figure 4.13 Satellite image (cross-section 2 and 3: $Y=6312072.5$ and $Y=6312297.5$)	58
Figure 4.14 Velocity of the river obtained by remote sensing method (cross-section 2 and cross-section3).	58
Figure 4.15 Simulated water level and comparison of simulated and measured surface water velocity in Cross-Section 4.	59
Figure 4.16 Satellite image for cross-section 4: $Y=6314147.5$	59
Figure 4.17 Velocity of the river obtained by remote sensing method (cross-section 4).	60
Figure 4.18 Simulated water level and comparison of simulated and measured surface water velocity in Cross-Section 1.	61
Figure 4.19 Satellite image for cross-section 1: $Y=6308972.5$	61
Figure 4.20 Velocity of the river obtained by remote sensing method (cross-section 1).	62

Figure 4.21 Simulated water level and comparison of simulated and measured surface water velocity in Cross-Section 5.	63
Figure 4.22 Satellite image for cross-section 5: Y=6316747.5.....	63
Figure 4.23 Velocity of the river obtained by remote sensing method (cross-section 5).	64
Figure 4.24 Simulated water level and comparison of simulated and measured surface water velocity in Cross-Section 6.	65
Figure 4.25 Satellite image for cross-section 6: Y=6316997.5.....	65
Figure 4.26 Velocity of the river obtained by remote sensing method (cross-section 6).	66
Figure 4.27 Simulated water level and comparison of simulated and measured surface water velocity in Cross-Section 7.	67
Figure 4.28 Satellite image for cross-section 7: Y=6318822.5.....	67
Figure 4.29 Velocity of the river obtained by remote sensing method (cross-section 7).	68
Figure 4.30 Simulated water level and comparison of simulated and measured surface water velocity in Cross-Section 8.	69
Figure 4.31 Satellite image for cross-section 8: Y=6319072.5.....	69
Figure 4.32 Velocity of the river obtained by remote sensing method (cross-section 8).	70
Figure 4.33 Simulated water level and comparison of simulated and measured surface water velocity in Cross-Section 9.	71
Figure 4.34 Satellite image for cross-section 9: Y=6319722.5.....	71
Figure 4.35 Velocity of the river obtained by remote sensing method (cross-section 9).	72
Figure 4.36 Simulated water level and comparison of simulated and measured surface water velocity in Cross-Section 10.	73
Figure 4.37 Satellite image for cross-section 10: Y=6320997.5.....	73
Figure 4.38 Velocity of the river obtained by remote sensing method (cross-section 10).	74
Figure 4.39 Simulated water level and comparison of simulated and measured surface water velocity in Cross-Section 11.	75

Figure 4.40 Satellite image for cross-section 11: $Y=6322097.5$	75
Figure 4.41 Velocity of the river obtained by remote sensing method (cross-section 11).	76
Figure 4.42 Simulated water level and comparison of simulated and measured surface water velocity in Cross-Section 12.	77
Figure 4.43 Satellite image for cross-section 12: $Y=6322372.5$	77
Figure 4.44 Velocity of the river obtained by remote sensing method (cross-section 12).	78
Figure A.1 Section of the Athabasca River in the reference image. The yellow rectangle shows the object which will be detected and compared after applying different co-registration methods on the target image with this reference image.....	89
Figure A.2 Comparison between the Reference Image and Georeferenced image (co-registration method: Linear).	90
Figure A.3 Comparison between the Reference Image and Georeferenced image (co-registration method: Helmert).	90
Figure A.4 Comparison between the Reference Image and Georeferenced image (co-registration method: Third-Order Polynomial).	91
Figure A.5 Comparison between the Reference Image and Georeferenced image (co-registration method: TPS).....	91
Figure A.6 Comparison between the Reference Image and Georeferenced image (co-registration method: Projective).	92
Figure B.1 Sample of the dry surface on the left side of the section.	93
Figure B.2 Sample of the dry surface in the middle of the section.	93
Figure C.1 Captured satellite images from a section of the Lower Athabasca River from Maxar company for a) 21 July 2009, b) 01 September 2009, and c) 11 November 2009.....	94

LIST OF SYMBOLS AND ABBREVIATIONS

1D	One-Dimensional
2D	Two-Dimensional
3D	Three-Dimensional
ADV	Acoustic Doppler Velocimetry
Air SAR	Airborne Along-Track Interferometric SAR images
ASERD	Alberta Environment and Sustainable Resources Development
ASTER	Advanced Spaceborne Thermal Emission and Reflectance Radiometer
ATI	Along-Track Interferometric
AT-InSAR	Along Track Synthetic Aperture Radar interferometry
BMA	Block Matching Algorithm
C_{avg}	Maximum Correlation Coefficient
C_{max}	Maximum Correlation Coefficient
CHP	Check Point
CIAS	Correlation Image Analysis Software
DEM	Digital Elevation Model
DHI	Danish Hydraulic Institute
DOQs	Digital Orthophoto Quadrangles
EFDC	Environmental Fluid Dynamic Code
FDM	Finite Difference Method
FEM	Finite Element Method
FVM	Finite Volume Method
GCP	Ground Control Point
HEC-RAS	Hydrological Engineering Center's River Analysis System
LS-PIV	Large Scale Particle Image Velocimetry
MRT	Mean Residual Total
n_b	Bottom Roughness
NCC	Normalized Cross-Correlation
NCC-O	Orientation Correlation
NDOP	National Digital Orthophoto
PAD	Peace Athabasca Delta
PDE	Partial Differential Equations
PIV	Particle Image Velocimetry
PRISM	Panchromatic Remote-sensing Instrument for Stereo Mapping
R_h	Hydraulic Radius
RAMP	Regional Aquatics Monitoring Program
RMSE	Root Mean Square Error
SAR	Synthetic Aperture Radar
SNR	Signal to Noise Ratio
SPOT	Satellite pour l'Observation de la Terre
SSC	Suspended Sediment Concentration
TPS	Thin Plate Spline
WSC	Water Survey of Canada

LIST OF APPENDICES

Appendix A	Comparing different georeferencing methods.....	88
Appendix B	Dry surfaces	93
Appendix C	Section of the LAR in three different times of the year.....	94

CHAPTER 1 INTRODUCTION

1.1 Context and Motivation

Almost 75 percent of the earth's surface is covered by water in environments like rivers, lakes, seas, and oceans. Hydraulic investigation of these environments is demanded to understand their behaviour. One of the vital influential conditions on these hydro systems is the weather condition which is different worldwide. As much as the geographical location of a hydro-system becomes closer to the pole, the weather becomes colder (e.g., northern hemisphere). In northern sections of Canada, severe cold weather is dominant for an extended period. This low temperature, especially in the cold seasons, causes the water to be frozen. Therefore, in the upper locations, the surface of the Canadian rivers freezes for the entire cold season. The Athabasca River is located in Alberta, Canada is an example of a river with a high possibility to be frozen. For instance, in the years (from 1976 to 2005), Fort McMurray had 118.1 icing days (the temperature is less than 0 degrees on icing days [1]), and the freeze-thaw cycle took 71.7 days in a year [2]. Some river ice is visible in the following figures (Figure 1.1 and Figure 1.2).

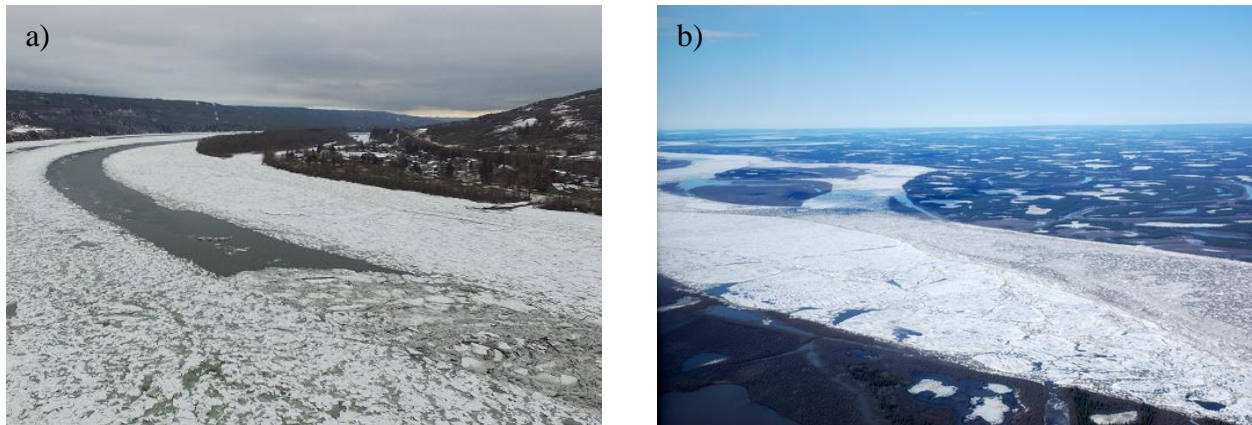


Figure 1.1 Examples of river ice. a) Peace River, Alberta in early March 2016 (image source: [3]). b) Mackenzie River at Inuvik, NWT in May 2008 (image source: [4]).



Figure 1.2 Example of river ice. Ice pans near the Dunvegan Bridge on the Peace River, Alberta (image source: [5]).

Studies showed strong, substantial linkages and sensitivity between changes in climatic circumstances and the entire ice regime [6]. Like open-water situations, river ice is an important part of the cold-climate hydrological cycle, and its phenology impacts both natural and human processes [7]. Ice floes can damage hydraulic infrastructures such as bridges or dams, and they can threaten the riverside communities [8] [9]. Studies showed that ice jams (when ice floes are obstructed, and it begins to accumulate behind an obstacle [7]) could be considered as a primary cause of floods by increasing the water level, especially in warm seasons [10] in areas like McKenzie Delta, NWT or Peace-Athabasca Delta, Alberta [11] [12] [13]. Flood risk management and water resource management need constant monitoring of essential hydrological factors other than water levels, such as flow velocity and flow charge [14]. Flow velocity significantly impacts fluxes, erosion, transport, and deposition of sediments in the river [15].

Traditionally, there are two ways to understand a hydro system:

- 1) Physical modelling and field measurements
- 2) Numerical modelling

The first method is costly, some conditions are uncontrolled, and there are flexibility issues. For instance, extreme weather events and climate change have made the conventional in-situ monitoring to measure the flow velocity (e.g., in situ measurement) challenging [16]. However, these methods can provide a high-resolution 3D water velocity [17], they are time-consuming, expensive, and need experts to be present in the field, and the improvement possibility is poor [18].

The second approach in fluvial research and engineering to effectively estimate river flow characteristics, including water surface velocity, and water depth, is simulating the flow using a numerical modelling [19]. This method is cost-effective, controlled, and flexible. The technique can continuously give a spatially and temporally river velocity estimation, yet it needs some field measurements to simulate the river properly.

Another approach to avoid field measurements completely where collecting ground-based data is problematic is the Remote Sensing monitoring [20], which has received much attention in recent years in hydraulic and hydrology to explore parameters such as water-surface width, slope, and elevation [21], and surface storage and river discharge [22]. Since it is almost impossible to do the in-situ flow velocity measurement (surface water dynamic) in the presence of ice, Remote Sensing monitoring can turn this ice presence to advantage and measure the water-surface velocity remotely [15] [23] [16].

In this study, the reliability of using Remote Sensing to estimate flow velocity in different cross-sections with different morphology and ice conditions of the Lower Athabasca River will be examined compared to real and simulated data. However, the existence of the ice can have significant effects on flow and geomorphic processes [24].

1.2 Study Area: Lower Athabasca River

The Athabasca River is an important river located in Alberta, Canada. It is part of the Athabasca sub-basin, which is a portion of the Mackenzie Basin that originates at the Columbia Icefield in Jasper National Park, flows in a north-easterly direction, and drains into Peace Athabasca Delta and Lake Athabasca, approximately 1500 km long. The Athabasca River basin is home to mining, forestry, and agricultural activities, significantly the lower reach (LAR). The riverbed in this section is made up of gravel, sand, and cohesive sediment [25] [26]. The geometry of the river is complex, with islands covered by vegetation, alternating sand bars, and a thalweg that is unpredictable. This complex geometry makes the numerical modelling and understanding of the physical behaviour of the river difficult. For instance, between Fort McMurray and Old Fort, the river has been described between a meandering and braided river [27].

The weather condition in Fort McMurray (which is located on the Lower Athabasca River) can be considered a representative of the weather condition in the Lower Athabasca River in winter. The weather is very frigid in winter. Based on the information provided by Climate Atlas of Canada [28] the mean temperature is -7.5°C in November (from 1976 to 2005), and the winter days (colder than -15°C) takes almost 89 days in a year. The annual precipitation is 441 mm, and in November it is 21 mm.

Several major tributaries join the Athabasca River, including the McLeod, Pembina, Lesser Slave, and Clearwater rivers [29]. The Ells, Firebag, MacKay, Muskeg, and Steepbank rivers are other main tributaries that join the LAR. The location and more information about these tributaries in the LAR are provided in Table 1.1.

These features made the Lower Athabasca River a very interesting river for the researchers; hence data for the numerical modelling is easily available. Also, due to the slight chance of having proper images for remote sensing studies in general, by having two high-resolution near-simultaneous images for this area, we chose this river for our research.

Table 1.1 Geographical information of the main tributaries in the LAR (Data collected from WSC).

Tributary (Station)	Location, Cartesian (X,Y)	Label
Ells River near the mouth	(456928.433, 6347420.147)	07DA017
Firebag River near the mouth	(487907.559, 6389883.323)	07DC001
MacKay River near Fort Mackay	(458014.123, 6341016.834)	07DB001
Muskeg River near Fort Mackay	(465543.318, 6338813.211)	07DA008
Steepbank River near Fort McMurray	(475285.455, 6317397.667)	07DA006

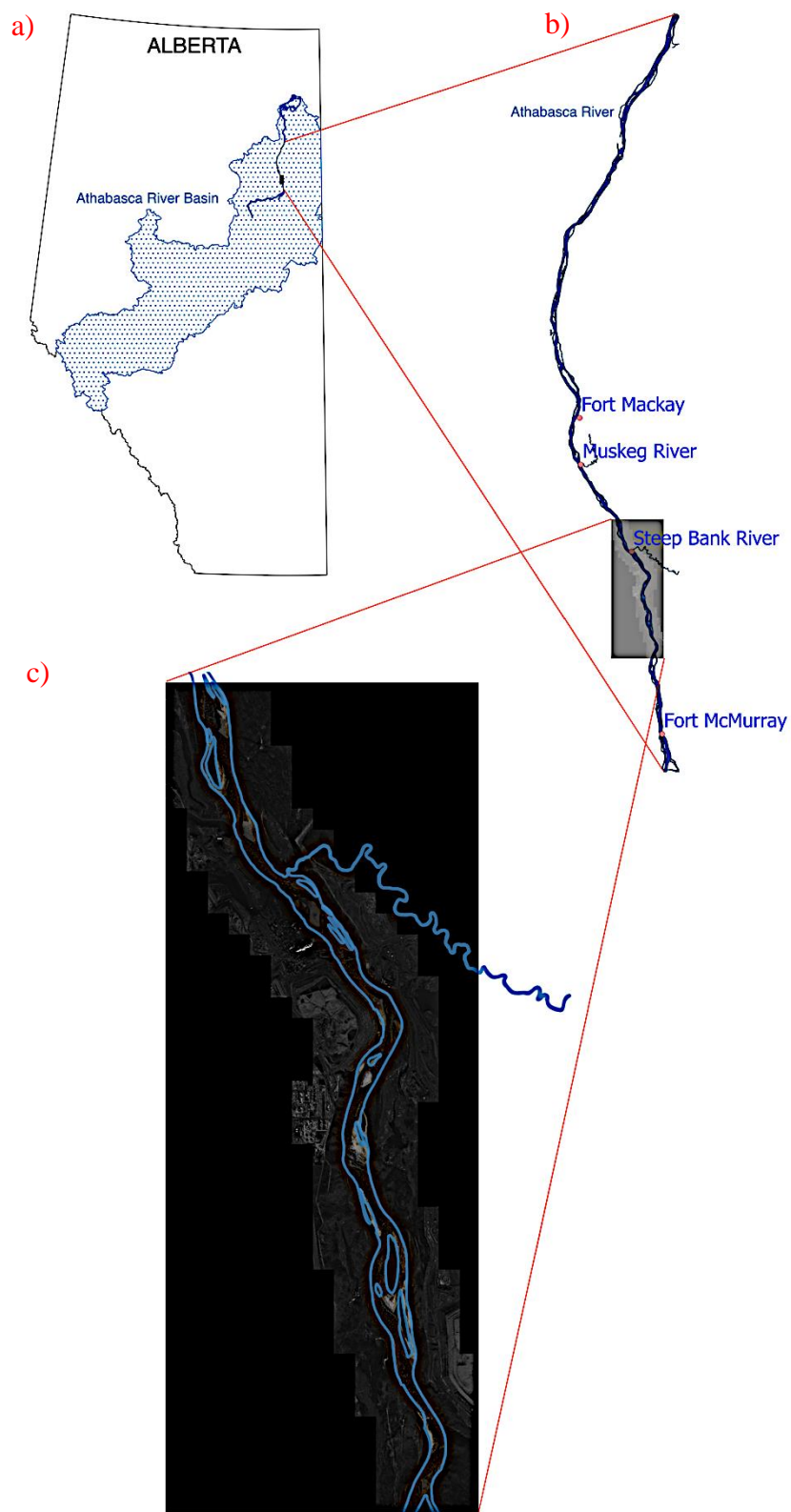


Figure 1.3 a) Athabasca River Basin located in the province of Alberta, Canada [30]. b) The extent of the simulated river. c) The extent of the river with available satellite imagery.

CHAPTER 2 LITERATURE REVIEW

In the study of hydro systems (in our research: the river), field data play an essential role in understanding the underlying processes and mechanisms and in the configuration, calibration, and validation of the numerical and physical models. Field data are typically acquired through field measurements [31] [32], which is time and energy-consuming and often challenging. Even if the measurement is possible, each measuring device is limited to just one cross-section [33]. Unfortunately, it is possible to have sparse and noisy observations [33] in many practical cases. If both spatial and temporal variations of a characteristic (e.g., velocity) are needed, the field measurement will be even more complicated. The situation becomes more problematic in cold regions, where a large percentage of the river surface is covered by ice in the winter [34], making the field measurement impractical. In the following sections, two methods that were used in this study (remote sensing and numerical modelling) will be reviewed.

Due to its special location, complex characteristics, and challenging morphology, the Lower Athabasca River is already an attractive object to study and monitor [35]. In the following sections, the works that have been done in this area are mentioned.

2.1 Motion tracking using image processing

Tracking flow is divided into two methods, intrusive and non-intrusive [33]. Intrusive flow measurement techniques use current-meter or Acoustic Doppler current profilers. The first method provides low spatial and temporal resolutions results, and the Acoustic Doppler Velocimetry (ADV) needs a human presence in the field, which is not always safe [36]. Non-intrusive techniques use indirect measurements by tracking a tracer in water, for instance, the dilution method and the Particle Image Velocimetry (PIV). In these two methods, a chosen tracer is injected into the flow, and the tracer's velocity shows the velocity of the flow.

When a tracer is being used to estimate the flow, the displacement of the tracer is representative of the velocity of the flow. However, the velocity of the tracer is not precisely equal to the velocity of the flow. To track this movement along with the flow, the image processing helps scientists and experts. For instance, the PIV method estimates the displacement of defined flow zones using taken images at two sequential time series. It is mainly used in laboratories and needs laser illumination; instead, the LS-PIV (Large Scale Particle Image Velocimetry), which is an alternative to PIV in

nature, uses natural light, and it can be used in large scales natural hydro systems like rivers and lakes [37] [38] [39]. This technique can also use floating ice as a natural tracer and estimate the flow [40].

The types of images that are used in image processing methods are different. They could be captured by simple cameras installed near the river, captured from higher elevations (aerial photos), or satellite images. In this study, we used satellite images, and more details will be provided in the following sections.

2.2 Remote Sensing

Numerical and physical modelling, and indirect measurement through remote sensing, are the alternatives to the challenging field measurements. The Remote Sensing method has a wide application in different areas, including water-surface dynamic and ice studies. Decades ago, when glacier studies were using satellite images, the flow was detected manually [41]. Later, this process has been changed to automatic process [42] [43], and different image matching methods were tested to evaluate their application [44] [45] [46].

Regarding the water surface studies, since the break-up season is considered the most critical hydrological event of the year, most studies investigated the application of RS in velocity estimation during the break-up season. However, the ice freeze-up period has been used in some studies to evaluate the application of ice debris in the freeze-up season in the remote estimation of the water-surface velocity [47].

Remote sensing uses the imagery data captured by airborne or space-borne satellites to analyze the motion detection on the earth's surface. SAR (Synthetic Aperture Radar), for example, is a system that uses the Doppler effect to track slow-moving objects (ships, ground vehicles, etc.). The SAR systems were utilised to identify or monitor vehicles and traffic continuously day or night in any weather condition [48]. AT-InSAR (along-track SAR interferometry) techniques which were used to track the vehicles, have been used earlier to estimate the ocean currents in 1987 [49]. Also, AT-InSAR has been used in another study to measure the currents of the Dutch Wadden sea [50] and to measure the currents in the Elbe River, Germany [51].

The hydraulic characteristics of a river obtained by the remote sensing methods could be useful to estimate the river discharge. Hydraulic information (e.g., water-surface width, slope, and water-

surface velocity) of the river can be extracted from remote sources. A study has been conducted to estimate the discharge based on the data that all received remotely [52]. In this study, the remotely sensed measurement of width, stage and depth, water-surface slope, and water-surface velocity has been used to evaluate the development of a general method for estimating the river discharge. Then, the obtained methodology from this study has been applied to estimate the discharge of the Missouri River [53]. In this study, each parameter has been obtained from different sources. For instance, the maximum channel width was measured using digital orthophoto quadrangles (DOQs) provided by the National Digital Orthophoto (NDOP). The water-surface velocity was obtained from airborne along-track interferometric (ATI) SAR images (AirSAR) using the Doppler along-track interferometry techniques developed by JPL [54].

Radar Remote Sensing could also be beneficent to observe the ice parcels on the river. The RADARSAT-1 Synthetic Aperture Radar (SAR) satellite images have been examined to see the ability of these images to distinguish the river ice during the winter (2004), and spring break up (2003 and 2004) on different Athabasca River reaches near Fort McMurray [55]. In this study, each pixel of the image was classified as ice jams, intact ice, or open water, and also the thickness of the ice was determined. Recent related studies explored the application of RS in the river/sea ice deformation [56] and the flood vulnerability [57].

Another feature that could be tracked and measured by the remote sensing method is suspended sediment concentration (SSC), which is carried by water and can represent the river flow velocity [58]. The SSC is a function of turbidity and can change the water reflectance, which is detectable in the satellite images [58]. Pavelsky and Smith used SPOT and ASTER images to detect the SSC in the Peace-Athabasca Delta, Canada, for four days in 2006 and 2007, and MODIS satellite images helped track the lake recharge [58].

Furthermore, remote sensing can also detect motion in water systems covered by ice. For instance, sea-ice motions have been tracked using low-resolution satellite sensors in the Arctic [59]. In comparison with sediment, ice debris is more visible and has more contrast with the water surface [60]. For the first time, [15] used the movement of river ice debris as an indicator of the water velocity from stereo images (ASTER, PRISM, and IKONOS) with about one minute of time lag, and they worked on the St. Lawrence River, Quebec, Canada, and the Mackenzie River at the Canadian Arctic on the break-up season. Two years later, this study has been followed with a

specially requested ASTER image for tracking ice debris over a 600 km long reach of the Lena River, Siberia [23] using CIAS software. CIAS is an automated image correlation software based on the Block Matching Algorithm (BMA) [61]. The application of the CIAS is not only in water resources. For instance, it calculated the individual terrain feature displacements using a multi-temporal digital orthophoto [62]. The structure of this software will be discussed in the methodology chapter.

In recent years, “near-simultaneous images” have been used a lot to detect river motions. These images are captured with time separations in the order of minutes. For the first time, the application of these images over a large flow has been exploited systematically by measuring the river flow from ice debris, water velocities from suspended sediments, sea ice and cloud motion tracking, wave motion, vehicles from minute-scale time-lags, and second-scale time-lags [63].

After significant success in using the CIAS [23] to estimate water velocity during the ice break-up and good results of using near-simultaneous images to detect the motion [63], another study has been conducted to calculate discharge during ice break-up along the 40 km long reach of the McKenzie River using the same method to estimate water-surface velocity [64]. They used images taken by PRISM with two different time-lags, and the ice slabs were clearly visible with a noticeable contrast with the water surface. They used CIAS to measure the displacement between two images. Combining the obtained results as a water-surface velocity with measured channel bathymetry in some cross-sections and water surface elevations acquired by installed gauges along the study reach leads to the flow discharge computation.

The application of RS has been evaluated in estimating flow discharge of the Yukon River, Alaska. They used different images captured by different satellites to estimate the river characteristics like slope, water elevation, and water surface width [65]. The most recent study on this topic has been done on the river ice freeze-up period [47] on the Yukon River, Alaska, considering the fact that the ice freeze-up period (Nov 2018) takes longer time than the break-up (May 2017), and the ice is more constant and resistant to breaking and deformation. The potential of using the PlanetScope CubeSat constellation images (with 3.7m spatial resolution) has been evaluated in this study.

2.3 Hydraulic Model

To simulate the behaviour of a hydro system (in our study: the river) with specific conditions, the governing equations, including mass conservation and momentum conservation (i.e. Navier-Stokes equations, which are PDE), must be solved. Since there is no analytical solution for these mathematical equations, numerical models and computers help scientists and engineers. Different discretization methods are available to transfer a continuous equation into discrete counterparts. Some numerical discretization schemes are FDM, FVM, FEM, and the mesh-free method. Different software does the discretization to simulate the behaviour of water. As some examples, the following software is mostly used in the modelling of shallow water (e.g., rivers) in 1D or 2D:

HEC-RAS, which was developed by the US Army Corps of Engineers' Hydrological Engineering Center, allows the user to simulate 1D steady flow, 1D and 2D unsteady flow calculations, sediment transport/mobile bed computation, and water temperature/ water quality modelling [66]. MIKE 11 is a 1D model provided by the Danish Hydraulic Institute (DHI) with applications in flood analysis, dam break analysis, sediment transport model, etc. [67]. MIKE 11 has been used to investigate the implications of anticipated climate change on the Lower Athabasca River's hydrodynamic and sediment transport regime [68]. MIKE-12 Flow Model is the leading software package for 2D modelling hydrodynamics, waves, sediment dynamics, water quality, and ecology [69]. In summary, the followings are some of the most extensively used 1D modelling programs: HEC-RAS, DWOPER, FLD-WAV, MIKE 11, River1D, and SOBEK-1D, and the following are some of the most extensively used 2D modelling programs: FLO 2D, RMA2, MIKE 21, DELFT-FLS, TELEMAC-2D, River2D and DELFT3D [70]. These 1D and 2D numerical models can also be commonly employed to simulate flow depth and depth-averaged velocity in rivers with different applications [19] [71] [72].

In this study, DELFT3D software has been used to simulate the LAR and develop a model to estimate the depth-averaged velocity. The DELFT3D is open-source software that allows the user to simulate hydrodynamics (DELFT3D-FLOW), morpho dynamics (DELFT3D-MOR), waves (DELFT3D-WAVE), water quality (DELFT3D-WAQ), and particles (DELFT3D-PART module) [73]. DELFT3D is currently extensively utilized and has shown to be helpful in solving challenging hydrodynamics issues [74]. DELFT3D-FLOW is a module of DELFT3D which has been used in different hydrodynamic modelling. For instance, in river modelling [75] [76] [77], sand and

sediment transport modelling [78] [79], tidal turbines simulation [80], salt-wedge estuary [81] etc. Williams et al. validated a 2D simulation of braided river flow (they simulated the river flow using field measurement and aerial photography) [82].

More related studies have been done to simulate the flow in the LAR in recent years. Andrishak et al. (2008) did an early study to simulate flow in the LAR using a 1D model [83]. Also, based on the high demand for understanding the transport of sediment and chemical constituents, a 1D model has been developed to investigate the sediment regime for open water (using MIKE 11) and ice-covered conditions (using CRISSP 1D) in LAR [35]. Later, Kashyap et al. built a 2D model using EFDC to simulate the movement of the sediment and chemical constituent in the LAR [84]. Recently, some efforts have been undertaken to investigate the LAR using 2D numerical models to simulate the flow and understand the ice processes. For instance, Dibike et al. simulated the flow using EFDC to follow the fate of Oil Sands tailings release into the LAR [85].

2.4 Problems and Research objectives

Considering the reviewed literature and identified problems and knowledge gaps, this research aims to estimate the river ice motion and water velocity field in the cold-region rivers from the satellite imagery data and investigate the reliability and limitation of such velocity estimation compared with numerical modelling. Furthermore, for the river of case study, this research is expected to provide valuable velocity data that can be used to study the mechanisms and processes in the river or validation and evaluation of numerical models. The particular case study of this research is the Lower Athabasca River (LAR).

The specific objectives of this research are defined as:

- 1) Acquiring and processing the satellite imagery data for quantifying ice motions and flow velocity of satellite images.
- 2) Setting up and validating a two-dimensional (depth-averaged) numerical model for the case study of this research.
- 3) Investigating the reliability and limitations of the technique and data achieved from objective 1 compared to the numerical results of objective 2.

2.5 Structure of the thesis

Chapter 3 of this study will discuss the methodology, including two parts. The first part is about remote sensing and the second part is about the hydraulic model. In the remote sensing part, the following subjects will be discussed:

- Acquisition of the imagery data
- Motion detection algorithm (Block Matching Algorithm)
- Image pre-processing
- Implementation of the remote sensing method on the obtained images using CIAS

In the second part (hydraulic model), the following subjects will be covered:

- Governing Equations in hydraulic models
- The combination of bathymetry data obtained from different sources
- The setting of the model in DELFT3D

Chapter 4 of this study will include the post-processing applied to the results of the numerical model and remote sensing with the following subjects:

- Calibration and validation of the hydraulic model
- Obtaining the type of flow in the LAR
- Conversion of depth-averaged velocity to surface velocity
- Error elimination
- Smoothing

This chapter also includes:

- Comparison of the obtained velocities in different cross-sections
- Conclusion

Chapter 5 of this study will consist of the conclusion, discussion and possible future work.

CHAPTER 3 METHODOLOGY

This chapter will explain the methodology of the remote sensing technique and hydraulic simulation.

3.1 Remote Sensing

The acquisition of the data, the Block Matching Algorithm, and the preprocessing of the images will be explained in the following sections.

3.1.1 Acquisition of the imagery data

Different types of images (e.g., airborne images, space-borne images with minute-scale time lag, or second-scale time lag) are captured by number of acquisition constellations each day. They can provide proper or sometimes improper images. The improper images are mostly with noise or in cold regions, the surface is covered by clouds, and no information could be obtained from these images. The high-quality images can be helpful in different studies to get various parameters. To measure the changes in a location of an object on the river surface remotely, the best images that can be used are near-simultaneous images. These images are obtained from individual stereo sensors. The images must satisfy some conditions to be useful. They must be high-resolution, have low cloud coverage, and have apparent moving ice floes. Obtaining images with the mentioned conditions is challenging. In this study, we decided to use images from DigitalGlobe company, which merged with MDA Holdings on 5th October 2017 and is now called Maxar¹.

This company has four on-orbit satellites (WORLDVIEW-1, WORLDVIEW-2, WORLDVIEW-3, and GEOEYE-1) and three decommissioned (QUICKBIRD, IKONOS, and WORLDVIEW-4). Two near-simultaneous images captured by GEOEYE-1 on 11 November 2009 at 18:39 are used

¹ <https://www.geospatialworld.net/news/mda-dg-combined-entity-to-be-rebranded-as-maxar-technologies/>

with the characteristics provided in Table 3.1. The time lag between two acquired images is equal to 56 s. Also, the extent of the captured images is shown in

Table 3.2, and the location of the captured image is shown in Figure 1.3. More information regarding the reason for this choice will be provided in the following paragraphs.

Table 3.1 Characteristics of the obtained images from Maxar company on 11 November 2009.

Sensor Type	Satellite
Sensor name	GeoEye-1
Processing level	Standard Geometrically Corrected
Image Type	PAN
Interpolation method	Cubic Convolution
Pixel size	0.5 m
Map Projection	Universal Transverse Mercator (UTM), 12N
Datum	WGS84
File Format	GeoTIFF
Cloud Coverage	0%

Table 3.2 Product MBR (Minimum Bounding Rectangle) Geographical Coordinates (the maximum extents of the image).

Coordinate number	Latitude	Longitude	UTM Easting	UTM Northing
1	57.0616281592	-111.5302481916	467842.01 (min x)	6324370.98 (max y)
2	57.0620968148	-111.4046155710	475461.53 (max x)	6324370.91 (max y)
3	56.8798659319	-111.4026448594	475461.49 (max x)	6304085.51 (min y)
4	56.8794005085	-111.5276656376	467841.98 (min x)	6304085.56 (min y)

The reason for choosing the Maxar company's images taken from GeoEye-1 as the source for this study is the existing restrictions. There are many satellites and sensors that visit the Earth's surface each day. For instance, MODIS, SPOT, ASTER, PRISM and Planet constellation are some satellites which take images from Earth daily. The highest spatial resolution of MODIS is 250 m, and ASTER takes images with 15 m resolution in visible and near-infrared bands. The images obtained from these satellites do not have a satisfying spatial resolution for this study. Other

satellites can provide higher-resolution images. For instance, the highest resolution that SPOT can capture is 2.5 m in the panchromatic band. Planet constellation and PRISM satellite can also take high-resolution images (2.5 m and 2 m). Also, IKONOS, WORLDVIEW or QUICKBIRD can provide images with 0.5 m to 1 m resolution. However, the spatial resolution of these images can be satisfying, the temporal resolution is not useful in our study. It takes days or weeks to capture the same scene by these single sensor satellites [23].

An alternative to solve the temporal resolution problem is using the stereo satellites (like GeoEye-1) which capture the same scene with a small time lag. However, the remaining challenge in obtaining the proper images is the fact that in cold seasons (between ice freeze-up and break-up) the rivers are not the main target of the satellites [23], probably due to the high percentage of cloud coverage on that time.

By considering all the above limitations, the mentioned near-simultaneous images with 0.5 m spatial resolution and 56-second time lag (captured on 11 November 2009) have been obtained from the sensor (GeoEye-1) from the Maxar company's archive. Figure 3.1 demonstrates the basic characteristics of the GeoEye-1 sensor.

Therefore, the cause for choosing 11 November 2009 as our study day is that based on the limitations this day is the only day that we can see ice floes from space with high-quality images in the freeze-up period.

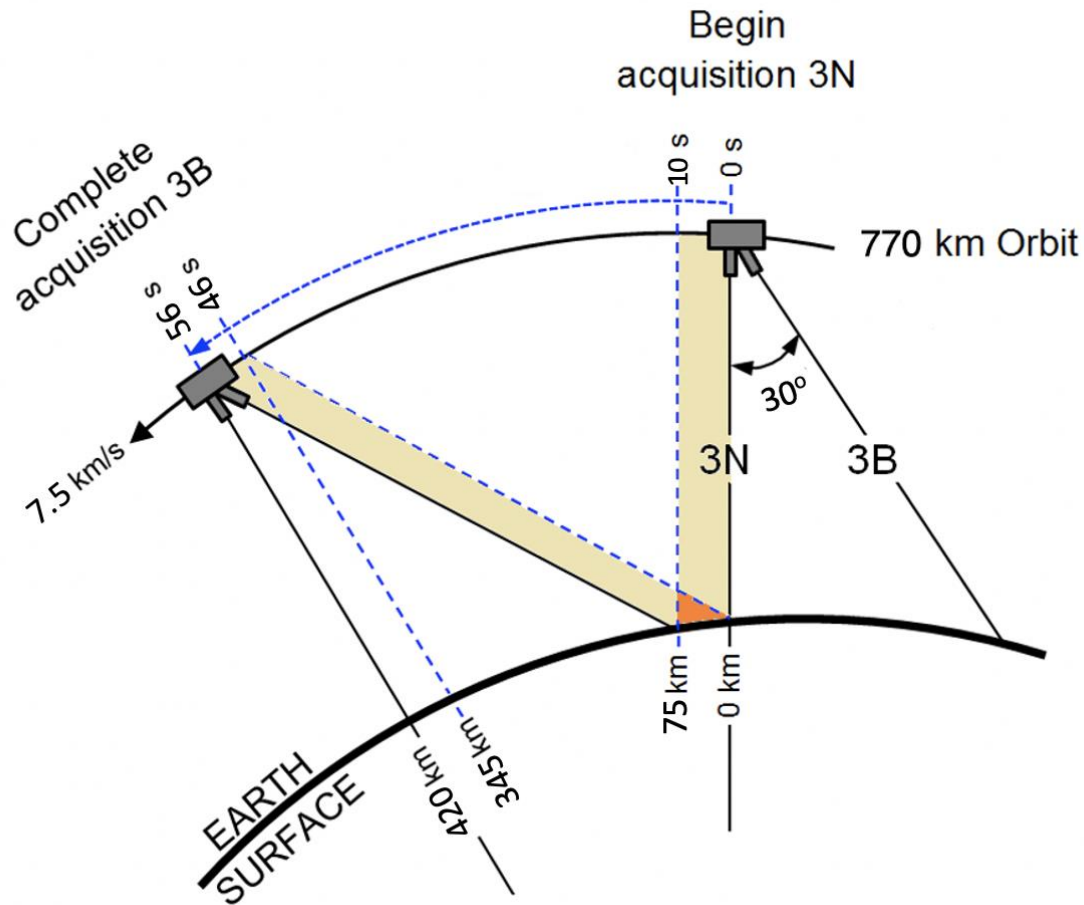


Figure 3.1 GeoEye-1 collection modes. The sensor takes simultaneous panchromatic (0.5 m resolution) and multispectral (1.84 m resolution) images in 15.2 km swaths.

The GeoEye-1 satellite has been launched in September 2008. The orbit of the satellite is sun-synchronous and it moves with a velocity of 7.5 km/h. It has two camera modes capable of taking panchromatic and multispectral images with 0.5 m and 1.84 m resolution. Since the panchromatic mode has a higher resolution, we used this band in our study. Two images can be taken with the time difference in the order of a minute from the same scene by two sensors (nadir-band 3N and the back-looking sensor 3B) with a 30-degree inclination. These images are considered near-simultaneous images and they show the same surface at two different times. More information regarding the GeoEye-1 sensor is provided in Figure 3.1.

3.1.2 Motion detection algorithm in images

There are different methods to measure the movement of an object in two or more sequential images, and in this study, we use the Block Matching Algorithm (BMA). The Block Matching Algorithm divides an image into small windows. It compares each window in the reference image to the corresponding window and possible adjacent neighbours in the second image to find the best matching block. The size of the window is defined by “Reference block size” in pixels, and the adjacent neighbours are defined by “Search area size” in pixels. Figure 3.2 shows a simple schematic of the Block Matching Algorithm. The block with the highest correspondence value is the matching block in the search window. The cross-correlation method is used [85] to measure the correspondence value between two blocks. One software that uses this method to calculate the motion between two images is the CIAS.

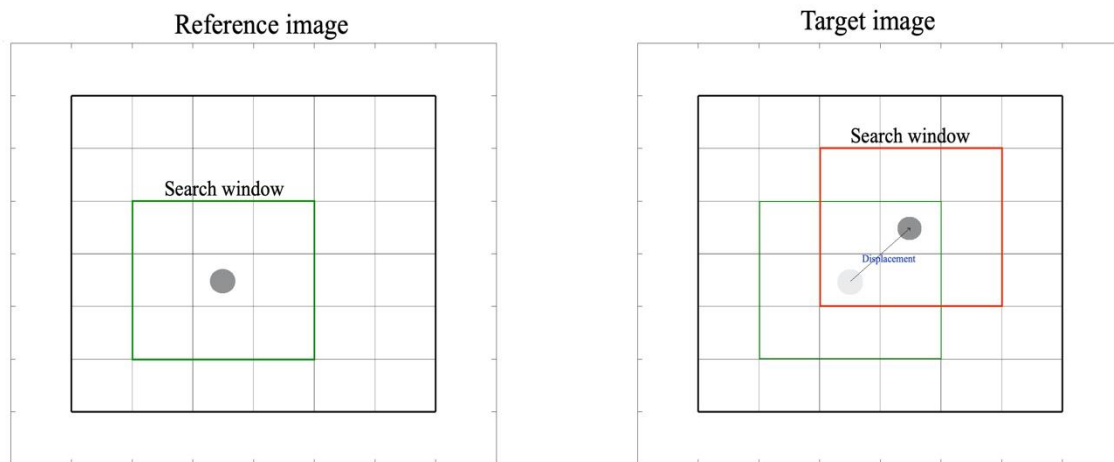


Figure 3.2 Motion estimation using block matching algorithm.

To prepare the taken images for the CIAS, we must make sure that they have the following characteristics:

1. The images must be captured from the same position or precisely co-registered.
2. The images must be in GeoTiff or Tiff World format (containing geographical information).
3. The images must have the same resolution.
4. Pixels in an image must be square (same resolution in X and Y direction).

The satellite images that we used have five bands. Panchromatic, Blue, Red, Green, and Near Infra-Red (NIR). We used the Panchromatic band for this study because of its higher resolution; hence,

each pixel has just one assigned value (called gray-scale). This pixel value could be detected in the second image to measure the displacement.

Captured images are already qualified for all prerequisites except the first one. The format is GeoTiff, and both images have 0.5m resolution in both X and Y directions. However, due to the satellite's movement and different acquisition angles in the two images, they do not match perfectly. Consequently, a co-registration method must be implemented to avoid further errors and inaccuracies and ensure that the images are spatially aligned.

3.1.3 Image pre-processing

Before starting the process of ice motion detection preprocessing is required. The first step is to ensure that the images are spatially aligned so that fixed terrain features in one image overlap the other image in the series [86]. To do so, one should do the co-registration of images. One image is selected as the reference in co-registration, and the other images will be aligned with the reference. Here, we chose the first image as a reference image, and the second image will be aligned with the first one. The co-registration algorithm could be either intensity-based or feature-based. Intensity-based methods use correlation measurements to compare image intensity patterns, whereas feature-based methods look for correspondence between images components like points, lines, and contours [87].

Here, we used the feature-based method. Common features (the ones that are detectable in both images) are manually identified as tie points (also called GCP: Ground Control Points). The first point is specified in the unregistered image, and then the x-y coordinate of this point will be identified in the reference image. As a result of a manual definition of tie points, an exact match of images is rarely achievable [86], and errors could not be eliminated. The number of points and their quality and geographical distribution are all elements that contribute to a successful translation [88]. These tie points are used by co-registration applications to match the remaining pixels and align the images completely. Here, we used QGIS software to do most of the required image processing to prepare two images for the next steps.

Co-registration in QGIS is performed by “Georeferencer Plugin”. By producing a new GeoTiff or adding a world file to an existing image, “raster” files can be referenced to geographic or projected coordinate systems. This plugin uses tie points to understand the relation between relevant points

in two images. Here we finally specified 672 points as tie points. For instance, Figure 3.3 shows a structure, near the Athabasca River, in the reference image, and its corner could be defined as tie points, and Figure 3.4 shows the same structure in the unregistered image. In the reference image, two specific points on the roof are marked red. The same points are marked in yellow in the second image. This part of the image could be almost co-registered by transferring yellow points to red ones.

More points like these points must be used to co-register the entire image. In defining the tie points, adding points close to the river's boundary is essential to get the best possible georeferenced image. With the tie points far from the river and its physical characteristics like boundaries or islands, the georeferencing algorithm cannot georeference the river properly.

After defining the tie points manually, the transformation method must be selected. QGIS has different algorithms to do the transformation. The explanation of each transformation algorithm and its functionality is here:

- 1) **Linear**: this algorithm creates a world file to add to an image. The Linear algorithm needs at least two GCPs to do the scaling and transformation, and it does not do the transformation locally. This method does not actually transfer the data; hence it differs from the others. If the unregistered image is already of acceptable quality and only needs to be georeferenced, this technique is a reasonable option. Otherwise, this algorithm will most likely be insufficient if the materials are scanned.
- 2) **Helmert**: this algorithm is more capable than the Linear algorithm. It transforms the images by scaling and rotating them, yet it is insufficient for complex cases. It also needs at least two GCPs to do the registration.
- 3) **Polynomial**: this algorithm contains three transformation methods (first-order, second-order, and third-order polynomial transformation). The first-order polynomial transformation needs three GCPs. However, the second-order and third-order need six GCPs, and they consider the earth's curvature. The first-order polynomial transformation transforms the images by scaling, translation, and rotation, maintaining collinearity. The second-order polynomial transformation allows some curvature; hence it is the most commonly used polynomial algorithm.

- 4) **Thin Plate Spline**: the TPS transformation needs ten GCPs, and it can transform the data locally. This method is the most recent algorithm which can georeference very low-quality or damaged maps. This algorithm is included in the elastic or nonrigid transformation method, which allows the images to be aligned locally; hence, it takes more time to apply it on the map.
- 5) **Projective**: the Projective transformation needs four GCPs and transfers the coordinates by linear rotation and transition.

These definitions give a good view of which algorithm to be chosen. However, we applied all the five algorithms with #156 GCPs to evaluate their functionality. Each transition gives a Mean Residual Total (in pixels) available in the generated report file. The values of the MRT for all transformation is available in Table 3.3.

Table 3.3 The values of MRT by using different co-registration algorithms.

Algorithm	Minimum required points (GCP)	Mean Residual Total (pixels)
Linear	2	50.1983
Helmert	2	50.2067
Polynomial	First-order: 3	30.01917
	Second-order and Third-order: 6	
Thin Plate Spline	10	8.83898E-05
Projective	4	43.1938

The Mean Residual Total is calculated with the following formula:

$$Error = \sqrt{\frac{\sum_{i=1}^n R_i^2}{n - o}} \quad \text{Equation 3.1}$$

where:

n is the total number of GCPs,

o is the number of Minimum required GCPs,

R_i is the distance between the transformed point and the expected transformed point.

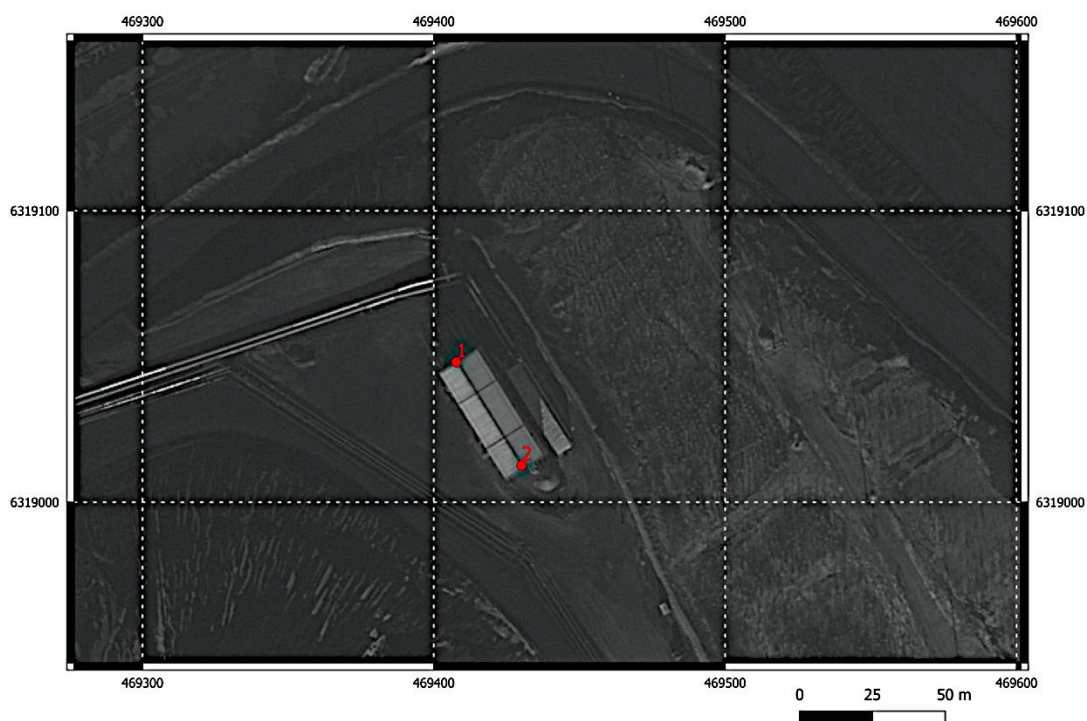


Figure 3.3 The location of two tie points in the reference image (GCP #1 and #2).

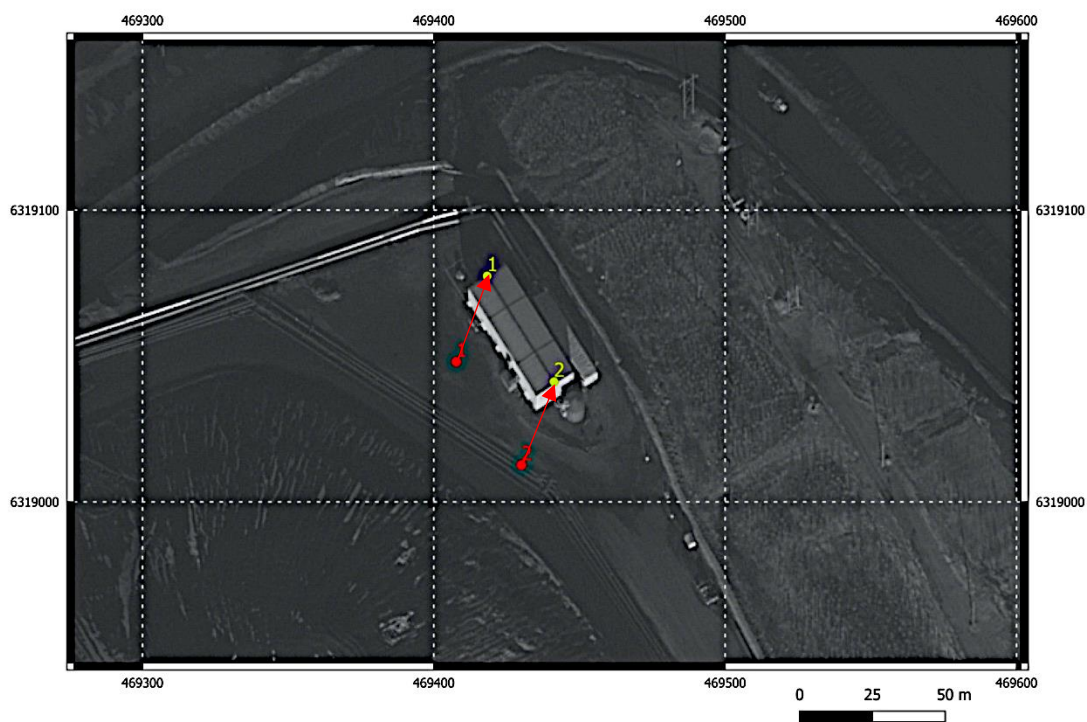


Figure 3.4 The location of the tie points in the unregistered image (GCP #1 and #2).

As was expected, the smallest MRT belongs to the TPS algorithm due to its local alignment, and the Linear transformation is the least accurate algorithm. Therefore, an image that has been co-registered using the TPS algorithm is used for the next steps. However, after a visual assessment of the river, we concluded that the georeferencing needs to be more accurate for a better match. Therefore, #516 points have been added as a GCP to the areas that required more alignment, and the georeferencing was applied to the image with #672 points in total.

In the provided figures in APPENDIX A, one cross-section of the river is co-registered with all five methods, and also the reference image is shown. A small subject has been specified as a checkpoint (CHP) to realize the differences between algorithms. As is visible in the figures, the TPS algorithm aligns the unregistered image with the reference image more precisely than the other algorithms. Though just a small reach of the river is shown in this figure, the effect of the algorithms is mostly the same all over the image. Both images are ready for comparison; however, they do not match 100 percent.

3.1.4 Implementation

After preparing the images and importing them into the CIAS, the co-registration method must be chosen. The software provides just one method for co-registration (Helmert). Since it is already done even more accurately, we decided “Measure WITHOUT co-registration” option. In the next step, the Correlation Algorithm must be chosen. Between the two available options (Normalized Cross-Correlation (NCC) and Orientation Correlation (NCC-O)), we chose and applied the NCC method. The measure of Normalized Cross-Correlation (NCC) has long been used to determine the degree of similarity (or dissimilarity) between two images which has the benefit of being less sensitive to linear changes in the amplitude of brightness and contrast in the two compared images than the cross-correlation algorithm [89]. The NCC and the following formula show the Cross-Correlation measurement between two images. The cross-correlation peak demonstrates the displacement of the target between the images.

$$CC(i, j) = \frac{\sum_{k,l} (s(i+k, j+l) - \mu_s)(r(k, l) - \mu_r)}{\sqrt{\sum_{k,l} (s(i+k, j+l) - \mu_s)^2 \sum_{k,l} (r(k, l) - \mu_r)^2}} \quad \text{Equation 3.2}$$

where

(i, j) is the position in the search image.

(k, l) the position in the reference image.

r is the pixel value of the target in the reference image.

s is the pixel value of the target in the search image.

μ_r is the average pixel value of the search area in the reference image, and

μ_s is the average pixel value of the search area in the search image.

The object in the reference image found in the target image must be defined as a point with X and Y coordinates in the CIAS. These points can be defined as “SINGLE points”, “POLYGON,” or “XY file”. The two first must be defined and drawn visually inside the CIAS. The “XY file” allows the user to import the points easily. We have decided to select two series of points. The first series has been chosen manually in the QGIS to represent some obvious ice floes, and the second series is the center of the staggered grids used in the numerical model. The latter will be explained in more detail in 4.2.2.

For the first series, in the first step, 1217 points have been chosen to be used as an input in the CIAS. The points are selected based on their visibility. They are visible ice floes that seem easy to be detected visually. The location of each point is almost the center of the ice, and it is going to be the center of the search window and has been extracted from the QGIS.

As mentioned earlier (3.1.2), two different block sizes must be defined: “Reference block size” and “Search area size”. Therefore, various combinations of these two factors are possible and lead to

different results. The best combination to optimize the matching result could be distinguished by doing a Sensitivity Analysis and comparing the results.

3.1.4.1 Sensitivity Analysis

To do the Sensitivity Analysis, different “Reference block size” and “Search area size” were coupled together, and the algorithm was applied to the images to compare the results. Measuring the possible errors for each series of measurements needs an exact source. Since this type of source data is not available, we created a source of “Real Movement Values”. Measuring these values has been done manually by finding the approximate correlated location of each defined point in the target image in QGIS by the operator. After finding these locations, each point’s approximate Real Movement Value could be easily measured. However, these values are not accurate, and they are just an approximation and need correction. Figure 3.5 shows how the movement values are defined by measuring the distance between the same points in two images.

Figure 3.5 a) demonstrates the initial position of the ice floe by yellow points in the reference image. Figure 3.5 b) shows the same points in the target image by red points and their earlier location after a while. After extracting the location of ice floes from the first and second images, an approximate movement for each was estimated by calculating the distance. However, this calculation is not accurate; it could be used as a source to compare the result of the CIAS and do the Sensitivity Analysis.

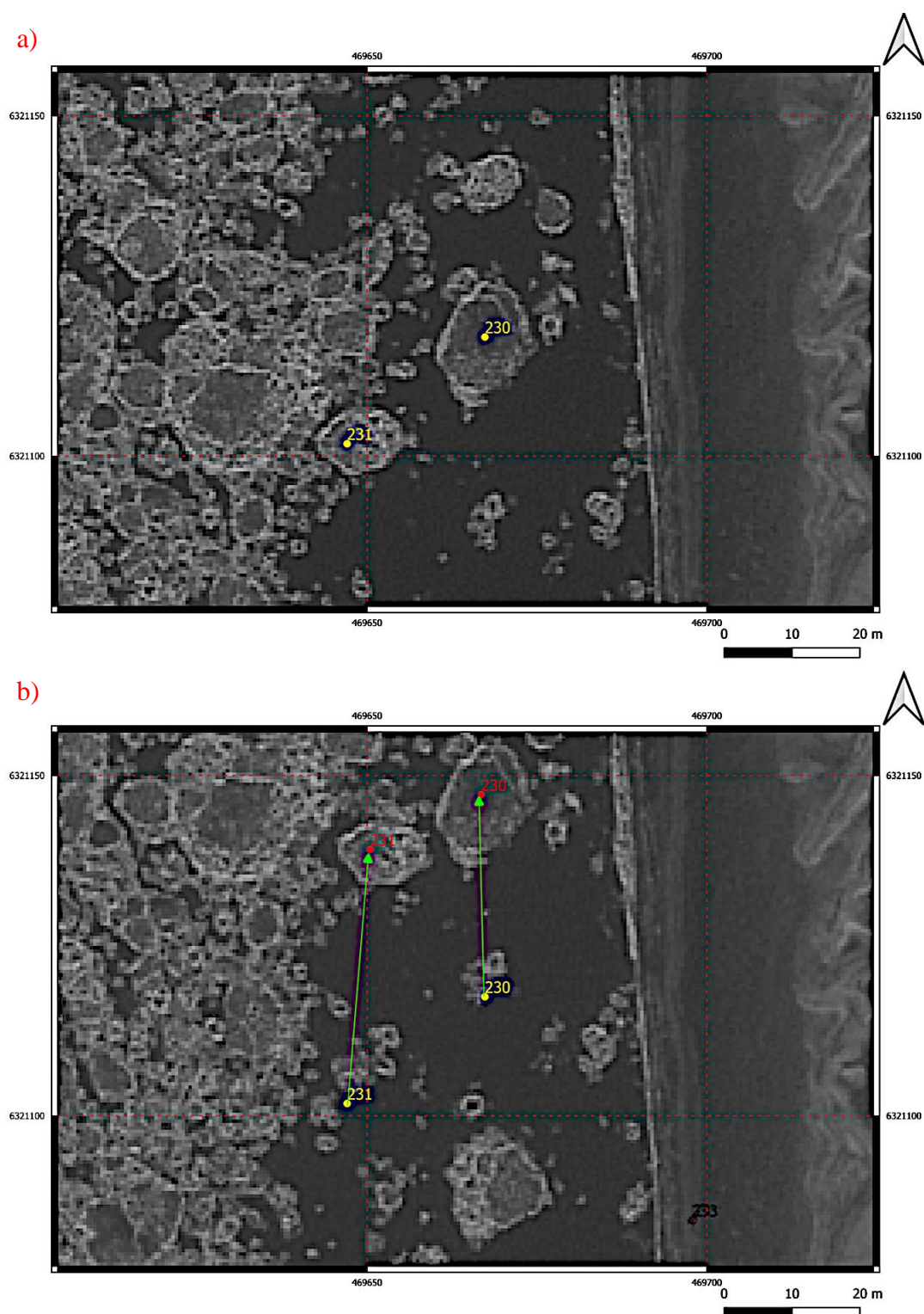


Figure 3.5 The location of two ice floes #230 and #231 a) in the reference image and b) in the target image. The distance between the location of points in the first and second image shows ice floes' movements.

The result of the analysis is provided in Table 3.4. At first, “Reference block size” is considered constant and equal to 15 pixels, and different “Search area sizes” from 120 to 280 have been tried. By increasing the “Reference block size,” the difference between the result of BMA and the approximate Real Movement Value decreased firstly, but after 240 pixels, it increased. Then, the “Reference block size” was changed to 20 pixels. Again, the same trend happened: diminution at first and then raise after increasing the “Search area size”.

In comparison between “Reference block sizes” (15 pixels and 20 pixels), when the “Search area size” is constant (240 pixels), “Reference block size” equal to 20 pixels shows the best performance. In conclusion, Table 3.4 shows the Root Mean Square Error for all the analyses, and it seems that “Search area size” = 240 pixels and “Reference block size” = 20 are the most suitable sizes in our study.

Table 3.4 The RMSE values measured by comparing the results of CIAS with the operator-measured movements for different search area sizes and reference block sizes (Sensitivity Analysis)

Search area size (pixels)	RMSE	
	Reference block size (pixels)=15	Reference block size (pixels)=20
120	20.87	21.65
150	16.67	-
180	-	13.65
240	11.23	10.52
280	12.78	12.40

Sensitivity Analysis results show that the window size of (20, 240) has the minimum RMSE. Since the source values are not precisely correct, and some huge errors make the RMSE very big in the results, we have decided to choose the best window size based on the distribution of the C_{\max} value. This value shows the correlation between two windows in reference and target images. Hence, the greater the mean and the smaller the standard deviation indicates a better match. The mean and standard deviation values for each window size are provided in Table 3.5. As a result, the final decision is to choose a “Search area size” = 280 pixels and “Reference block size” = 15.

Table 3.5 The mean value and standard deviation of the C_{\max} for different reference block sizes and search area sizes.

Search area size (pixels)	Reference block size (pixels)=15		Reference block size (pixels)=20	
	Mean of C_{\max}	Standard deviation of C_{\max}	Mean of C_{\max}	Standard deviation of C_{\max}
120	0.569	0.157	0.523	0.161
150	0.640	0.170	-	-
180	-	-	0.653	0.181
240	0.725	0.145	0.709	0.159
280	0.728	0.142	0.713	0.156

To ensure choosing the best pixel sizes, we also calculated the same means and standard deviation for the C_{\max} when the reference block size is equal to 30 pixels and the search area size is 280 pixels. We get 0.66 as the mean value and 0.187 as the standard deviation. Hence, it seems that the algorithm has a better performance with a smaller reference block size, and increasing this value just creates more confusion. Probably, the size of the ice floes plays an important role, and big window sizes cannot detect ice floes properly.

Another way to ensure that the algorithm will work properly is to choose a “search area size” based on the maximum capturable movement. The maximum ice floe movement in our images is smaller than 60 m (obtained by the operator). This value must be smaller than half of the “search area size”. By choosing “search area size” equal to 280 pixels, l (length of the searching window) will be equal to:

$$l = 280 (\text{pixel}) \times 0.5 \left(\frac{m}{\text{pixel}} \right) = 140 \text{ m}$$

Therefore, the software can detect objects at a distance of less than 70 m.

$$\frac{l}{2} = 70 \text{ m}$$

As long as the maximum ice floe movement (in our images: 60 m) is smaller than $\frac{l}{2}$ (70 m), the considered value for l is acceptable.

These selected values for the reference block size and the search area size will be used later when the first series of data is used for the main measurements.

3.1.4.2 Error elimination

These points and the Real Movement Values assigned to them can also be used to select the best error elimination method, which will be explained in detail later in 4.2.2.

3.2 Hydraulic Model

Simulating the Athabasca River using numerical modelling is the second part of this study. We do the simulation to have a continuous source of river behaviour (e.g., depth-averaged velocity and water level). So many simulation software does exist for simulating the water flows by solving the problem based on different numerical discretization schemes. The DELFT3D is an open-source, free program, fully integrated software capable of disciplinary analysis and 3D computations in coastal, river, and estuarine environments, developed by Deltares. The calculations that DELFT3D does to simulate the river and the model's structure will be presented here.

3.2.1 Governing equations

As mentioned earlier, the Navier- Stokes equations are discretized in the majority of hydrodynamic models to simulate the river flow. There are two equations: the continuity equation and the momentum equation for an incompressible fluid ($\frac{D\rho}{Dt} = 0$). DELFT3D-FLOW solves the 2D (depth-averaged) shallow water equation from the Navier-Stokes equations for incompressible free-surface flow.

Continuity equation:

$$\frac{\partial \zeta}{\partial t} + \frac{\partial [h\bar{U}]}{\partial x} + \frac{\partial [h\bar{V}]}{\partial y} = 0 \quad \text{Equation 3.3}$$

Horizontal momentum equation:

$$\frac{\partial U}{\partial t} + U \frac{\partial U}{\partial x} + V \frac{\partial U}{\partial y} = -g \frac{\partial \zeta}{\partial x} + fV + \nu_H \left[\frac{\partial^2 U}{\partial x^2} + \frac{\partial^2 U}{\partial y^2} \right] + \frac{gU\sqrt{U^2+V^2}}{HC^2} + \frac{\rho_{air} C_d W_x \sqrt{W_x^2 + W_y^2}}{\rho_0 H} \quad \text{Equation 3.4}$$

$$\frac{\partial V}{\partial t} + U \frac{\partial V}{\partial x} + V \frac{\partial V}{\partial y} = -g \frac{\partial \zeta}{\partial y} + fU + \nu_H \left[\frac{\partial^2 V}{\partial x^2} + \frac{\partial^2 V}{\partial y^2} \right] + \frac{gV\sqrt{U^2+V^2}}{HC^2} + \frac{\rho_{air} C_d W_y \sqrt{W_x^2 + W_y^2}}{\rho_0 H} \quad \text{Equation 3.5}$$

where

ζ is the Water Level according to the reference level (m).

h is the water depth (m).

U, V is the depth-averaged velocity in respectively X and Y-direction (m/s).

f is the Coriolis parameter (s^{-1}).

ν_H is the horizontal eddy viscosity (m^2/s).

g is the acceleration of gravity (m/s^2).

H is the total water depth (m).

C is the Chezy-coefficient.

ρ_{air} is the density of air (kg/m^3).

C_d is the wind shear stress coefficient.

d is the depth towards the reference level (downwards is positive) (m).

W_x and W_y are wind speeds in respectively X and Y-direction (m/s).

ρ_0 is the density of water (kg/m^3).

3.2.2 Bathymetry and topography data

For the LAR (from Fort McMurray to Old Fort), We used the processed bathymetry data created earlier by Shakibaeinia et al. [90]. The bathymetry data were obtained from the combination of a variety of sources with different resolutions and different coverages due to complex bathymetry and floodplain topography. Considering flood plains are necessary because the risk of flood is high in this river. The sources that have been compiled are:

- (a) Collected high-resolution (5m) bathymetry data for approximately 40 km (from Fort McMurray to Old Fort) by Environment Canada using a GeoSwath sonar sensor (2012-2014).
- (b) Surveyed fifty-four cross-sections of bathymetry data (from Crooked Rapid to Steepbank) by Faye Hicks [91].
- (c) Investigated six high-resolution reaches by CEMA [92] .
- (d) Acquired one hundred twenty-seven DEM synthetic rectangular sections with 1 km intervals from the Mackenzie River Basin Hydraulic Model (from Steepbank River and Embarrass Airport) [93].
- (e) Provided high-resolution (5 m) LiDAR data by Alberta Environment and Sustainable Resources Development (AESRD). They have been used to reproduce the topography

of floodplains and islands processed into DEM by Environment and Climate Change Canada (2014).

- (f) Acquired DEM data of the region (Geobase 2012).
- (g) The LIDAR and DEM data were used primarily to reproduce the topography of the floodplain and islands [35].

The combination of all these bathymetry data sources generated continuous bathymetry for the LAR main channel and the flood plains. Some data adjustments have been made to make the transition between different data sources smoother. The final resolution ranges from 10 to 25 m. These bathymetry data will be used in the numerical reproduction of the river.

Other data, such as initial and final water level, discharge of open boundaries, and other tributaries, are obtained from the Water Survey of Canada (WSC), measured by hydrometric gauges.

3.2.3 Model settings

DELFT3D consists of multiple modules applicable to a particular problem, and DELFT3D-FLOW is one of these modules. DELFT3D-FLOW is a 2D/3D hydrodynamic simulation module that could simulate a river flow [94]. We simulated the river twice:

- for the first time, the extended version of the river has been simulated using coarse grids and available hydrometric data from September 2004 for calibration and validation.
- then we used finer grids for a shorter reach of the river and the hydrometric data of November 2009 to compare the results with velocities obtained by the CIAS.

The following tools have been used to set up the model for both simulations.

3.2.3.1 Pre-processing

Mesh generation

DELFT3D needs the grids/meshes to be defined. Grids are small geometrical shapes covering the physical domain, and each governing equation will be applied to these grids. To create, manipulate and visualize the curvilinear grids, the RGFRID tool could be used. In this study, an already constructed mesh has been used. This mesh was generated using a shapefile covering the Lower Athabasca River's main channel and flood plain. A plain represents the high flow water surface

plus 1 m of freeboard used to cut the bathymetric and topography data into the shapefile; in this way, it can tolerate flood events.

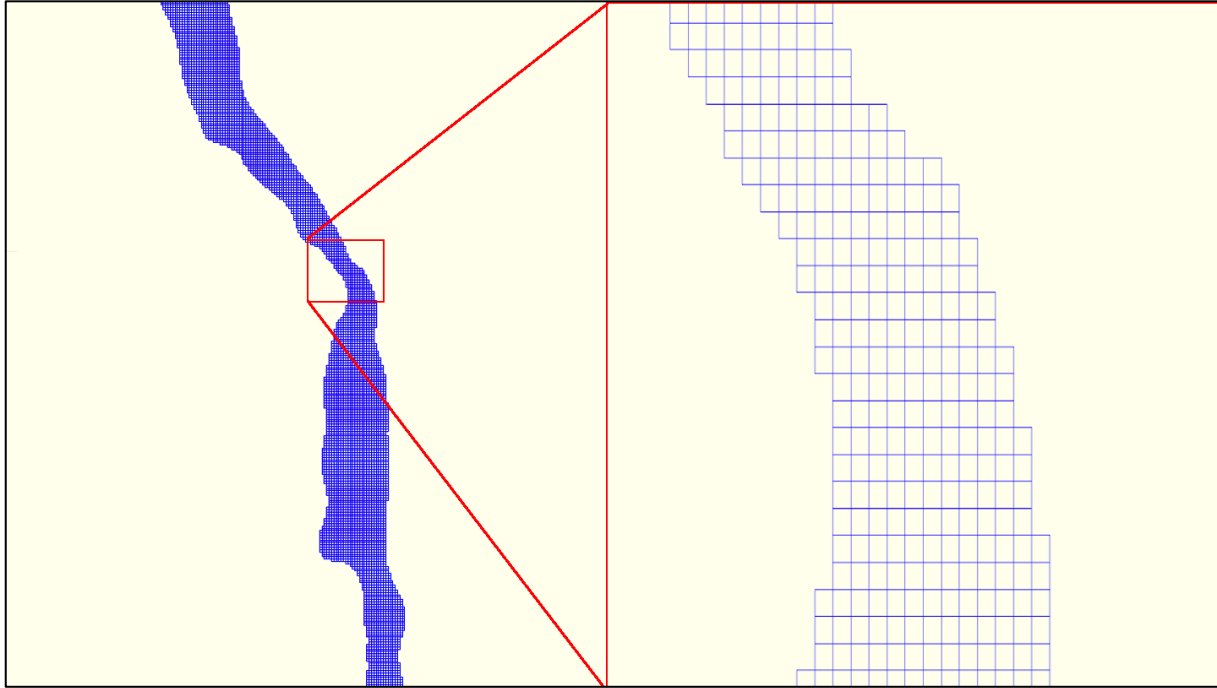


Figure 3.6 High-resolution computational grids (coarse grid: 75 m x 75 m).

At first, the shapefile was divided into 46,203 squares with 75 x 75 m dimensions in a 2D Cartesian grid. Previously, this grid has been used to model the sediment and chemical constituent movement in the LAR by Shalini Kashyap et al. [84]. A part of the computational grid of the model and zoomed view (to show the mesh) can be seen in Figure 3.6.

Though these grids are required to be created to solve the governing equations, the staggered grid is needed (m, n) at each staggered grid, which is different from the numerical grid, and each quantity is defined in a specific place. For example, each numerical grid includes a value for Water Level in the center, but in staggered grids, this value must be interpolated rather than being in the center. The scenario is the same for depth values and velocities. A sample of the staggered grid is presented in Figure 3.7.

We used the grids with 75 x 75 m dimensions as a coarse grid to simulate the entire river from Fort McMurray to Fort McKay in our first simulation for validation. However, the available information for the bathymetry has a 10 to 25 m resolution. Therefore, we can have a more detailed simulation by refining the grids into 25 x 25 m dimensions (three times finer). In our second simulation, we

used finer grids for part of the river that we have high-resolution images for that part. This finer grid can help us to be capable of having a more detailed survey.

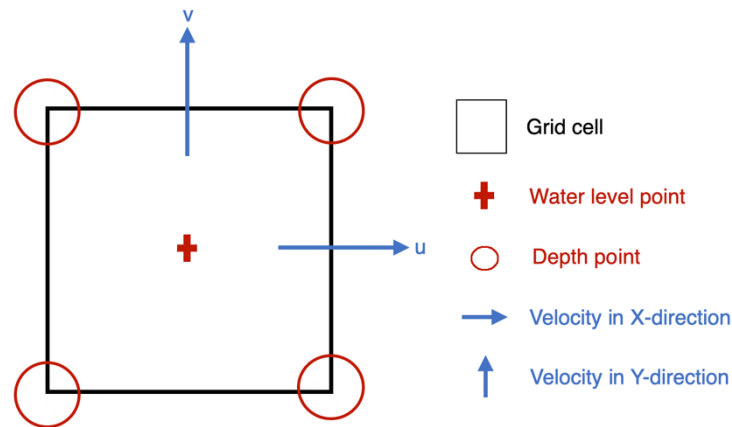


Figure 3.7 Staggered grid in DELFT3D-FLOW

Bathymetry interpolation

To complete the physical characteristics of the grids, the elevation of each grid must be allocated. To create, manipulate and visualize the bathymetry QUICKIN tool could be used. The continuous bathymetry data with 10 to 25 m resolution has been used to allocate the elevation information to each grid. The bathymetry data exist as a .dat file with X coordinate, Y coordinate, and Elevation information. It must be noted that the reference level of the depth is a horizontal plane, and a negative depth value defines a depth above the reference plane. Therefore, the values must be negative. After importing the grid file and the elevation data, the screen looks like Figure 3.8 (upper image). The data were then interpolated onto the model computational grids using the triangular method to create the required model geometry. The triangulation method is the best suited for the data sets with a resolution equal to or smaller than the grid resolution [95]. After the interpolation, QUICKIN allocates each grid cell corner a depth value, and the final file is a .dep file (with the extension <dep>). A sample reach of the river after the depth interpolation is shown in Figure 3.8 (lower image).

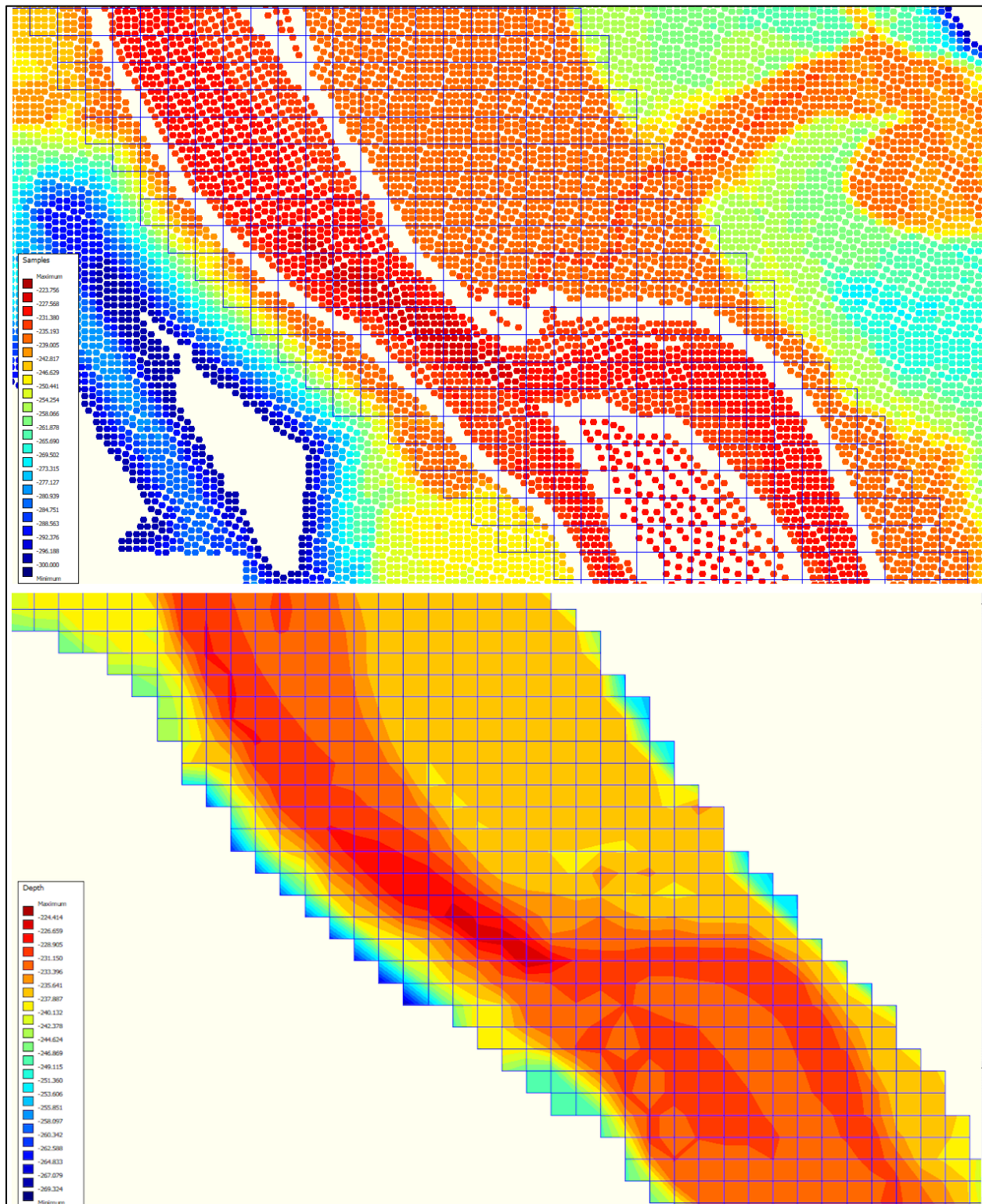


Figure 3.8 Grids and bathymetry data imported in QUICKIN before (upper image) and after triangulate interpolation (lower image). The lower image demonstrates the bathymetry in main channel and flood plain.

3.2.3.2 Flow (Hydrodynamics including morphology window)

In this module, the characteristics of the flow could be defined, and a “Master Definition Flow” file (MDF file) could be built. The following parameters must be considered as input:

Domain

This Data Group contains the following parameters:

- **Grid:** the grid file contains the latitude of the model and the number of layers. The grid file is the output of the RGFGRID module, which contains the meshes and coordinate information. Here we have just one level, and the latitude has been kept equal to zero.
- **Bathymetry:** to define the bathymetry, we used the interpolated depth obtained from the QUICKIN. Depth values have been generated and specified at the cell center by QUICKIN’s default setting.

Time frame

In this section, the “Reference date”, “Simulation start time”, “Simulation stop time” and “Timestep” must be defined. Here we set the following times to simulate the model. Since the available images for the “Remote Sensing” studies were taken on 11th November 2009, we simulate the river for one week, and the simulation start and stop time covers this time in the middle.

Table 3.6 Time frame of the model. The river has been simulated for one week and our study day is in the middle of this week.

Reference date	08 11 2009 00 00 00 [dd mm yyyy hh mm ss]
Simulation start time	08 11 2009 00 00 00 [dd mm yyyy hh mm ss]
Simulation stop time	15 11 2009 00 00 00 [dd mm yyyy hh mm ss]
Time step	0.25 [min]

To satisfy the numerical stability of the model, the Courant Number must be smaller than 10 [94]. Therefore, the time step is controlled by the Courant-Friedrichs-Lewy condition, which is defined by:

$$CFL = \frac{\Delta t \sqrt{gH}}{\{\Delta x, \Delta y\}} \quad \text{Equation 3.6}$$

where

CFL is the Courant Number.

Δt is the time step in seconds.

g is the acceleration of gravity (m/s^2).

H is the (total) water depth (m).

$\{\Delta x, \Delta y\}$ is a characteristic value of the grid spacing in either direction. (minimal value of the grid size)

Here if we consider $\Delta T = 15$ s, $g = 9.81$ m/s^2 , $H = 10$ m, $\{\Delta x, \Delta y\} = \{75, 75\} = 75$ m, the Courant number will be equal to 1.98 [dimensionless] which is an acceptable value.

Even by using finer grid spacing $\{\Delta x, \Delta y\} = \{25, 25\} = 25$ m, the Courant number will be equal to 5.94 which is acceptable.

Initial Condition

The dependent variables, such as water level and flow velocity components (in both directions), must have specified initial values. Here our initial water level is a space varying value taken from the results of another simulation that has been done by Shakibaeinia et al. [84]. The velocity component in the X and Y direction is assumed to be zero.

Boundaries

The model domain's contour is made up of two sections. One is that it runs along "land-water" lines (riverbanks, coastlines), known as closed boundaries, and the second part runs across the flow field, known as open boundaries. Closed boundaries are defined naturally. In this section, open boundaries, their location, and type must be defined.

The flow and transport boundary conditions are necessary at open boundaries. These conditions indicate the effect of the outside world, i.e., the region that is not simulated outside the model area, and it keeps the model updated in time. Our model has the following setting as the boundary condition in Table 3.9. The Discharge and the Water Level values are obtained from the WSC website.

Table 3.7 Boundary Condition for Downstream.

Time dd mm yyyy hh mm ss	Water level Begin (m)	Water level End (m)	Source of data
08 11 2009 00 00 00	232.4	232.4	WSC (Water Survey of Canada)
15 11 2009 00 00 00	231.5	231.5	WSC (Water Survey of Canada)

Table 3.8 Boundary Condition for Upstream.

Time dd mm yyyy hh mm ss	Total discharge (m ³ /s)	Source of data
08 11 2009 00 00 00	620	WSC (Water Survey of Canada)
15 11 2009 00 00 00	177	WSC (Water Survey of Canada)

Table 3.9 The type and location of the Boundary Conditions in upstream and downstream.

Boundaries	Location Cartesian (X,Y)	Label	Type of open boundary (quantity)	Forcing type
Downstream	(469487, 6470518)	07DD011	Water level	Time-series
Upstream	(475439, 6293000)	07DA001	Total discharge	Time-series

Physical parameters

Here, physical parameters such as Hydrodynamic constants, Roughness, and Viscosity could be defined. In this study, gravity, water density, Wall roughness, and Viscosity remained as default. However, Bottom Roughness (n_b), which can be defined with different formulas (Chezy, Manning, and White-Colebrook) as a constant value or a file, can play a significant role in the condition of the problem and change the final water level and velocity values.

The bed roughness characteristics for the Athabasca River are provided in Table 3.10. The values for n_b are obtained from the previous work done by She et al. [96]. However, the bed roughness is mainly affected by the type and size of the materials of the bed and also the shape of the channel. These two components may vary time by time. For instance, the change in water level can alter the shape of the channel, or the material and settled sediment may vary at different times, and the resistance between the ice floes and the border of the river close to the surface will add complexity.

Table 3.10 The Athabasca River's bed roughness characteristics.

From ² (km)	To (km)	Manning coefficient (n_b)
0	296.55	0.030
296.60	300.4	0.020
300.45	319.4	0.030
319.45	400	0.035

However, to simplify these roughness values, Beltaos et al. (2018) used 0.030 and 0.035 below and above 319.4 km from the mouth of the Athabasca River at Lake Athabasca [97]. Therefore, in this study, we defined the Bottom Roughness value as equal to 0.035, and we used the Manning formula. Considering a uniform value for the entire length of the study area is not precise and it will add uncertainty to the numerical model.

Operation

In the LAR, the reach has complicated bathymetry and a thalweg that is unpredictable, and it receives lateral inputs from up to six main tributaries. The Ells, Firebag, MacKay, Muskeg, and Steepbank rivers are among the tributaries examined for model development. The locations of these tributaries have been added to the river. Each tributary has a coordinate, and the flow value is obtained from the WSC website. The location and the discharge of all tributaries (for September 2004) are in Table 3.11.

Monitoring

In our studies, we defined Observation Points and Cross-Sections to validate the results in these points and sections.

Output

Finally, an MDF file with the mentioned settings and numbers has been created and used as an input for the START module. The D-HYDRO engine has done the calculations, and it took almost two hours. The calculation time depends on the number of grids, time step, and grid size.

² Distance from the mouth of the Athabasca River at Lake Athabasca

Table 3.11 The flow on the start and end date of the simulation for main Athabasca River tributaries.

Tributary (Station)	Location, Cartesian (X,Y)	Label	Flow – start (m ³ /s)	Flow – end (m ³ /s)
Ells	(456928.433, 6347420.147)	07DA017	7.15	7.15
Firebag	(487907.559, 6389883.323)	07DC001	29.28	29.28
MacKay	(458014.123, 6341016.834)	07DB001	16.99	16.99
Muskeg	(465543.318, 6338813.211)	07DA008	4.74	4.74
Steepbank	(475285.455, 6317397.667)	07DA006	6.04	6.04

CHAPTER 4 RESULTS CALIBRATION, VALIDATION, AND EVALUATION

4.1 Hydraulic model

4.1.1 Calibrating Delft3D hydraulic model

To calibrate the model, we have to define the parameters that affect the model's outputs. Our model is sensitive to the manning coefficient (n_b) in this study. However, previously, it has been mentioned that some studies have been done by She et al. [96] to measure the bed roughness in the Athabasca River. Therefore, we used the proposed value for the bed roughness.

4.1.2 Validating Delft3D hydraulic model with collected water level and depth-averaged velocity data

To validate the hydraulic model results, outputs like water level and depth-averaged velocity must be compared to the real data in different cross-sections. Since there are no measured values precisely on the same day that the model is based on, the model's reliability can be tested by comparing the results with measurements that have been done on another day. We tried to set a hydraulic model based on available information in November 2009. However, the available measured data was collected on the 15th and 16th of September 2004 by the Canadian Council of Ministers of the Environment (CEMA) [92]. Therefore, the model has been set up with the hydrometric data of September 2004. These four cross-sections do not cover the area that we have images for; however, they evaluate the model's functionality. It must be mentioned that the behaviour of the river in September 2004 is not the same as its behaviour in November 2009. This can add some uncertainty to our model, but due to the limitations that already exist in obtaining a proper image, we have to decide based on the available data that we have.

4.1.2.1 Model parameters for validation

Table 4.1 The hydrometric data obtained from the WSC as a boundary condition for downstream (from 13 September 2004 to 18 September 2004).

Time dd mm yyyy hh mm ss	Water level Begin (m)	Water level End (m)	Source of data
13 09 2004 00 00 00	211.6	211.6	WSC (Water Survey of Canada)
18 09 2004 00 00 00	211.603	211.603	WSC (Water Survey of Canada)

Table 4.2 The hydrometric data obtained from the WSC as a boundary condition for upstream (from 13 September 2004 to 18 September 2004).

Time dd mm yyyy hh mm ss	Total discharge (m ³ /s)	Source of data
13 09 2004 00 00 00	1100	WSC (Water Survey of Canada)
18 09 2004 00 00 00	1090	WSC (Water Survey of Canada)

Table 4.3 The hydrometric data for the main tributaries of the Athabasca River (from 13 September 2004 to 18 September 2004).

Tributary (Station)	Location, Cartesian (X,Y)	Label	Flow – start (m ³ /s)	Flow – end (m ³ /s)
Ells	(456928.433, 6347420.147)	07DA017	7.15	7.15
Firebag	(487907.559, 6389883.323)	07DC001	20.9	21.8
MacKay	(458014.123, 6341016.834)	07DB001	1.42	1.95
Muskeg	(465543.318, 6338813.211)	07DA008	0.703	1.14
Steepbank	(475285.455, 6317397.667)	07DA006	1.84	2.05

4.1.2.2 The comparison between the estimated and measured values for water level and velocity in available cross-sections

The following plots demonstrate the water level and depth-averaged velocity in four cross-sections.

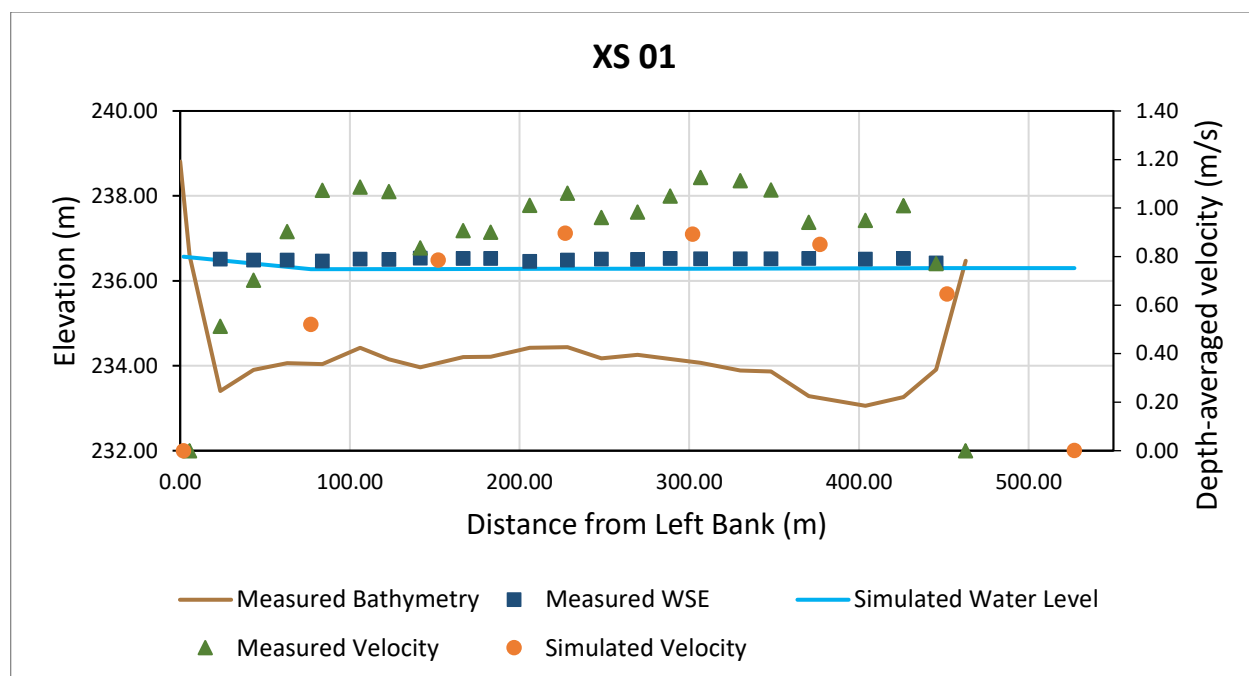


Figure 4.1 Validation of the Delft3D hydraulic model with collected water level and velocity data for the cross-section 01 in September 2004.

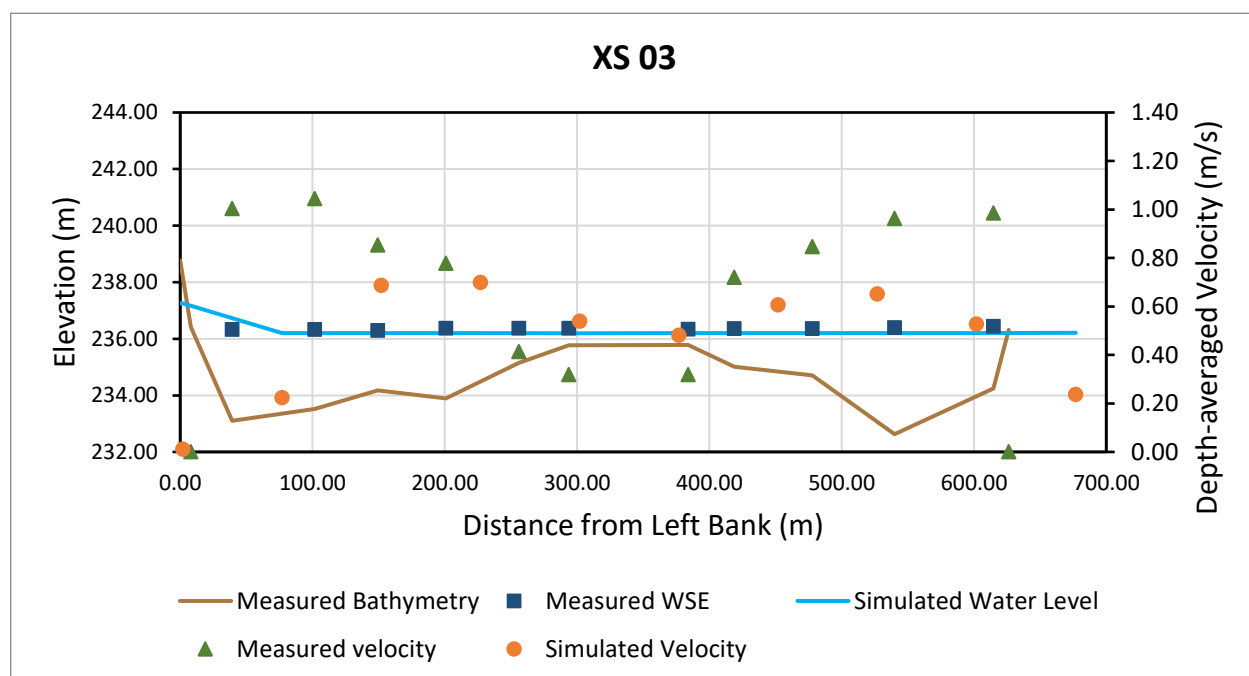


Figure 4.2 Validation of the Delft3D hydraulic model with collected water level and velocity data for the cross-section 03 in September 2004.

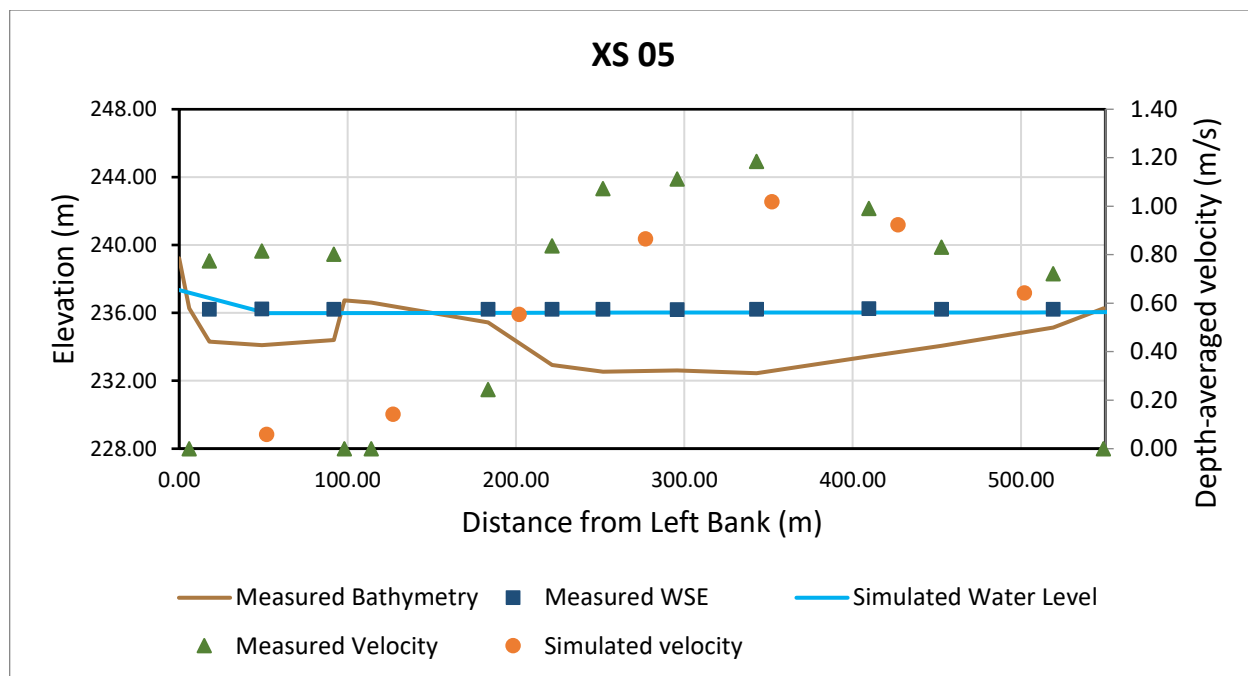


Figure 4.3 Validation of the Delft3D hydraulic model with collected water level and velocity data for the cross-section 05 in September 2004.

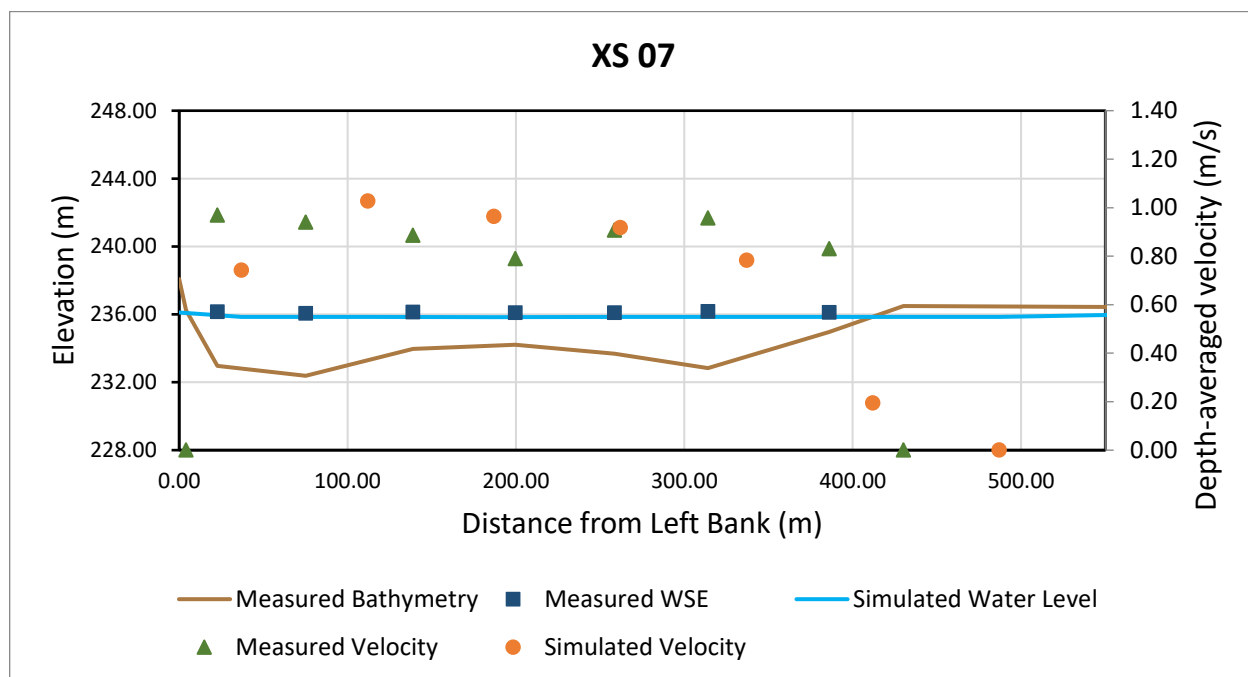


Figure 4.4 Validation of the Delft3D hydraulic model with collected water level and velocity data for the cross-section 07 in September 2004.

4.1.2.3 Interpretation of the comparison between the estimated and measured values

This comparison ensures that the variables across the river follow the same trend. The following plots show four cross-sections and the comparison between measured data and simulated components. The figures (from Figure 4.1 to Figure 4.4) show a similar water level compared to measured data and simulated values. Besides, the water level trend at different distances from the Left Bank is correct, and the results seem rational. Also, the figures demonstrate a high level of similarity between the simulation and real data in depth-averaged velocity. However, there are discrepancies between the values, and they are not exactly the same. These incompatibilities could be due to the rough assumption (not exact values) of the bed level in the simulation. However, the depth-averaged velocity follows the same trend in each cross-section.

4.1.3 Reynolds number calculation

The Reynolds number is a dimensionless value that represents the ratio of inertial force to viscous force and can be calculated by the following formula:

$$Re = \frac{\rho VD}{\mu} = \frac{VD}{\nu} \quad \text{Equation 4.1}$$

where

ρ is fluid density (kg/m³)

V is the fluid velocity (m/s)

D is the characteristic linear dimension (m)

μ is the dynamic viscosity (Pa.s)

ν is the kinematic viscosity (m²/s)

Using the values provided in Table 4.4, the Reynolds number for this situation in this river will be approximately equal to 300000. The flow can be divided into three types based on the Reynolds number. Table 4.5 shows different flow types and their corresponding Reynolds number. Hence, we can conclude that our flow is turbulent like most natural river's flow [98].

Table 4.4 Physical Parameters of the water for measuring the Reynolds number.

Parameter	value	unit
Water density	1000	kg/m ³
Dynamic viscosity	1.5673	mPa.s
Kinematic viscosity	1.5673	mm ² /s

Table 4.5 Reynolds number for different types of flow regimes in open channel flow.

Flow type	Reynolds number
Laminar	$Re < 500$
Turbulent	$Re > 2000$
Transition flow	$500 < Re < 2000$

4.1.4 Converting the depth-averaged velocity to water surface velocity

The velocity profile in open channel flow (e.g., river) varies depending on the depth (Figure 4.5), and in turbulent flow, it follows the wall known as logarithmic velocity distribution. To convert the velocity in one depth to another, depth conversion is needed. We can consider the following method for conversion, and we define a variable coefficient (α) by the following formula:

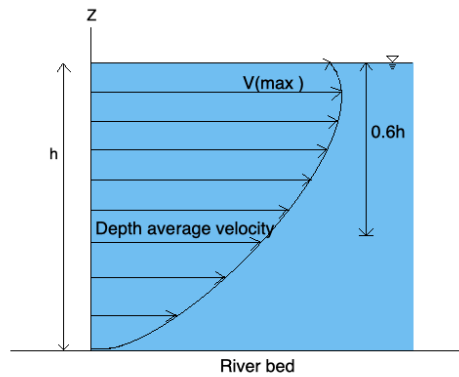


Figure 4.5 Velocity profile in open channel flow.

The velocity profile (in a very simple way) follows a logarithmic relation given by:

$$V_z = V_{max} \left(\frac{z}{h} \right)^{1/3} \quad \text{Equation 4.2}$$

Which is a simplified formula to explain the velocity profile depending on the height of the flow. In this formula, the maximum velocity happens at the water surface, which is not exactly true. We know that maximum velocity occurs close to the surface; nevertheless, by considering the maximum velocity at the river's surface, the "depth-averaged velocity" is observed to be equivalent to 0.79~0.84 times the water surface velocity ($\alpha = 0.79 \sim 0.84$) [99] [100]. Hence, an approximate surface velocity can be obtained by dividing the obtained depth-averaged velocities by α .

$$\text{Water Surface Velocity} = \frac{\text{Depth - averaged Velocity}}{\alpha}$$

Obtaining the best value for α and applying this value to the entire river is challenging.

Hence, we have decided to use a more reliable formula, a function of depth and bed shear stress for each point.

The velocity follows the following formula depending on the depth of the flow [101]:

$$u = \frac{u_*}{k} \ln \left(\frac{y}{k_s} \right) + 8.5 \quad \text{Equation 4.3}$$

where:

u is the longitudinal velocity (m/s)

u_* is the shear velocity (m/s), and it is equal to $\sqrt{\frac{\text{bed shear stress}}{\text{density of water}}}$

k is the Von Karman constant (typically equal to 0.41) [102] [94]

k_s is the equivalent sand-roughness height of the channel bed (m)

y is the vertical distance above the channel bed (m)

The depth-averaged velocity can be calculated by integration over Y-axis, and we reach the following formula:

$$u_{average} = \frac{u_*}{k} \ln \left(11.0 \frac{h}{k_s} \right) \quad \text{Equation 4.4}$$

where

h is flow depth

If we replace y with h at the water surface, the surface velocity will be obtained by the following formula:

$$u_{surface} = \frac{u_*}{k} \ln \left(30.1 \frac{h}{k_s} \right) \quad \text{Equation 4.5}$$

To calculate the ratio between water surface velocity and depth-averaged velocity, we divided $u_{surface}$ to $u_{average}$. The following ratio is the coefficient (α) to convert the depth-averaged velocity to the water surface:

$$\frac{u_{surface}}{u_{average}} = 1 + \sqrt{\frac{f}{1.28}} \quad \text{Equation 4.6}$$

Where

f is the Darcy-Weisbach friction factor equal to $8 * \left(\frac{u_*}{u_{average}} \right)^2$

Therefore, we calculated $\frac{u_{surface}}{u_{average}}$ ratio for all points to convert the depth-averaged velocity to

water surface velocity. This ratio is between 1.1468 and 1.8245 for the points with a considerable magnitude of velocity and bed shear stress.

However, it is needed to be mentioned that, however, this method is commonly being used to convert the velocities in different depths to another depth, the basic hypothesis which considers the water surface velocity is equal to ice floes' velocity is a rough consideration. The existence of the ice floes on the water surface will add some interactions between ice and water and the water does not follow the behaviour of a free surface open channel anymore.

4.2 Remote sensing

4.2.1 Dry surface

By comparing the border of the river in an unfrozen condition (which has been used to define the river's boundary in DELFT3D) with the obtained images, we can see that some parts of the river surface (close to the border and in the middle) there are some dry areas (the related images has been provided in APPENDIX B). These areas do not exist in the images taken earlier in summer (July 2009), but they appeared on the surface from September that year. Therefore, it seems that these areas are where the sediment has been deposited due to the small velocity or shallow water depth.

This condition has not been considered in the numerical model, and it can affect the flow characteristics considerably. By the existence of these dry areas, our accessibility to the water surface velocity has been limited. This condition can happen close to the boundary and to the islands where the flow is shallow, and examples have been provided in APPENDIX C.

4.2.2 Error elimination

4.2.2.1 Filtering the results based on their movement direction

There is no specific way to filter the results and eliminate the errors. However, in this study, due to the upward direction of the flow (from downstream to upstream), the most reliable filter to eliminate the errors could be the flow direction. All velocity vectors must have a positive “dy”. If a point shows movement in the downward direction, this point has been matched incorrectly by the CIAS, and it has to be eliminated.

4.2.2.2 Filtering the results based on their correlation

Another method to filter the results is the correlation between a point (in the first image) and the assigned one (in the second image). We can measure the matching level and connectivity using the “ C_{\max} ” (maximum correlation coefficient) and “ C_{avg} ” (average correlation coefficient) for each match that the CIAS provides. There is no particular recommendation for using these two parameters to find the best matches and remove possible mismatches.

Some possible methods are:

- I. Define a threshold on the C_{\max}
- II. Define a threshold on the ratio between C_{\max} and C_{avg} , which is called SNR (Signal_to_Noise ratio)
- III. Define a threshold on both the C_{\max} and C_{avg} .
- IV. Define a threshold for the difference between C_{\max} and C_{avg} .

Although these methods are being used to eliminate the errors, they cannot eliminate all the mismatches and keep all the correct matches. Therefore, we decided to check the performance of these methods by applying them to the first series of points. Since we have the valid value of the velocity for each point, we can detect and evaluate the functionality of these methods. In the following, the first, the second, and the fourth method are explained in detail, and their functionality has been evaluated.

I. Define a threshold on the C_{\max}

As expected, the higher the C_{\max} , the better and more reliable the results will be. For instance, Kumari et al. set this value equal to 0.9 in their study to obtain glacier velocity [103]. We decided to put this threshold to 0.6 to keep more ice floes in this study. As it is evident, the existed outliers have been eliminated automatically by setting this threshold. Almost 30 % of the results have been eliminated, and just 50% are actual errors. Therefore, it is worth mentioning that using this method will eliminate some acceptable data with small values of C_{\max} .

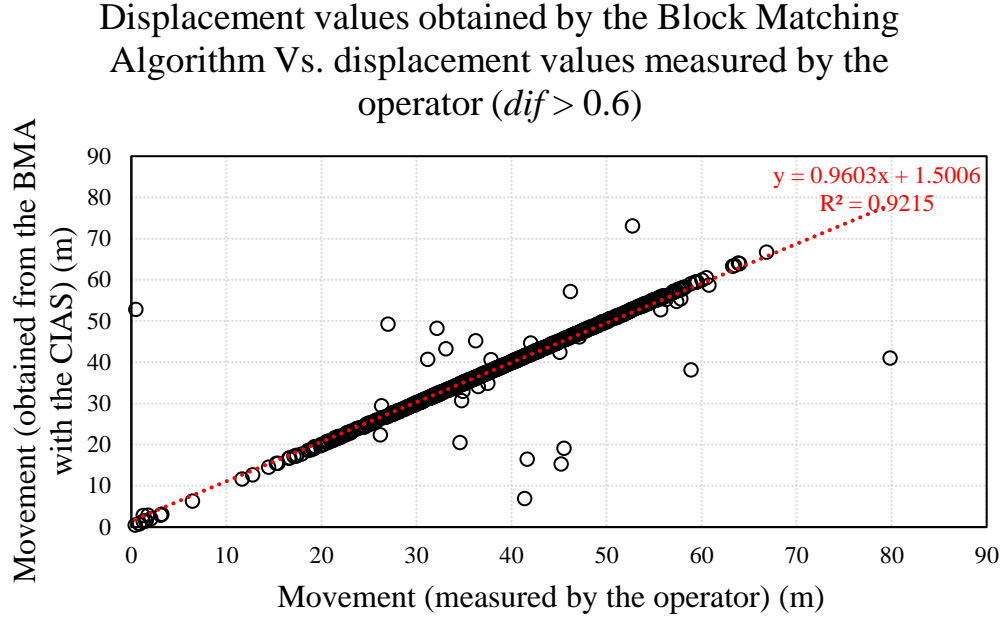


Figure 4.6 The movement value of the ice floe obtained by the CIAS plotted against the expected movement value of the ice floe obtained manually for the points with $C_{max} > 0.6$.

II. SNR

Based on the definition of the SNR , a greater value for SNR shows a more reliable match, and the smaller SNR shows a mismatch. However, this value on its own cannot be a suitable filtering method to eliminate all the errors and keep all the well-matched points [61]. In our study, the SNR is between 6 and 35, and only small numbers of our points have $SNR > 25$ (which is almost 0.1% of the data). Hence, we have to reduce the threshold. By lowering the limitations and changing the threshold to 15, 30% of the total matches could be acceptable. It means that 70% of the matches are mismatched, which is against reality. In conclusion, this method does not seem like a proper method. It is worth mentioning that most of the mismatches have an SNR of less than 10.

$$SNR = \frac{C_{\max}}{C_{\text{avg}}}$$

Equation 4.7

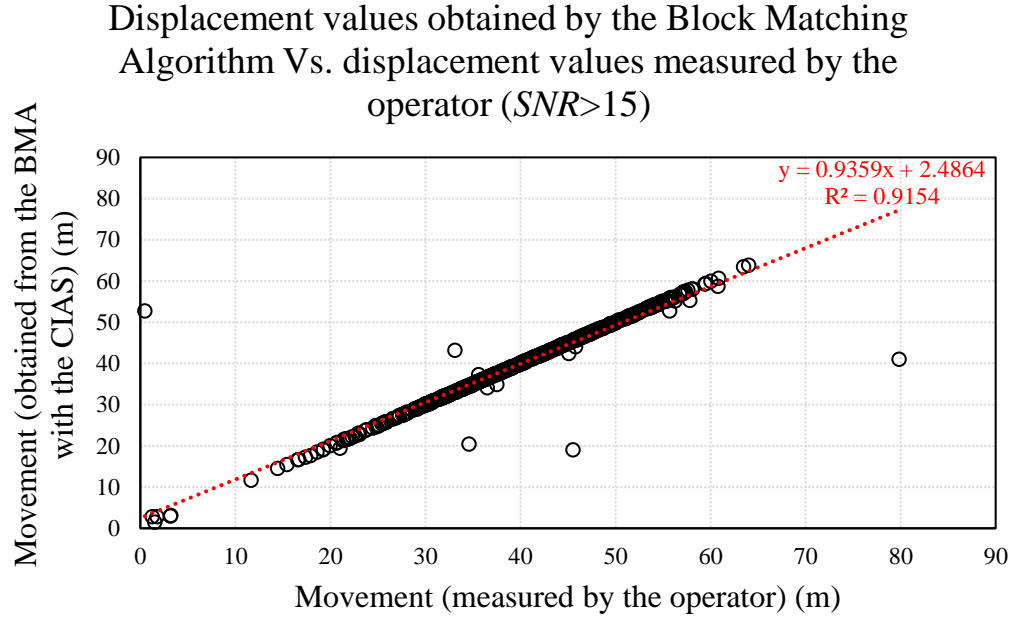


Figure 4.7 The movement value of the ice floe obtained by the CIAS plotted against the expected movement value of the ice floe obtained manually for the points with $SNR > 15$.

III. Define a threshold on both the C_{\max} and C_{avg} .

IV. Define a threshold on the difference between C_{\max} and C_{avg} .

There is no specific limitation for this value [61], but more significant values lead to better connectivity, and the range of this value in our results is between 0.2 and 0.936. If matches with $C_{\max} - C_{\text{avg}}$ greater than 0.6 is considered to have a good match, almost 62% of the results satisfy this condition.

$$dif = C_{\max} - C_{\text{avg}}$$

Equation 4.8

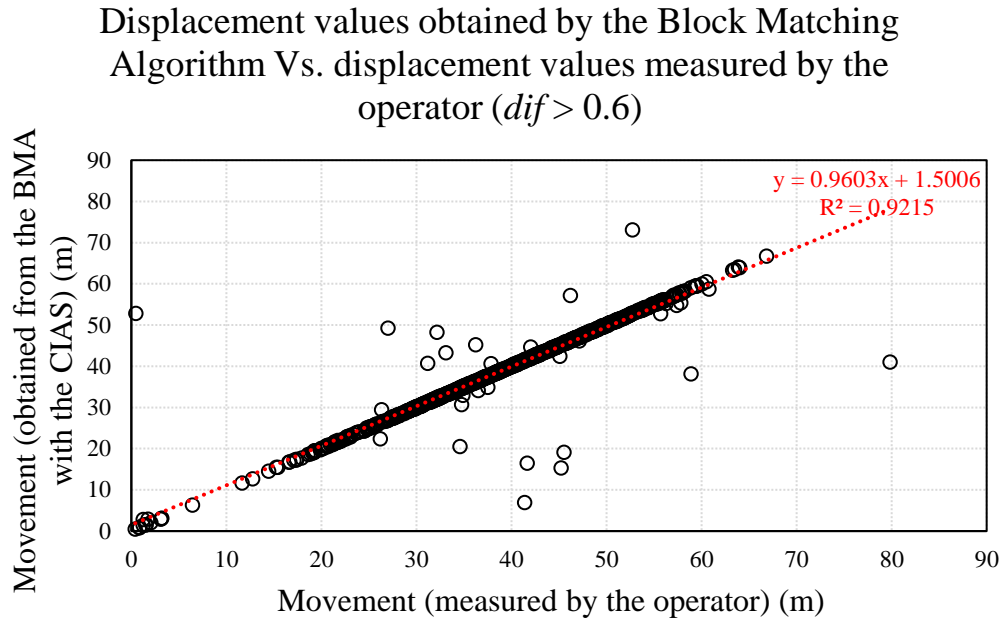


Figure 4.8 The movement value of the ice floe obtained by the CIAS plotted against the expected movement value of the ice floe obtained manually for the points with $dif > 0.6$.

However, the mentioned methods are not used in this study because they eliminate considerable numbers of correct matches and keep some erroneous matches. Hence, to avoid this and keep the correct matches as much as possible, we conclude that operator interaction is needed [44].

As explained earlier, we have two series of points for measuring the ice floes. Here, we used the first series to check the performance of our model and the effect of applying different filters for error elimination. The number of ice floes in this series is limited, and the operator could measure the expected movement values. However, the second series of ice floes contains more than 19000 points (before the process), and the operator cannot measure the expected values of the movement. Therefore, we do not have such a source to evaluate the functionality of these methods.

Finally, in this study, due to the upward direction of the flow, we eliminated the mismatches by their velocity direction in the Y direction. Also, the remaining mismatches have been recognized and eliminated manually. Now, we can compare the results to see the RS's functionality in different situations. The remaining data have a mean of C_{\max} equal to 0.75.

It is worth mentioning that the mismatches are mainly located at the following locations:

- close to the river's boundary (close to the plain when the water depth is shallow)
- in meanders

- when there is a reduction in the width of the channel and ice aggregation
- close to the dry surface.

4.2.3 Smoothing the results

After eliminating the erroneous matches, the results must be smoothed. This smoothness can reduce the effect of remaining errors and mismatches in the remaining points. We used a 3×3 moving window median filter in this study. The following images show the final velocity values across the river (Figure 4.9).

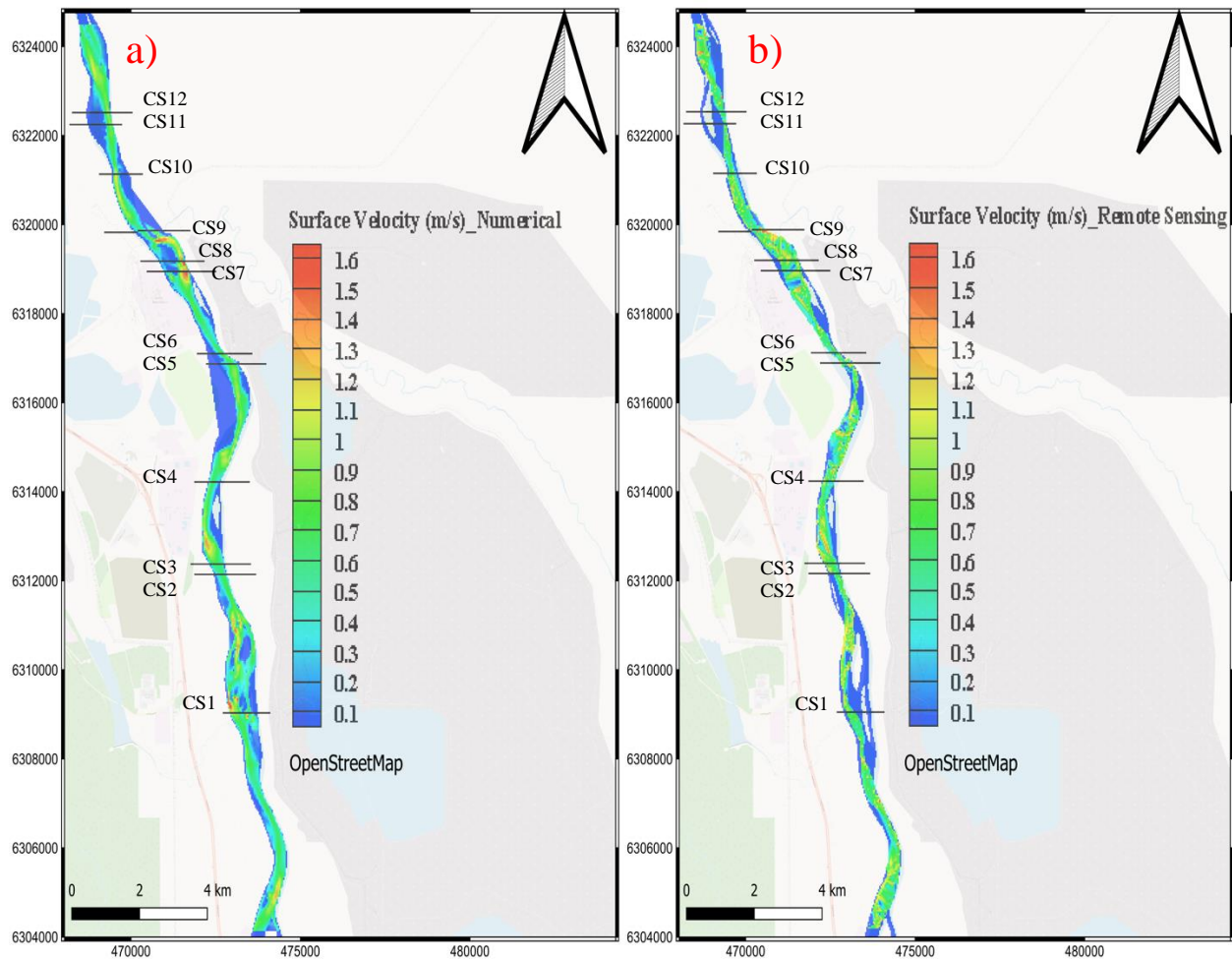


Figure 4.9 Velocity values (m/s) were obtained from a) the numerical model (DELFT3D), and b) the remote sensing method (CIAS).

4.3 Result comparison

To compare the velocities measured by the CIAS with the velocities simulated by DELFT3D, we chose 12 cross-sections to demonstrate the contour of velocity over these cross-sections. These cross-sections have been chosen based on their characteristics. We separated the cross-sections which are able to display and compare different situations (e.g., narrow/wide width, great/small velocity, braided/ straight geology, etc.). Before comparing the results, it has to be mentioned that the velocity simulated by the DELFT3D is the “depth-averaged velocity”; however, the ice floes have been used to measure the water surface velocity. Hence, the depth-averaged velocity had to be converted.

4.3.1 Comparing the results in different cross-sections

To demonstrate the similarities and differences between the obtained velocities, we chose twelve cross-sections to compare their velocity and show the bed level and water level in these cross-sections for a better understanding of the differences. In the following, the plots and their explanations are presented.

4.3.1.1 Cross-Section 2 and Cross-Section 3

In these cross-sections, the flow is experiencing a normal situation, without acceleration or deceleration in velocity. The section is straight without any island or a dry area. The ice floes are moving normally, and there is no ice aggregation.

Figure 4.10 and Figure 4.11 show a good agreement between the velocities obtained by the numerical model and the velocities obtained from the images. The velocities of the ice floes are very close to the values obtained from the numerical model. The value of the RMSE in cross-section 2 is equal to 0.1, and in cross-section 3 is equal to 0.08.

However, since the ice floe detection close to the boundaries is challenging, there are several disagreements on the right and left sides of the river. This disagreement happens due to the mismatches in the remote sensing method (it is challenging for the BMA to detect ice floes close to the border). The mismatches have been eliminated and replaced by zero.

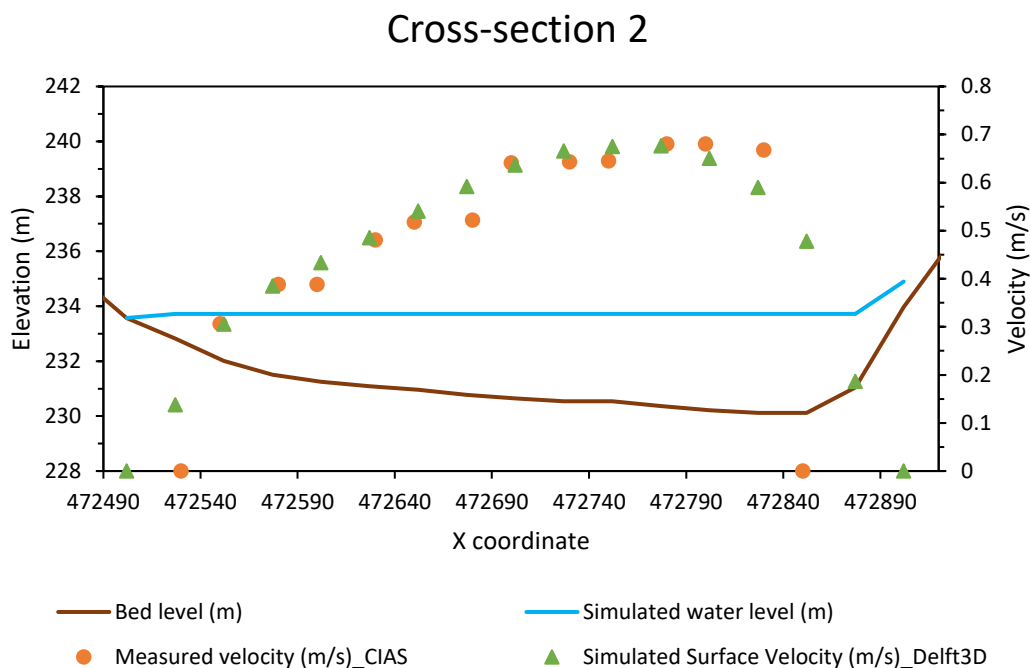


Figure 4.10 Simulated water level and comparison of simulated and measured surface water velocity in Cross-Section 2.

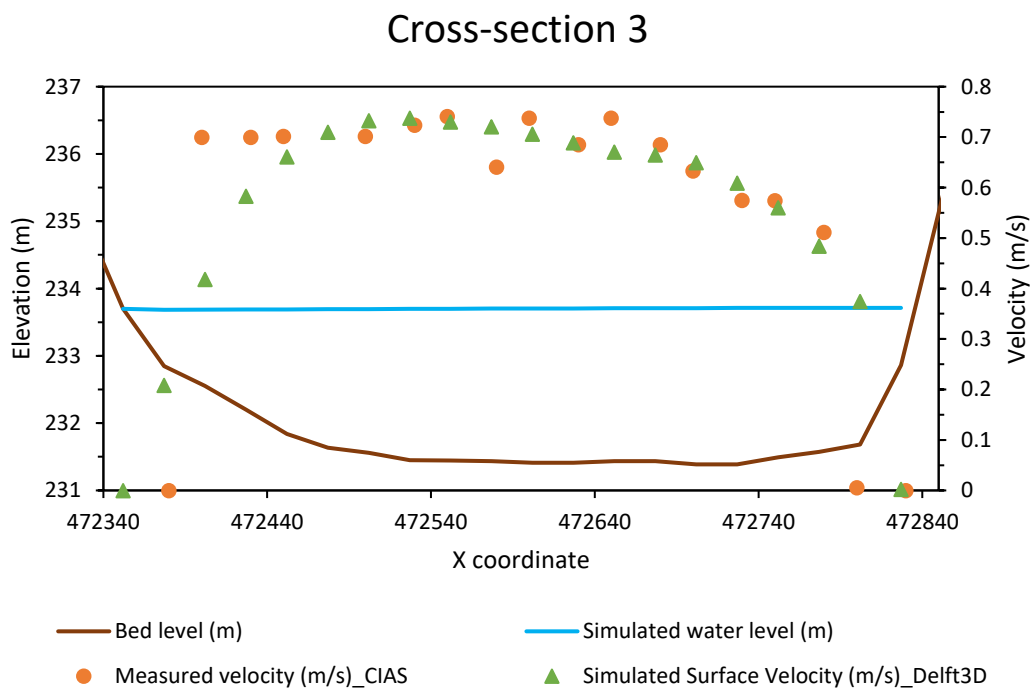


Figure 4.11 Simulated water level and comparison of simulated and measured surface water velocity in Cross-Section 3.

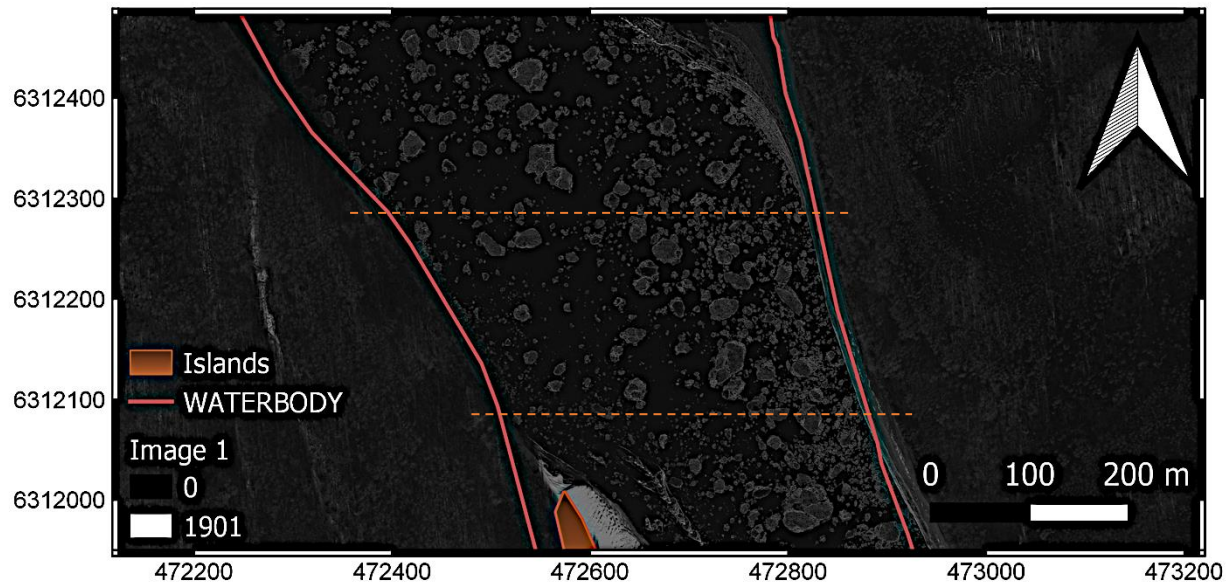


Figure 4.12 Satellite image (cross-section 2 and 3: $Y=6312072.5$ and $Y=6312297.5$)

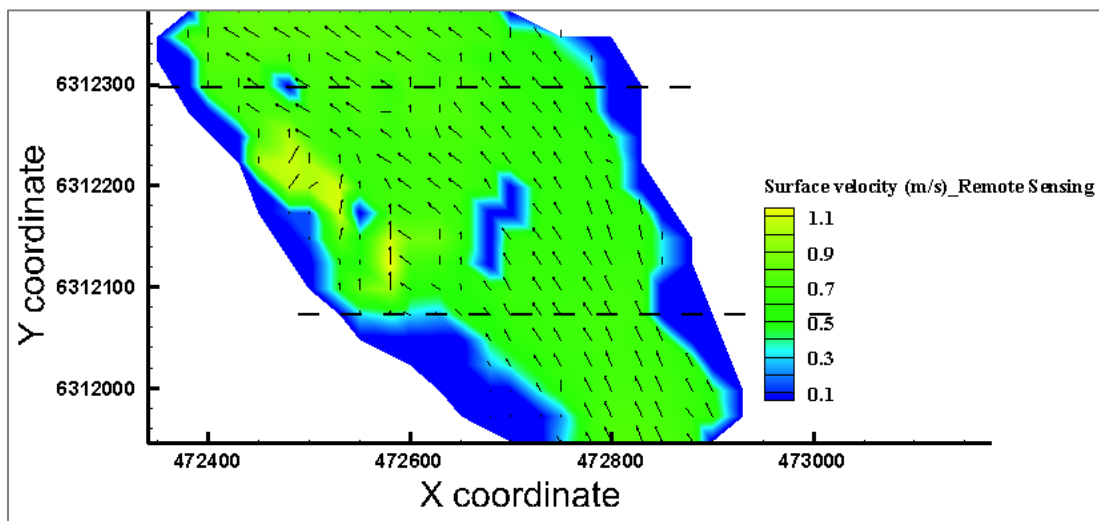


Figure 4.13 Velocity of the river obtained by remote sensing method (cross-section 2 and cross-section3).

4.3.1.2 Cross-Section 4

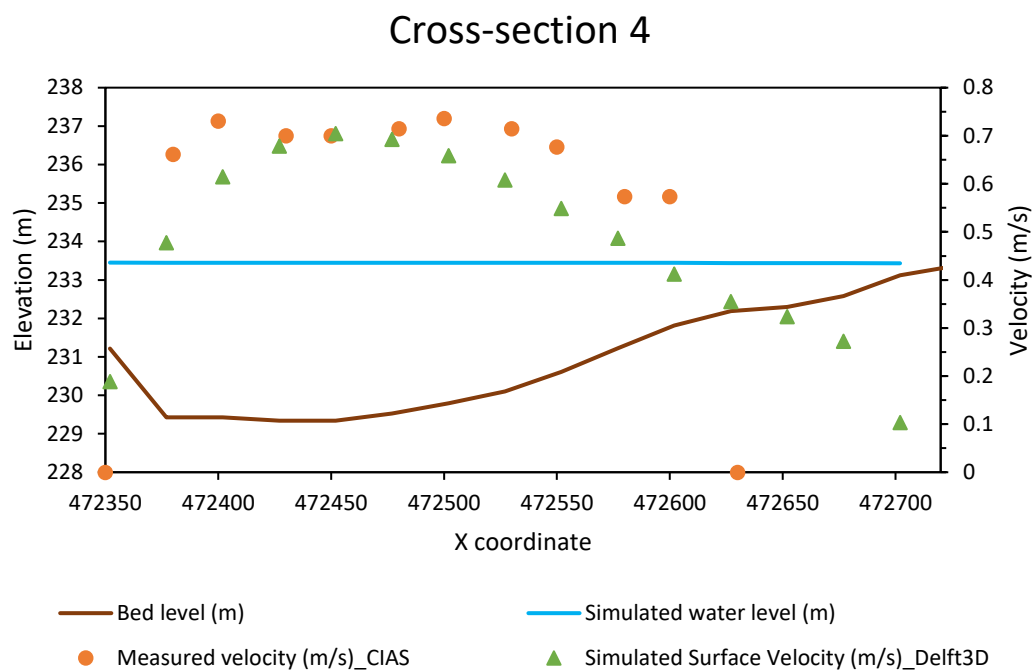


Figure 4.14 Simulated water level and comparison of simulated and measured surface water velocity in Cross-Section 4.

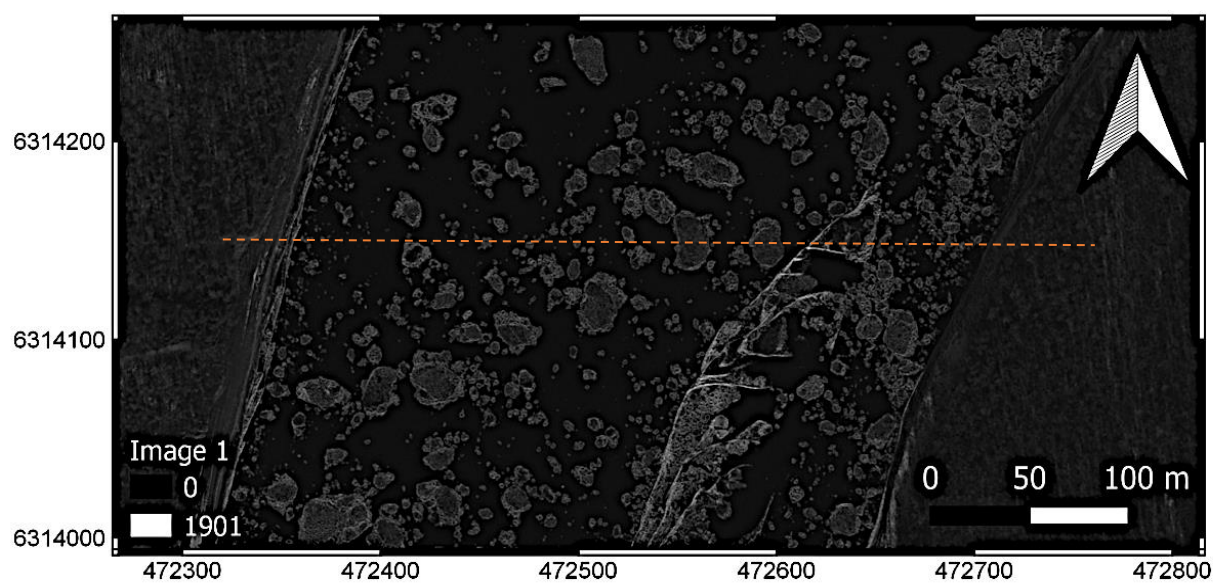


Figure 4.15 Satellite image for cross-section 4: Y=6314147.5.

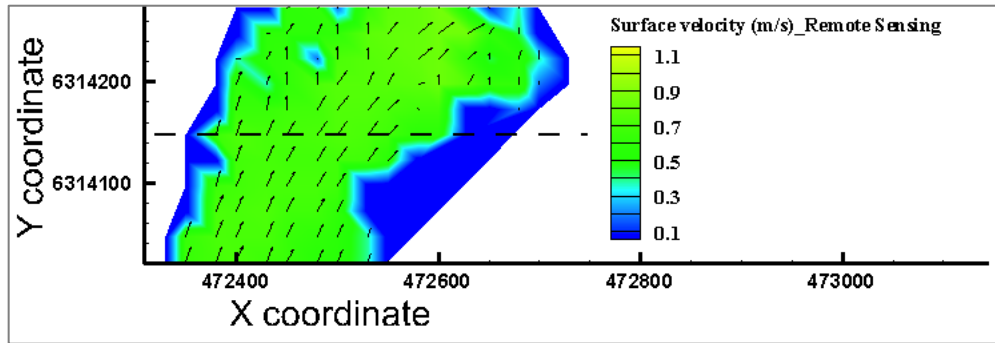


Figure 4.16 Velocity of the river obtained by remote sensing method (cross-section 4).

In this cross-section, there is a steady ice parcel close to the right side of the river (from X=472614 to X=472652). This ice parcel did not change the flow characteristic a lot. On the left side, the flow is normal; the remote sensing results and the numerical model agree well but are not precisely equal. The value of the RMSE in cross-section 4 is equal to 0.1.

This inequality could be the effect of the size and weight of ice floes which affects their velocity. However, on the right side of this stable frozen object, due to the narrow channel (50 m), the ice floes are very small and close to each other, some rotated, and it causes the remote-sensing to make mistakes and unreliable results (all the obtained velocities have been eliminated).

4.3.1.3 Cross-Section 1

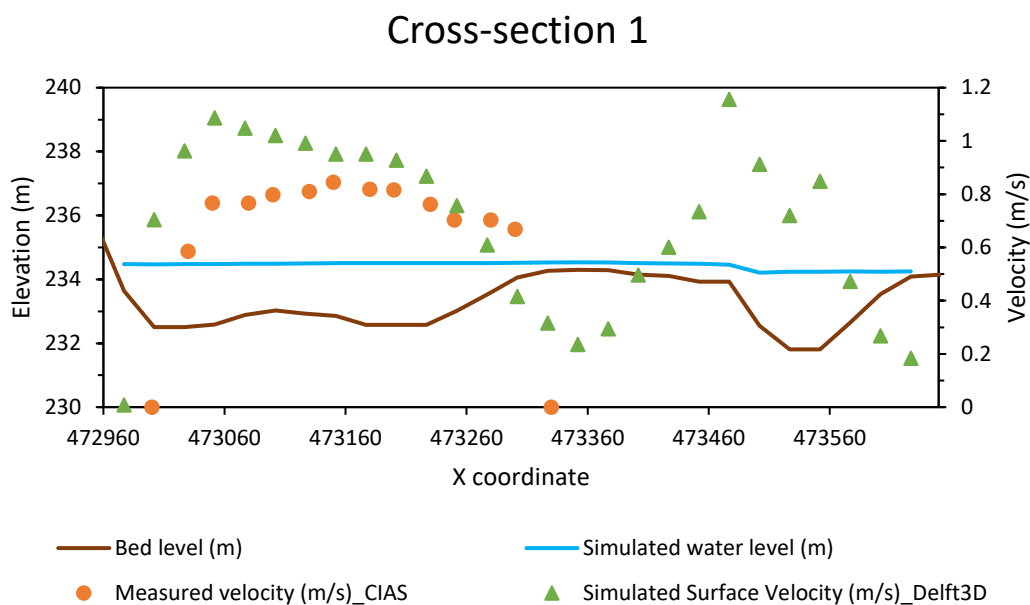


Figure 4.17 Simulated water level and comparison of simulated and measured surface water velocity in Cross-Section 1.

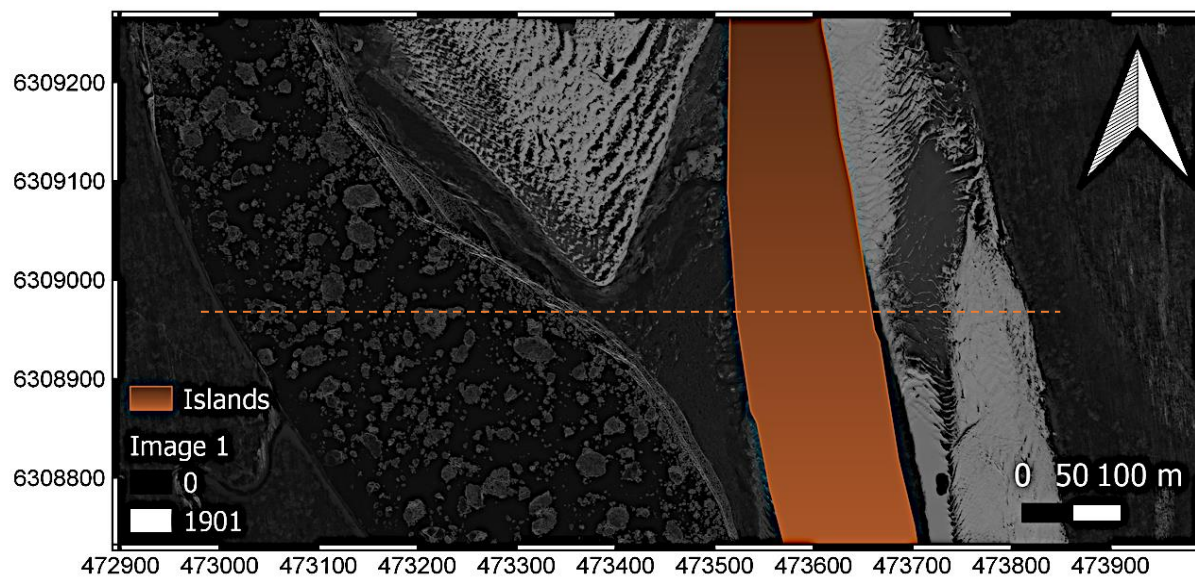


Figure 4.18 Satellite image for cross-section 1: Y=6308972.5.

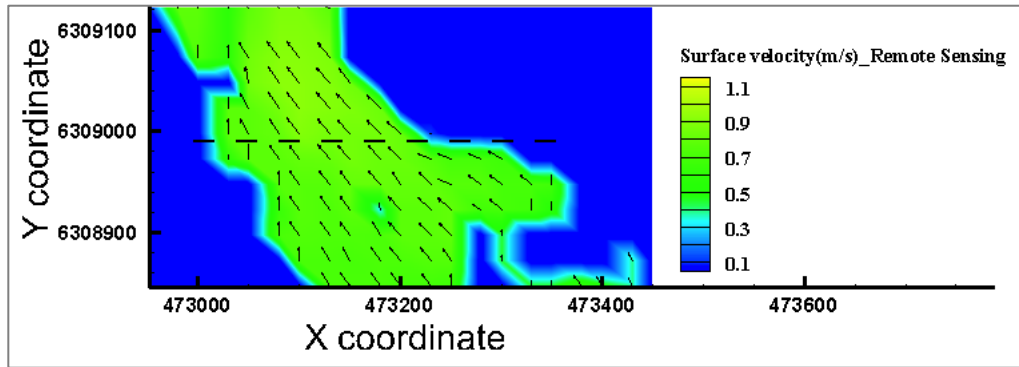


Figure 4.19 Velocity of the river obtained by remote sensing method (cross-section 1).

In this cross-section, there is an island close to the right side of the river. The width of the channel on the right side of the island is almost 150 m, yet the numerical model shows great velocity there; the images prove that this section is frozen (or filled with sediment), and the velocity on the surface is equal to zero. The value of the RMSE in cross-section 1 is equal to 0.2, which is greater than the RMSE in the previous cross-sections.

On the left side of the island, we can compare two series of velocities. Close to the boundary and close to the island, due to the shallow water and higher chance of mismatches, the velocity obtained by the remote-sensing is equal to zero. From the point (473352,6308972.5), the dry area appears in the images (yet the velocity is equal to 0.23 m/s in the model). The depth of water on that point has been estimated to be equal to 23 cm. With this small value, the existence of the settled sediment (dry surface) is rational.

4.3.1.4 Cross-Section 5

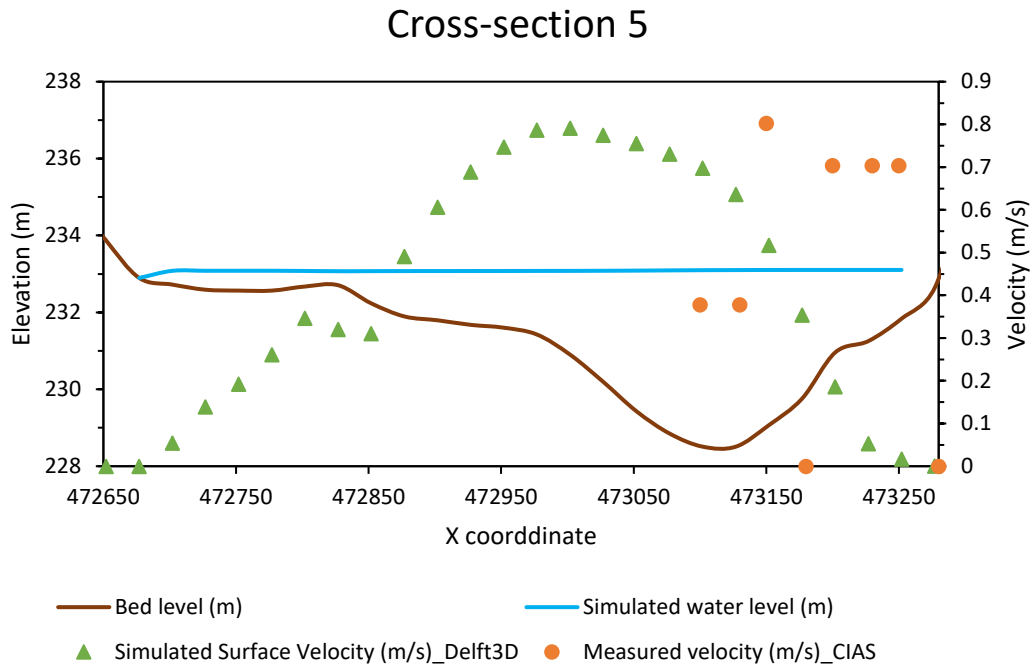


Figure 4.20 Simulated water level and comparison of simulated and measured surface water velocity in Cross-Section 5.

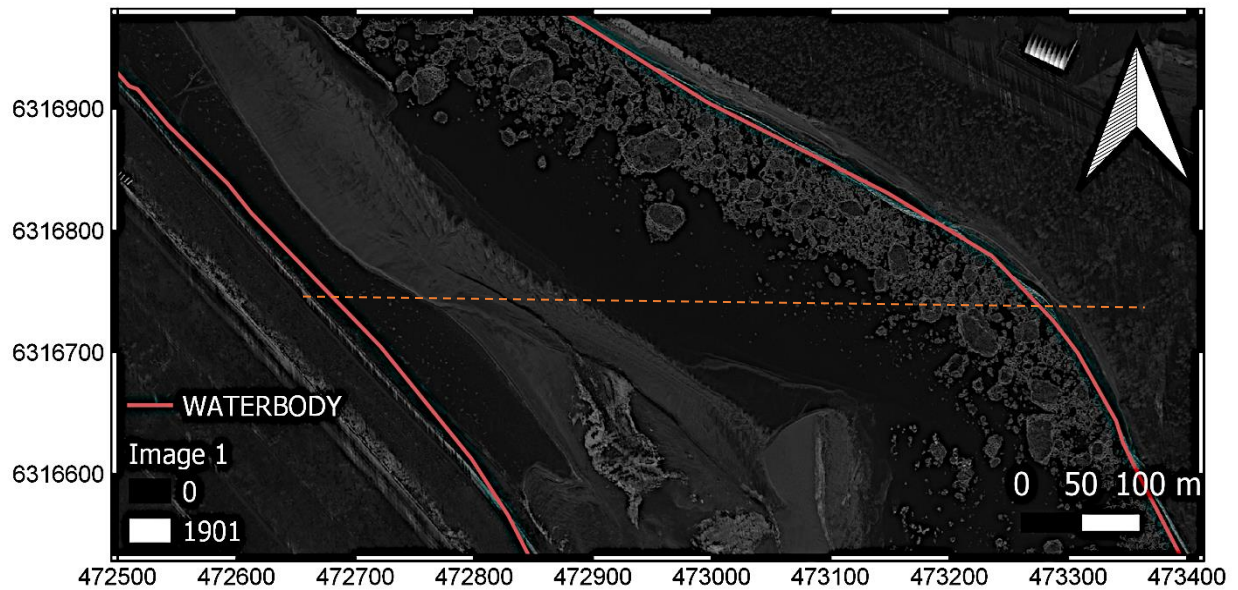


Figure 4.21 Satellite image for cross-section 5: Y=6316747.5.

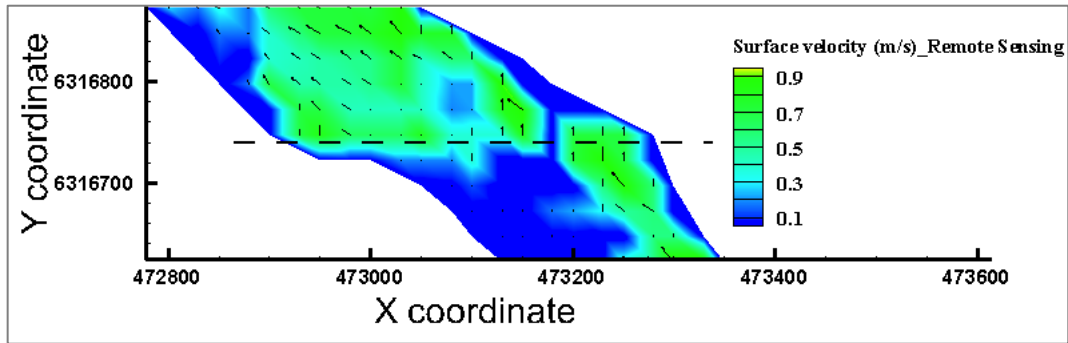


Figure 4.22 Velocity of the river obtained by remote sensing method (cross-section 5).

In this cross-section, the flow path is not straight and braided. It makes the ice floes aggregated on the right side of the river, and the left side of the river is free of ice floes. Therefore, the velocities obtained from the left side are not reliable and eliminated. Also, on the right side of the river, due to the ice aggregation, rotation of ice floes, and ununiform movement for ice floes, the results of BMA are not reliable, and they have a huge difference from the velocities obtained by the numerical model. The value of the RMSE in cross-section 5 is equal to 0.43, which makes the results unreliable.

4.3.1.5 Cross-Section 6

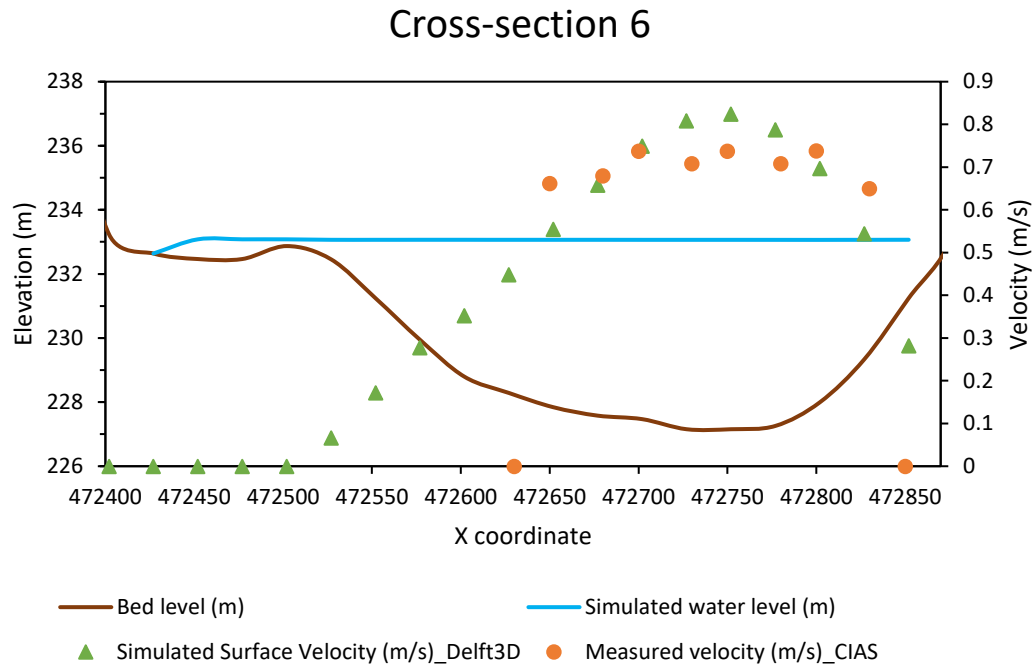


Figure 4.23 Simulated water level and comparison of simulated and measured surface water velocity in Cross-Section 6.

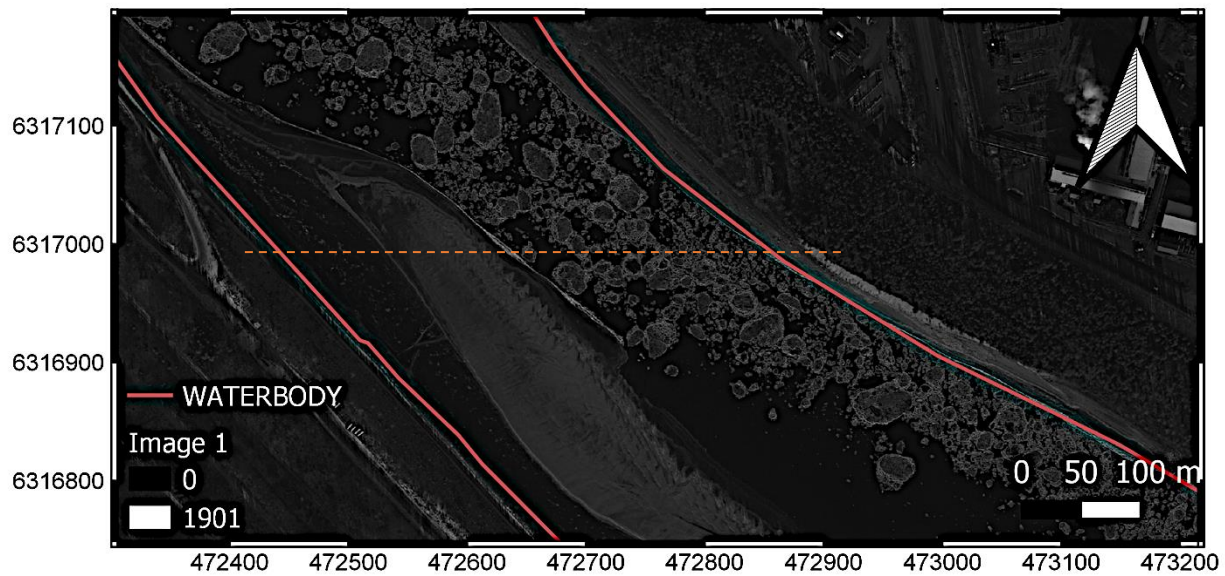


Figure 4.24 Satellite image for cross-section 6: Y=6316997.5.

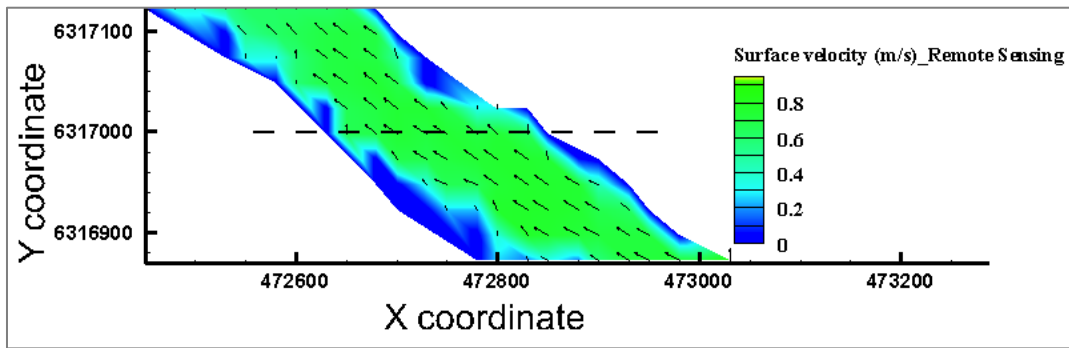


Figure 4.25 Velocity of the river obtained by remote sensing method (cross-section 6).

In this cross-section, on the left side of the river, when the water depth is small and the velocity is not significant, the riverbed has been filled with sediment. The existence of the deposit is visible in the images, and it reduces the channel width. This reduction in the width of the channel causes ice aggregation, and the entire length of this cross-section is filled with ice floes. This ice aggregation could cause a smaller velocity in ice floes than the model's velocity. However, the difference between the two velocities is not considerable due to the straight flow, except close to the boundary. The value of the RMSE in cross-section 6 is equal to 0.078, which shows that the results are reliable.

4.3.1.6 Cross-Section 7

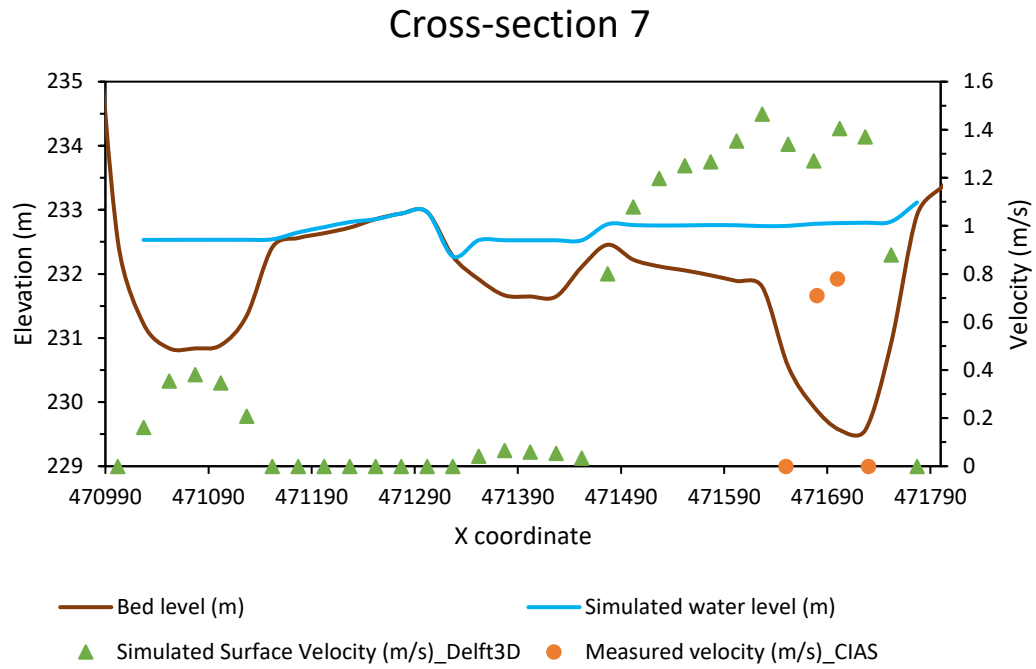


Figure 4.26 Simulated water level and comparison of simulated and measured surface water velocity in Cross-Section 7.

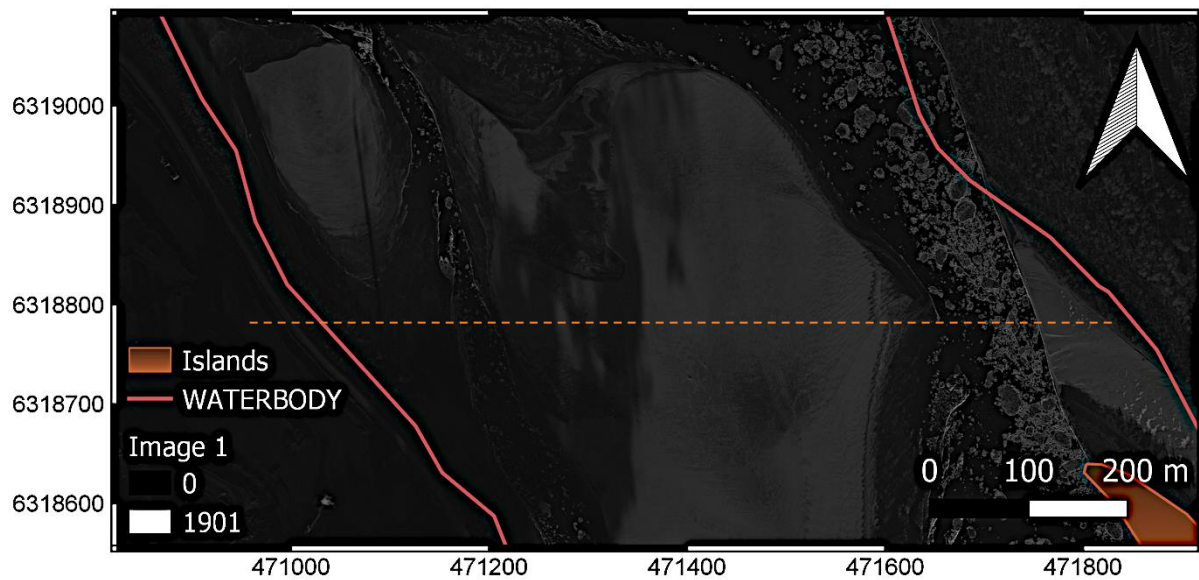


Figure 4.27 Satellite image for cross-section 7: Y=6318822.5.

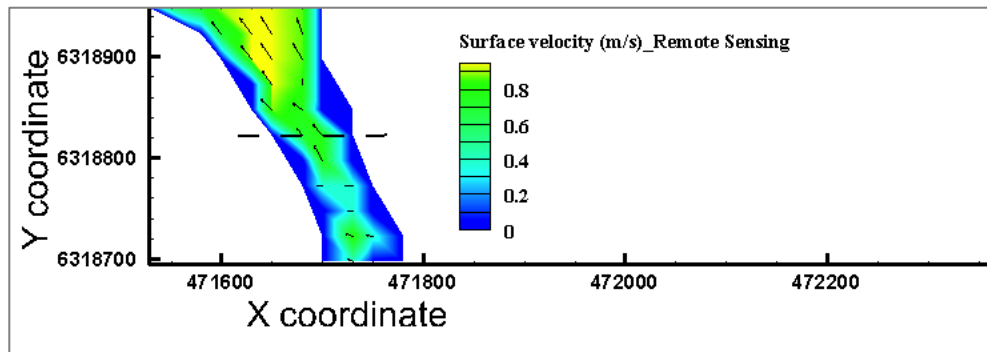


Figure 4.28 Velocity of the river obtained by remote sensing method (cross-section 7).

In this cross-section, due to the shallow water on the left side of the river, the river has no velocity. The flow is between $x=471652$ and $x=471726$, which is a narrow width (almost 100 m). In this narrow cross-section, four points could be used to measure the velocity. However, two of them have been eliminated because of a mismatch ($dy < 0$). It is due to the rotation or different velocities in ice floes, which confuse the BMA, and the remaining points show smaller values for velocity. The value of the RMSE in cross-section 7 is equal to 0.59, which shows that the results are not reliable. The reason could be ice aggregation in this cross-section (due to the narrow channel width).

4.3.1.7 Cross-Section 8

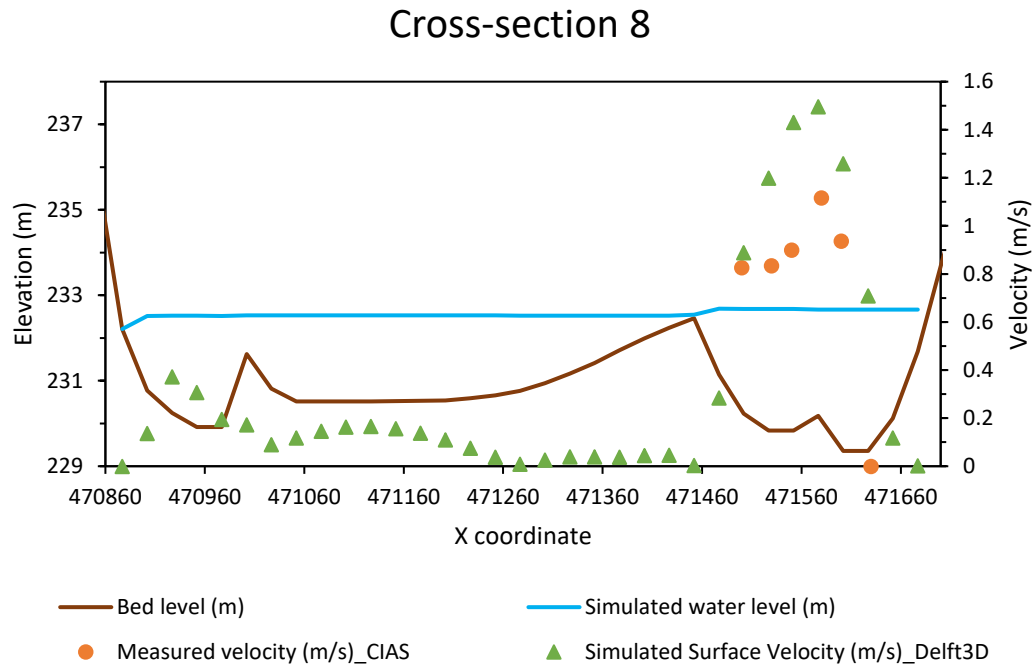


Figure 4.29 Simulated water level and comparison of simulated and measured surface water velocity in Cross-Section 8.

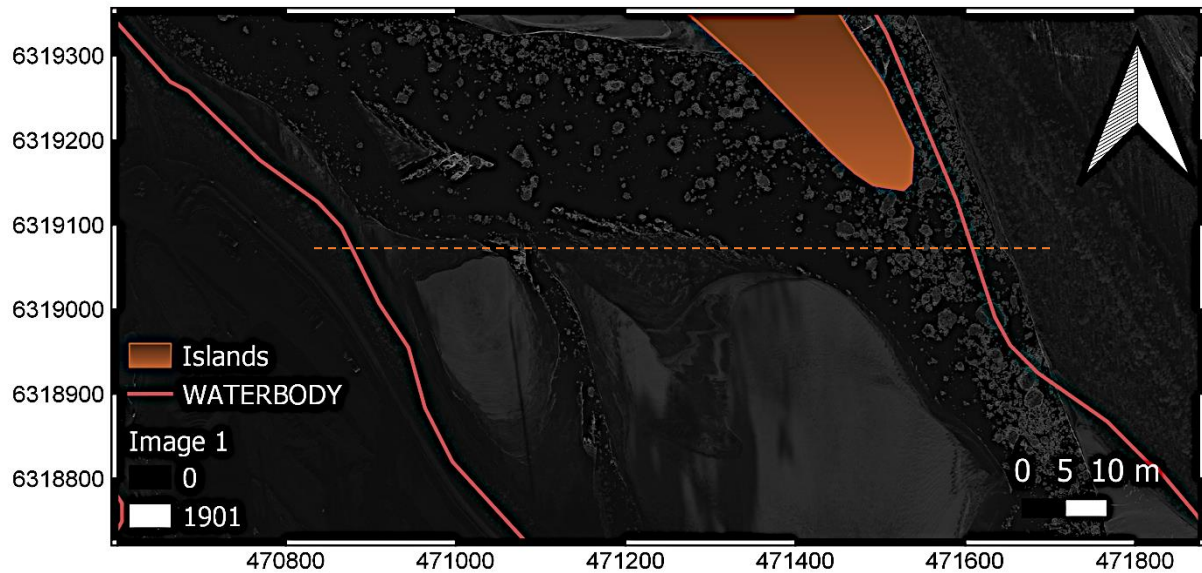


Figure 4.30 Satellite image for cross-section 8: Y=6319072.5.

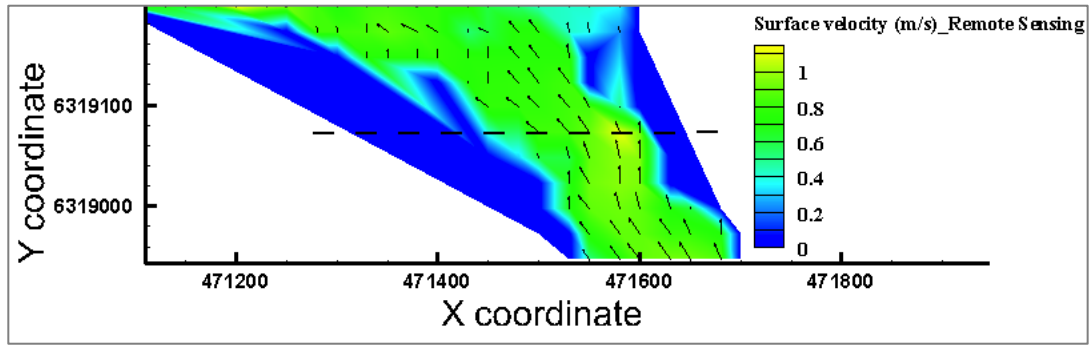


Figure 4.31 Velocity of the river obtained by remote sensing method (cross-section 8).

In this cross-section, there is a dry surface with no velocity on the left side of the river due to the shallow water and small magnitude of the velocity. A narrow section on the left side shows considerable velocity, but it is not detectable by the CIAS because of the very small ice floes.

In the main part of the cross-section (from $x=471327$ to 471652), on the left side, the ice floes do not exist, and they are accumulated on the right side of the cross-section. The reason for this accumulation on the right side can be found in the previous cross-sections of the river (4.3.1.6). Where $y=6318822.5$ (250 m before $y=6319072.5$), the river's width is equal to 100 m, and it has been gradually increased to almost 315 m in this cross-section (obtained from the images). The flow forced the ice floes to move on the right side close to the boundary.

Therefore, the velocities from $x=471327$ to $x=471477$ are not reliable. For the remaining points, the CIAS shows smaller values for velocity. The numerical model predicts some considerable velocities (greater than one m/s) on the right side. However, images show velocities less than one m/s. The value of the RMSE in cross-section 8 is equal to 0.36. The results can show us that in this cross-section the ice floes are moving with a velocity smaller than the flow.

4.3.1.8 Cross-Section 9

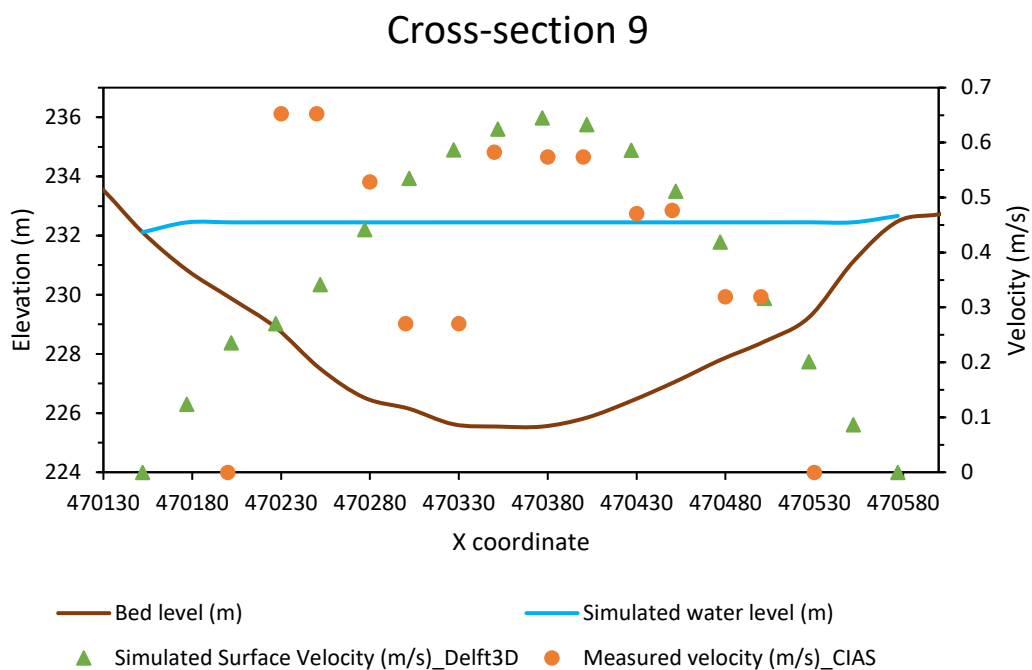


Figure 4.32 Simulated water level and comparison of simulated and measured surface water velocity in Cross-Section 9.

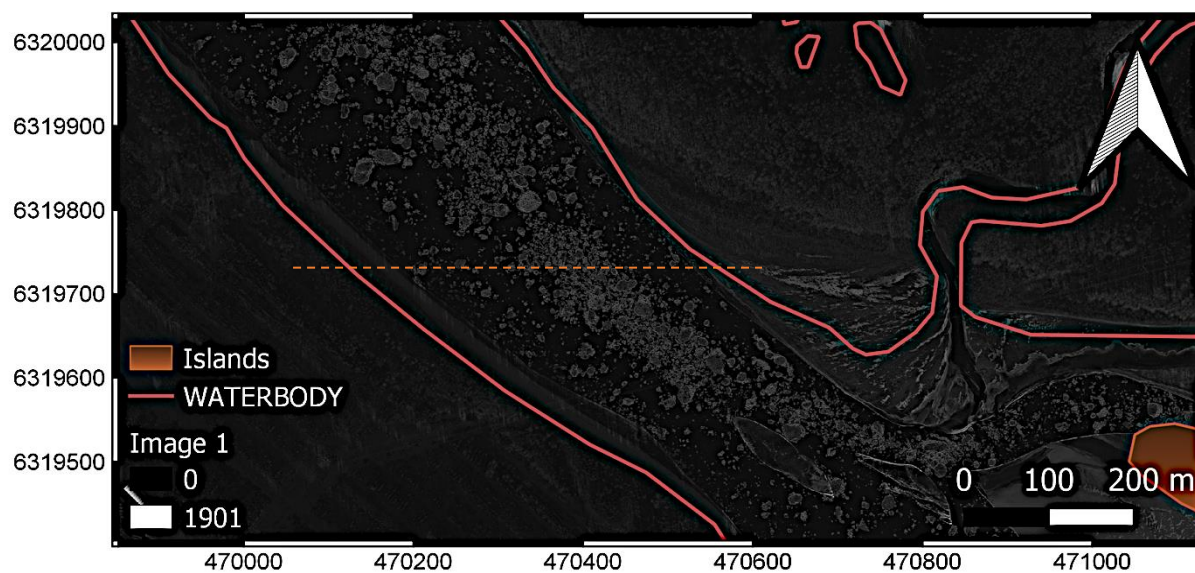


Figure 4.33 Satellite image for cross-section 9: Y=6319722.5.

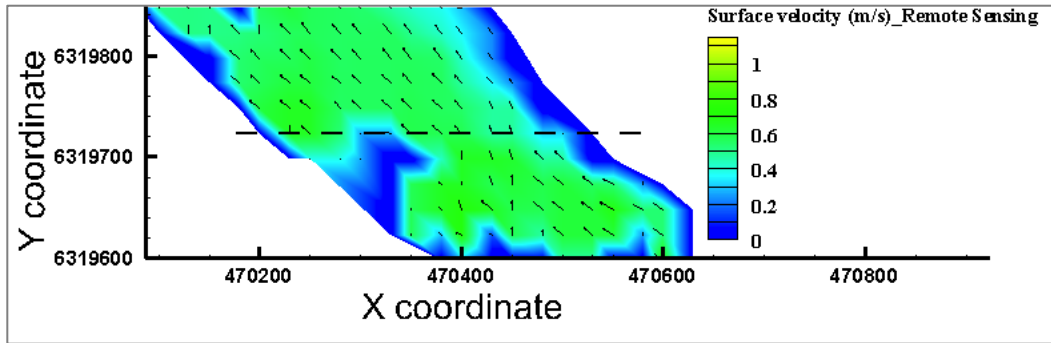


Figure 4.34 Velocity of the river obtained by remote sensing method (cross-section 9).

In this cross-section, most of the ice floes are in the middle of the river. However, due to the straight flow, the values of the two obtained velocities are close, and they agree well. The value of the RMSE in this part of the cross-section 9 is equal to 0.07.

On the left and right sides of the river, the number of ice floes is small, and the obtained velocities from the remote-sensing method could not be reliable. Also close to the boundary (on the left side), the velocities are misestimated, and the rest of the velocities have been replaced by zero by the applied median filter.

4.3.1.9 Cross-Section 10

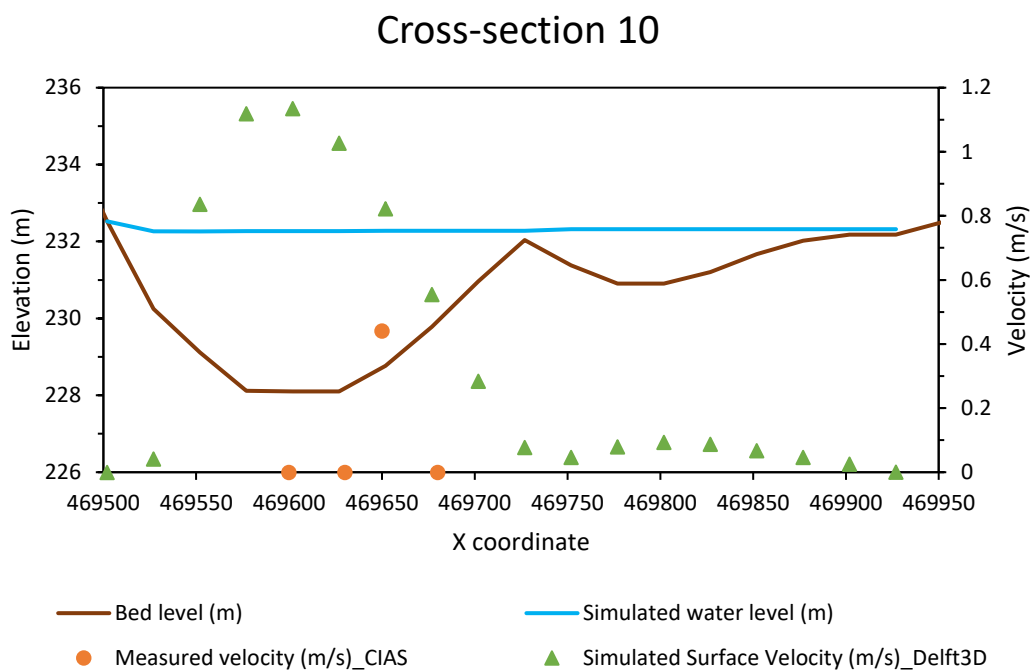


Figure 4.35 Simulated water level and comparison of simulated and measured surface water velocity in Cross-Section 10.

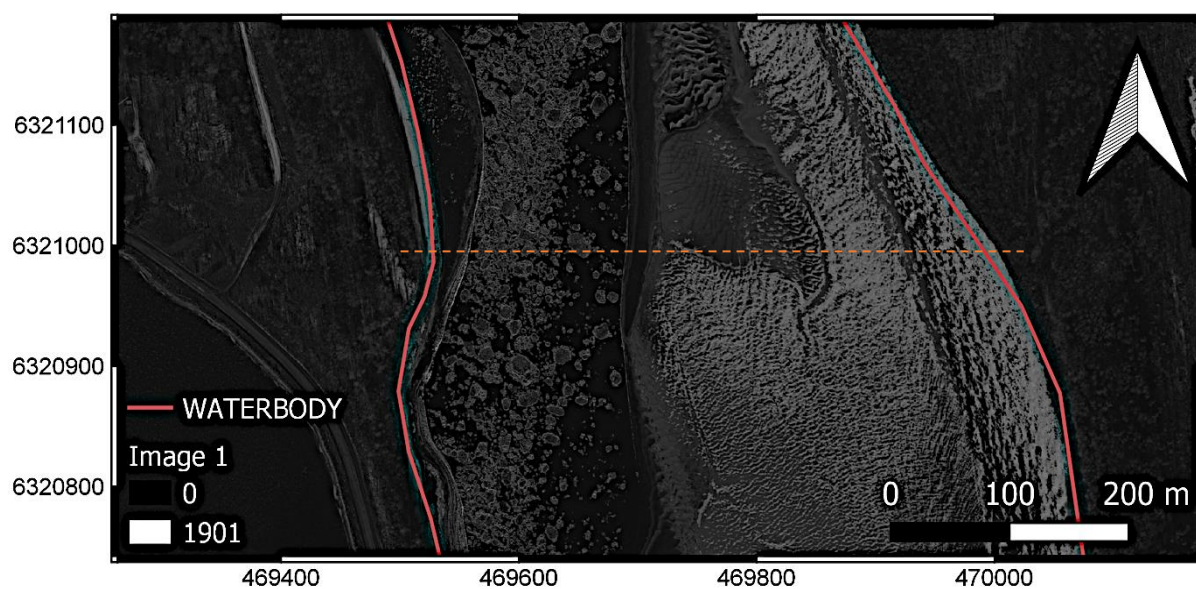


Figure 4.36 Satellite image for cross-section 10: Y=6320997.5.

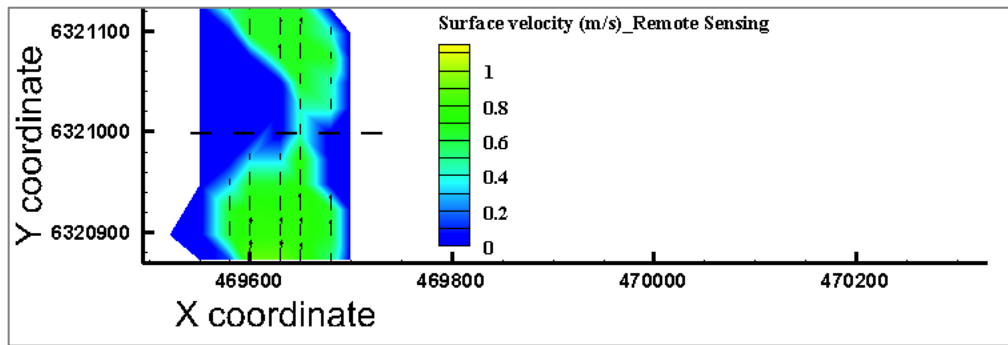


Figure 4.37 Velocity of the river obtained by remote sensing method (cross-section 10).

In this cross-section, flow experiences a reduction in the channel width (the channel width is equal to 130 m based on images); therefore, velocity in the model is greater than one (1m/s) in the middle of the section. The model estimates velocities for the points neighbouring the boundaries, but the CIAS cannot detect this movement. The images show ice aggregation in the middle of the river, and it makes the ice floes move slowly, and detecting the ice floes is mistakable. (Some points have been eliminated ($dy < 0$). The remaining points do not match the numerical model well and are unreliable.)

4.3.1.10 Cross-Section 11

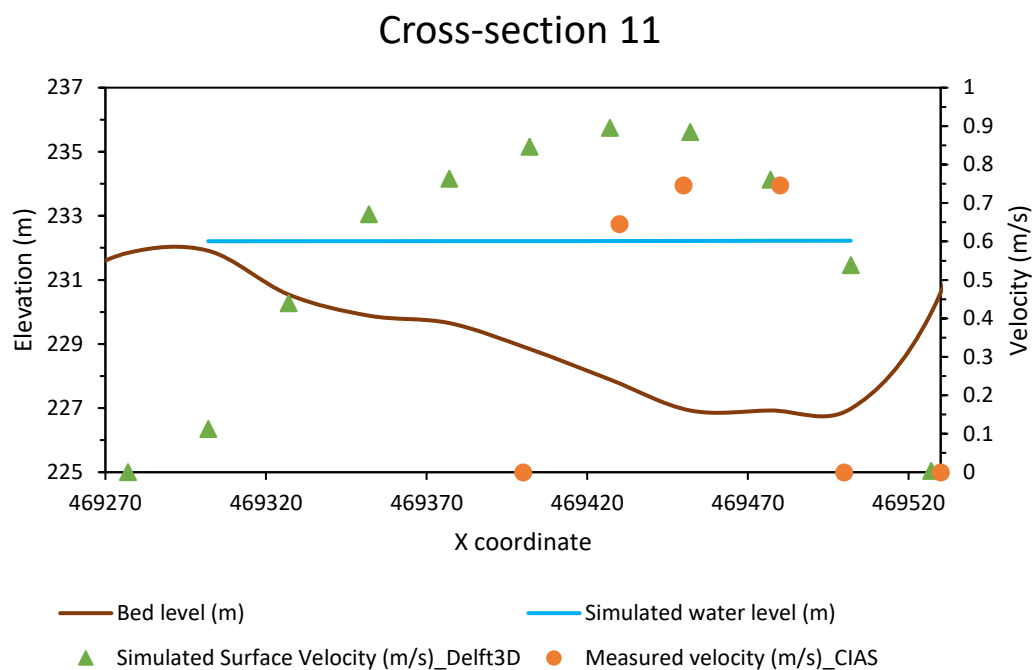


Figure 4.38 Simulated water level and comparison of simulated and measured surface water velocity in Cross-Section 11.

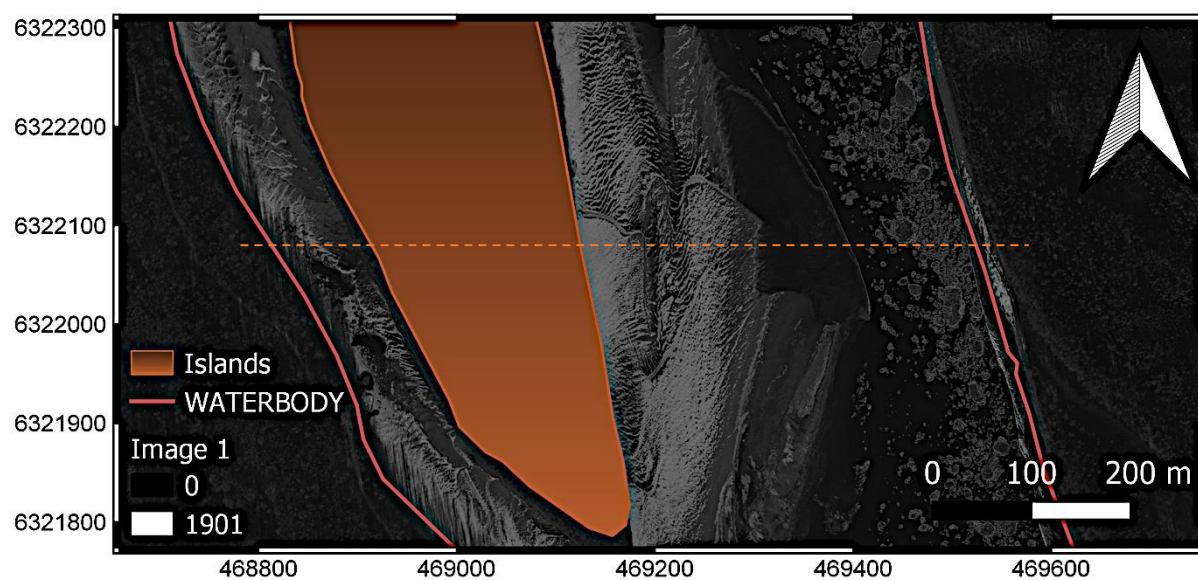


Figure 4.39 Satellite image for cross-section 11: Y=6322097.5.

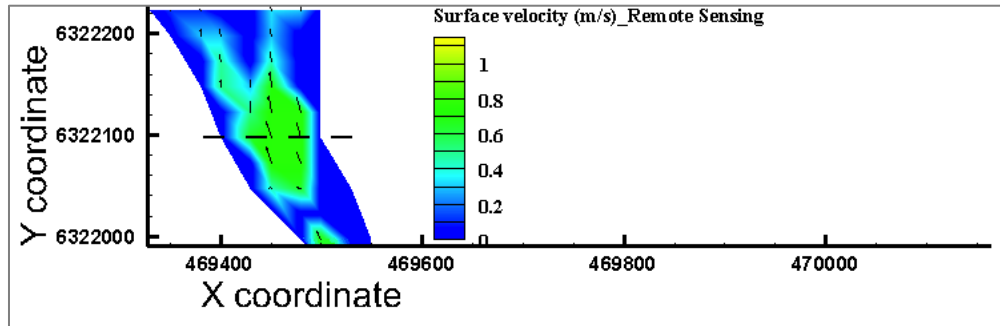


Figure 4.40 Velocity of the river obtained by remote sensing method (cross-section 11).

In this cross-section, the left side of the river is dry, and the water flows from $x=469400$. The river's width is almost 115 m, and the rest is dry. In the remaining part of the river, the CIAS shows smaller velocities for ice floes. That could be the result of ice aggregation. The ice floes in this cross-section are very small, and many exist here. This also forces them to collide with each other and rotate. The value of the RMSE in cross-section 11 is equal to 0.165.

4.3.1.11 Cross-Section 12

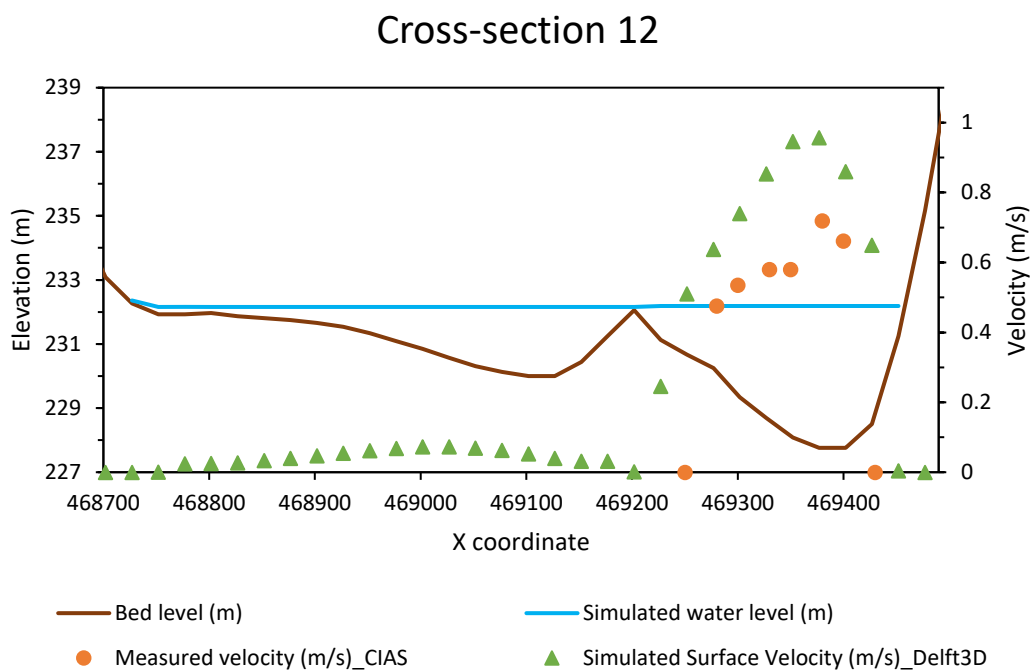


Figure 4.41 Simulated water level and comparison of simulated and measured surface water velocity in Cross-Section 12.

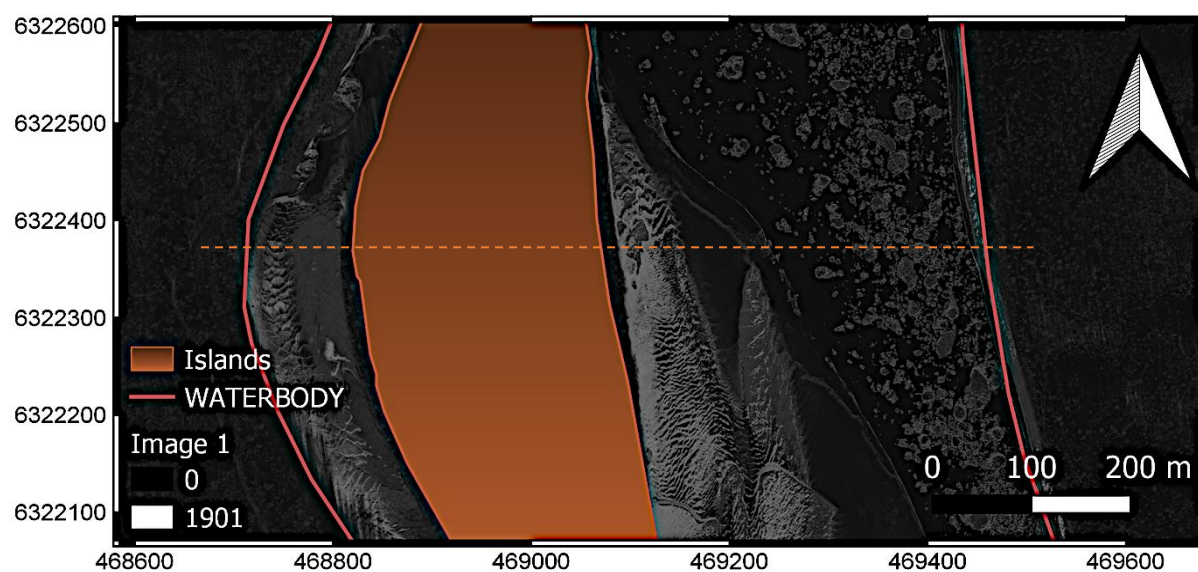


Figure 4.42 Satellite image for cross-section 12: Y=6322372.5.

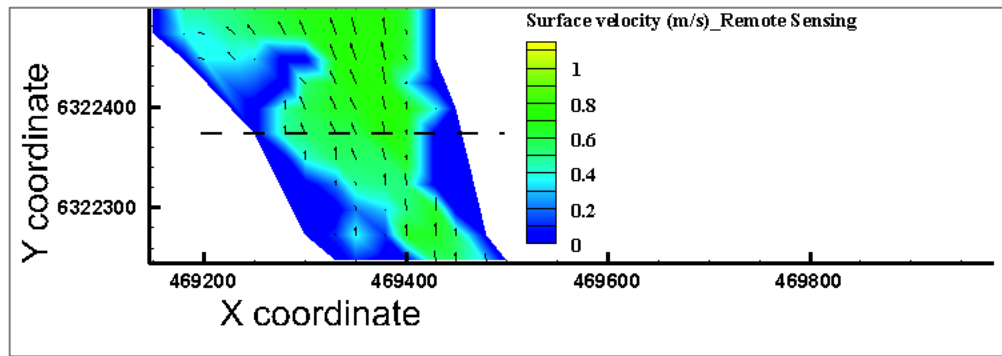


Figure 4.43 Velocity of the river obtained by remote sensing method (cross-section 12).

In this cross-section, the left side has no velocity and is dry. On the right side, due to the small width of the river (200 m), the numerical model estimates velocities close to 1 m/s. However, the images show smaller velocities resulting from ice aggregation and small ice floes. The value of the RMSE in cross-section 12 is equal to 0.25. However, it does not seem to be a good value for the RMSE, but they follow the same trend with R^2 equal to 0.67.

4.4 Conclusion

Athabasca river already has a complex geometry. In this study, the situation is more complicated due to the lower water level than at other times of the year and the existence of ice floes. The shallow water with a small magnitude of velocity causes the sediment to settle, and also, the freezing areas lead to numbers of small or big dry surfaces on the river.

By investigating different cross-sections along the river (with or without the existence of these dry surfaces), it seems that when the ice floes are not moving freely and there is a restriction in their movement, for instance, when they are accumulated in a cross-section, which happens mainly in a narrow cross-section with an expected velocity greater than one m/s (estimated by DELFT3D), since this situation increases the chance of rotation and collision of ice floes, the ability of the remote sensing method to detect the ice floes will be reduced (the results show discrepancy) and it cannot be reliable (not a good representative of water surface velocity). Also, when the ice floes are very small, and again, the chance of aggregation and rotation is high, it makes confusion for the algorithm to detect the ice floes. The remaining acceptable values for the velocity show smaller ice floe velocities in those cross-sections due to the ice aggregation. This aggregation will cause the ice floes to move slowly, and at some points, a collision between ice happens, which could be a reason for rotation and creates confusion for BMA.

CHAPTER 5 CONCLUSION AND RECOMMENDATIONS

5.1 Conclusion

An ice floe is a floating ice sheet, and most of the river's surface in the cold season can be covered by hundreds of ice floes. The ice floes can cause floods during ice break-up season, damaging the infrastructures while they are moving. However, we can benefit from them to estimate the river's surface velocity, by considering the hypothesis of equal ice floes velocity with water surface velocity, when other measurement methods are dangerous or difficult.

In this study, we focused on using satellite images as a source to detect the ice floes to obtain their movement. The images have been obtained from Maxar Company which can provide stereo (near-simultaneous) images with 0.5 m resolution on 11 November 2009. These images have been chosen due to their high quality, availability, and visible ice floes (there is a small chance to find proper images at that time of the year). Afterward, image pre-processing methods were applied to the images to prepare them for further studies. Then, the Block Matching Algorithm and the CIAS software were used to detect ice floes in two near-simultaneous images taken from the same position (Georeferenced). By dividing the movement to the time lag between two images (56 s), we obtained the velocities of the ice floes as a representative of the surface velocity of the river. A simple directional filter has eliminated the errors and the mismatches, and the remaining errors have been smoothed by applying the median filter.

The field measurement is impossible in this cold situation and with the existence of ice floes, we needed another source to compare these velocities. Hence, we used a numerical model as a source to compare the velocities. The other objective of this study was to develop an integrated numerical model to simulate the behaviour of the Lower Athabasca River on the same day that we studied the river with images (11 November 2009) as a source to study the velocity of the flow in winter situations. We used previously prepared bathymetry data, the measured hydrometric data (flow and water level) as boundary conditions, and the physical characteristics of the river to simulate the water level and the velocity of the river. The hydrodynamic model has been validated by the field measured water level and depth-averaged velocity in different cross-sections in an ice-free situation, and it shows well agreement. However, it has to be mentioned that, since there is no available measured data on the simulation day (11 November 2009), we have been forced to evaluate the model's functionality on a day that there is in-situ measured data (15 and 16 September

2004), which may add some level of uncertainty to the model. The reason for this lack of reliable measured data in November 2009, could be the existence of ice floes on the surface of the river, which has made the in-situ measurements impossible.

There are some limitations and uncertainties in the numerical model: the highest resolution of the available bathymetry data was equal to 10 m at some points which can cause missing some specific elevations. However, it is worth mentioning that this resolution can be considered a high-resolution value in the study of the Earth's elevation. Another reason could be using a constant value for the manning coefficient. This value differs at different times and locations and changes in water level changes this value. Also, the effect of ice floes is not considered in the numerical model. These simplifications that we applied to the model, they add uncertainties to the model.

Finally, we compared our obtained velocities (obtained by different methods) to evaluate the functionality of the remote-sensing in velocity measurement using ice floes to represent the river's velocity in different conditions (e.g., narrow/wide width, great/small velocity, braided/ straight geology, etc.). As mentioned earlier, when the river is straight and the ice floes can move easily without any restriction, they show good agreement (ice floes are good representatives of water surface velocity). However, in other conditions (e.g., narrow channel width, a considerable amount of very small ice floes, bending in the river, or ice aggregation) which make restrictions on the movement of ice floes, the remotely-sensed values are unreliable (not a good representative of water surface velocity).

5.2 Discussion

Detecting the ice floes to estimate the river velocity in cold seasons by processing satellite images could be a replacement for other available methods. However, obtaining proper and near-simultaneous images on a specific date and time is a considerable challenge. In addition, since the technique is very sensitive to the quality of the images and the behaviour of the river, we cannot rely on this method in some conditions, for instance, when the movement of ice floes is restricted by ice aggregation. On the other hand, the correct matches represent the true and real ice movement on the river's surface and prevent time and energy-consuming calculations when there is no restriction on the movement of ice floes. However, numerical modelling needs more information to simulate the velocity and water level, and it cannot consider the real and on-time situation of the river very precisely, and we considered some hypotheses to simplify the model.

5.3 Future work

In this study, for the first time, the two following objectives have been gained:

- 1) We assessed the reliability of velocity estimation using motion tracking of ice.
- 2) We provide a continuous velocity field on the Lower Athabasca River.

The obtained objectives could be used for various purposes, including the validation of numerical models or combining with other models to estimate new components (e.g., sediment or oil transportation in the river).

However, we ignored the existence of sediments to simplify the simulation. Due to the small velocity values and shallow water level, sediment deposition plays an essential role in the river's behaviour. Also, the ice floes could be added to the numerical model to complicate the condition for investigating the effect of ice floes and evaluating the functionality of using DELFT3D to simulate ice floes' movement compared to their real movement, which is obtained from the images. It is worth mentioning that the proposed subjects need more information and data on the sediment transportation system of the Lower Athabasca River, the characteristics of the sediment, and the characteristics of ice floes (e.g., thickness, density, porosity, shape, and other related factors). Also, it is possible to add more complexities like the variable manning coefficients for each section.

For the remote sensing part of this study, it is suggested to request high-quality images from companies that can provide high-resolution images like Maxar or Planet constellations. We can also use the same strategy on the ice break-up event (instead of ice freeze-up) to estimate the ice floes' velocity, channel width, and water depth to measure the discharge and compare it with the numerical model or in-situ measurements at that time to study the potential of the flood. Meanwhile, we are able to detect the changes in the channel width of the river in the images to investigate the advance of water and ice floes from the river into the flood plain.

REFERENCES

1. Bonsal, B.R. and T.D. Prowse, *Trends and Variability in Spring and Autumn 0 °C-Isotherm Dates over Canada*. Climatic Change, 2003. **57**(3): p. 341-358.
2. ClimateAtlasofCanada. Available from: https://climateatlas.ca/map/canada/icedays_baseline#z=6&lat=56.16&lng=-109.2&city=437.
3. PEACE RIVER. Available from: <https://peaceriver.ca/river-ice/>.
4. *River Ice Mapping and Monitoring using SAR Satellites*. 2015-11-25; Available from: <https://www.nrcan.gc.ca/earth-sciences/permafrost-ice-snow/lake-river-ice/9166>.
5. *Ice Jams: frazil ice, freeze up, and floods*. 2017; Available from: <https://albertawater.com/ice-jams>.
6. Prowse, T.D. and S. Beltaos, *Climatic control of river-ice hydrology: a review*. Hydrological Processes, 2002. **16**(4): p. 805-822.
7. Beltaos, S., *River ice breakup*. 2008, Highlands Ranch, CO: Water Resources Publications, LLC.
8. Beltaos, S. *Assessing ice-jam flood risk: methodology and limitations*. in *Proceedings of the 20th IAHR International Symposium on Ice, Lathi, Finland*. 2010.
9. Beltaos, S., *River ice breakup processes: recent advances and future directions*. Canadian Journal of Civil Engineering, 2007. **34**(6): p. 703-716.
10. Whitfield, P.H., *Floods in future climates: a review Changing floods in future climates*. Journal of Flood Risk Management, 2012. **5**(4): p. 336-365.
11. Peters, D.L., et al., *Flood hydrology of the Peace-Athabasca Delta, northern Canada*. Hydrological processes., 2006. **20**(19): p. 4073-4096.
12. Beltaos, S., *Ice-jam flood regime of the Peace-Athabasca Delta: Update in light of the 2014 event*. Cold Regions Science and Technology, 2019. **165**.
13. Goulding, H.L., T.D. Prowse, and S. Beltaos, *Spatial and temporal patterns of break-up and ice-jam flooding in the Mackenzie Delta, NWT*. Hydrological Processes, 2009. **23**: p. 2654-2670.
14. Huang, K., et al., *A photogrammetry-based variational optimization method for river surface velocity measurement*. Journal of Hydrology, 2021.
15. Kääb, A. and T. Prowse, *Cold-regions river flow observed from space*. Geophysical Research Letters, 2011. **38**(8).
16. Carroll, M., et al., *Quantifying Surface Water Dynamics at 30 Meter Spatial Resolution in the North American High Northern Latitudes 1991–2011*. Remote Sensing, 2016. **8**(8): p. 622.
17. Huhta, C., *Handheld Acoustic Doppler Velocimeter (ADV) for Water Velocity Surveys*, in *Hydraulic Measurements and Experimental Methods 2002*. 2002. p. 1-10.
18. Shiklomanov, A.I., R.B. Lammers, and C.J. Vörösmarty, *Widespread decline in hydrological monitoring threatens Pan-Arctic Research*. Eos, Transactions American Geophysical Union, 2002. **83**(2): p. 13-17.
19. Jowett, I.G. and M.J. Duncan, *Effectiveness of 1D and 2D hydraulic models for instream habitat analysis in a braided river*. Ecological Engineering, 2012. **48**: p. 92-100.
20. Birkett, C.M., et al., *Surface water dynamics in the Amazon Basin: Application of satellite radar altimetry*. Journal of Geophysical Research: Atmospheres, 2002. **107**(D20): p. 26-1.

21. Brakenridge, G.R., et al., *Orbital microwave measurement of river discharge and ice status*. Water Resources Research, 2007. **43**(4).
22. Alsdorf, D., D. Lettenmaier, and C. Vörösmarty, *The need for global, satellite-based observations of terrestrial surface waters*. Eos, Transactions American Geophysical Union, 2003. **84**(29): p. 269-276.
23. Kääb, A., M. Lamare, and M. Abrams, *River ice flux and water velocities along a 600 km-long reach of Lena River, Siberia, from satellite stereo*. Hydrology and Earth System Sciences, 2013. **17**(11): p. 4671-4683.
24. Prowse, T.D., *TECHNICAL PAPERS - River-Ice Ecology: I: Hydrologic, Geomorphic, and Water-Quality Aspects*. Journal of cold regions engineering., 2001. **15**(1): p. 1.
25. Shaw, J.a.K., R., *The composition of recent alluvial gravels in Alberta River beds; Alberta Research Council*. . 1982, ARC/AGS Bulletin 41.
26. Doyle, P.F., *Hydrologic and hydraulic characteristics of the Athabasca River from Fort McMurray to Embarras*. . 1977, Alberta Energy Regulator. p. 51.
27. Conly, F., R. Crosley, and J. Headley, *Characterizing sediment sources and natural hydrocarbon inputs in the lower Athabasca River, Canada*. Journal of Environmental Engineering and Science, 2002. **1**: p. 187-199.
28. Canada, C.A.o.; Available from: https://climateatlas.ca/map/canada/nov_meantemp_baseline#z=6&lat=56.16&lng=-109.2&city=437.
29. Wayland, M., *Mackenzie River Basin: State of the Aquatic Ecosystem Report, 2003*. 2004: [Fort Smith, NWT]: Mackenzie River Basin Board.
30. Science), S.M.W.S.C.a., *Athabasca Watershed*. 2022.
31. Luijendijk, A.P., *Validation, calibration and evaluation of Delft3D-FLOW model with ferry measurements*. 2001, TU Delft, Faculty of Civil Engineering and Geosciences, Hydraulic Engineering.
32. Aberle, J., et al., *Experimental hydraulics : methods, instrumentation, data processing and management. Volume II, Instrumentation and measurement techniques*. 2017, CRC Press/Balkema: Leiden, the Netherlands.
33. Jodeau, M., et al., *Application and evaluation of LS-PIV technique for the monitoring of river surface velocities in high flow conditions*. Flow Measurement and Instrumentation, 2008. **19**(2): p. 117-127.
34. Bennett, K.E. and T.D. Prowse, *Northern Hemisphere geography of ice-covered rivers. Hydrological processes.*, 2010. **24**(2): p. 235-240.
35. Shakibaeinia, A., et al., *A numerical framework for modelling sediment and chemical constituents transport in the Lower Athabasca River*. Journal of Soils and Sediments, 2017. **17**(4): p. 1140-1159.
36. Lu, J.-Y., et al., *Application of a portable measuring system with acoustic Doppler current profiler to discharge observations in steep rivers*. Flow Measurement and Instrumentation, 2006. **17**(3): p. 179-192.
37. Weitbrecht, V., G. Kühn, and G.H. Jirka, *Large scale PIV-measurements at the surface of shallow water flows*. Flow Measurement and Instrumentation, 2002. **13**(5): p. 237-245.
38. Admiraal, D.M., J.S. Stansbury, and C.J. Haberman, *Case Study: Particle Velocimetry in a Model of Lake Ogallala*. Journal of Hydraulic Engineering, 2004. **130**(7): p. 599-607.
39. Creutin, J.D., et al., *River gauging using PIV techniques: a proof of concept experiment on the Iowa River*. Journal of Hydrology, 2003. **277**(3): p. 182-194.

40. Jasek, M., M. Muste, and R. Ettema, *Estimation of Yukon River discharge during an ice jam near Dawson City*. Canadian Journal of Civil Engineering, 2001. **28**(5): p. 856-864.
41. Lucchitta, B.K. and H.M. Ferguson, *Antarctica: Measuring Glacier Velocity from Satellite Images*. Science, 1986. **234**(4780): p. 1105-1108.
42. Bindenschadler, R.A. and T.A. Scambos, *Satellite-Image-Derived Velocity Field of an Antarctic Ice Stream*. Science, 1991. **252**(5003): p. 242-246.
43. Scambos, T.A., et al., *Application of image cross-correlation to the measurement of glacier velocity using satellite image data*. Remote Sensing of Environment, 1992. **42**(3): p. 177-186.
44. Heid, T. and A. Kääb, *Evaluation of existing image matching methods for deriving glacier surface displacements globally from optical satellite imagery*. Remote Sensing of Environment, 2012. **118**: p. 339-355.
45. Kääb, A., *Monitoring high-mountain terrain deformation from repeated air- and spaceborne optical data: examples using digital aerial imagery and ASTER data*. ISPRS Journal of Photogrammetry and Remote Sensing, 2002. **57**(1): p. 39-52.
46. Rolstad, C., et al., *Visible and near-infrared digital images for determination of ice velocities and surface elevation during a surge on Osbornebreen, a tidewater glacier in Svalbard*. Annals of Glaciology, 1997. **24**: p. 255-261.
47. Kääb, A., B. Altena, and J. Mascaro, *River-ice and water velocities using the Planet optical cubesat constellation*. Hydrology and Earth System Sciences, 2019. **23**(10): p. 4233-4247.
48. Budillon, A., V. Pascazio, and G. Schirinzi, *Estimation of radial velocity of moving targets by along-track interferometric SAR systems*. IEEE Geoscience and Remote Sensing Letters, 2008. **5**(3): p. 349-353.
49. Goldstein, R.M. and H.A. Zebker, *Interferometric radar measurement of ocean surface currents*. Nature, 1987. **328**(6132): p. 707-709.
50. Romeiser, R., et al., *Current measurements by SAR along-track interferometry from a Space Shuttle*. IEEE Transactions on Geoscience and Remote Sensing, 2005. **43**(10).
51. Romeiser, R., et al., *Current Measurements in Rivers by Spaceborne Along-Track InSAR*. IEEE Transactions on Geoscience and Remote Sensing, 2007. **45**(12).
52. Bjerklie, D.M., et al., *Evaluating the potential for measuring river discharge from space*. Journal of Hydrology, 2003. **278**(1): p. 17-38.
53. Bjerklie, D.M., et al., *Estimating discharge in rivers using remotely sensed hydraulic information*. Journal of Hydrology, 2005. **309**(1): p. 191-209.
54. Goldstein, R.M., T.P. Barnett, and H.A. Zebker, *Remote Sensing of Ocean Currents*. Science, 1989. **246**(4935): p. 1282-1285.
55. Unterschultz, K.D., J. van der Sanden, and F.E. Hicks, *Potential of RADARSAT-1 for the monitoring of river ice: Results of a case study on the Athabasca River at Fort McMurray, Canada*. Cold Regions Science and Technology, 2009. **55**(2): p. 238-248.
56. Vincent, F., et al., *Detection of river/sea ice deformation using satellite interferometry: limits and potential*. International Journal of Remote Sensing, 2004. **25**(18): p. 3555-3571.
57. Obenade, M., et al., *Application of remote sensing and GIS in flood vulnerability and risk assessment : a case study of Yenagoa and its environs, Bayelsa State*. Proceedings of the 2nd International Conference on Flood and Erosion Prevention, Protection and Mitigation, November 3-5, 2014, @ Rivers State University of Science and Technology, Port Harcourt, Nigeria., 2014.

58. Pavelsky, T.M. and L.C. Smith, *Remote sensing of suspended sediment concentration, flow velocity, and lake recharge in the Peace-Athabasca Delta, Canada*. Water Resources Research, 2009. **45**(11).
59. Lavergne, T., et al., *Sea ice motion from low-resolution satellite sensors: An alternative method and its validation in the Arctic*. Journal of Geophysical Research: Oceans, 2010. **115**(C10).
60. Matthews, J., *Stereo observation of lakes and coastal zones using ASTER imagery*. Remote Sensing of Environment, 2005. **99**(1): p. 16-30.
61. *Image correlation software CIAS*. 2013 June 23, 2020; Available from: <https://www.mn.uio.no/geo/english/research/projects/icemass/cias/>.
62. Kääb, A. and M. Vollmer, *Surface Geometry, Thickness Changes and Flow Fields on Creeping Mountain Permafrost: Automatic Extraction by Digital Image Analysis*. Permafrost and Periglacial Processes, 2000. **11**(4): p. 315-326.
63. Kääb, A. and S. Leprince, *Motion detection using near-simultaneous satellite acquisitions*. Remote Sensing of Environment, 2014. **154**: p. 164-179.
64. Beltaos, S. and A. Kääb, *Estimating river discharge during ice breakup from near-simultaneous satellite imagery*. Cold Regions Science and Technology, 2014. **98**: p. 35-46.
65. Bjerklie, D.M., et al., *Satellite remote sensing estimation of river discharge: Application to the Yukon River Alaska*. Journal of Hydrology, 2018. **561**: p. 1000-1018.
66. Engineers, U.A.C.o. *HEC-RAS*. Available from: <https://www.hec.usace.army.mil/software/hec-ras/>.
67. DHI. *MIKE 11*. Available from: <https://www.mikepoweredbydhi.com/products/mike-11>.
68. Dibike, Y., et al., *Effects of projected climate on the hydrodynamic and sediment transport regime of the lower Athabasca River in Alberta, Canada*. River Research and Applications, 2018. **34**(5): p. 417-429.
69. DHI. *MIKE 21*. Available from: <https://www.dhigroup.com/download/mike-2020/mike-21>.
70. Chatterjee, C., S. Förster, and A. Bronstert, *Comparison of hydrodynamic models of different complexities to model floods with emergency storage areas*. Hydrological Processes, 2008. **22**(24): p. 4695-4709.
71. Rinaldi, M., et al., *Numerical simulation of hydrodynamics and bank erosion in a river bend*. Water Resources Research, 2008. **44**(9).
72. Hicks, D.M., et al., *Use of Remote-Sensing with Two-Dimensional Hydrodynamic Models to Assess Impacts of Hydro-Operations on a Large, Braided, Gravel-Bed River: Waitaki River, New Zealand*, in *Braided Rivers*. 2006. p. 311-326.
73. Deltares. *Delft3D 4 - Open Source Community*. Available from: <https://oss.deltares.nl/web/delft3d>.
74. Javernick, L., et al., *Numerical Modelling of Braided Rivers with Structure-from-Motion-Derived Terrain Models*. River Research and Applications, 2016. **32**(5): p. 1071-1081.
75. Parsapour-moghaddam, P., C.D. Rennie, and J. Slaney, *Hydrodynamic Simulation of an Irregularly Meandering Gravel-Bed River: Comparison of MIKE 21 FM and Delft3D Flow models*. E3S Web of Conferences, 2018. **40**.
76. Kasvi, E., et al., *Two-dimensional and three-dimensional computational models in hydrodynamic and morphodynamic reconstructions of a river bend: sensitivity and functionality*. Hydrological Processes, 2015. **29**(6): p. 1604-1629.
77. Parsapour-Moghaddam, P., et al., *Impacts of Channel Morphodynamics on Fish Habitat Utilization*. Environmental Management, 2019. **64**(3): p. 272-286.

78. Maryam, R. *A comparison between the suspended sediment concentrations derived from DELFT3D model and collected using transmissometer - a case study in tidally dominated area of Dithmarschen Bight*. Oceanologia. **57**, 44-49 DOI: 10.1016/j.oceano.2014.06.002.
79. Lesser, G., et al., *Three-dimensional morphological modelling in Delft3D-FLOW*. Paper in prep, 2001.
80. Ramos, V., R. Carballo, and J.V. Ringwood, *Application of the actuator disc theory of Delft3D-FLOW to model far-field hydrodynamic impacts of tidal turbines*. Renewable Energy, 2019. **139**: p. 1320-1335.
81. Couceiro, M.A.A., C.A.F. Schettini, and E. Siegle, *Modeling an arrested salt-wedge estuary subjected to variable river flow*. Regional Studies in Marine Science, 2021. **47**.
82. Williams, R.D., et al., *Hydraulic validation of two-dimensional simulations of braided river flow with spatially continuous aDcp data*. Water Resources Research, 2013. **49**(9): p. 5183-5205.
83. Andrishak, R., et al. *Freeze-up study on the lower Athabasca River (Alberta, Canada)*. in *Proceedings of the 19. IAHR international symposium on ice: using new technology to understand water-ice interaction*. 2008.
84. Kashyap, S., et al., *Two-dimensional numerical modelling of sediment and chemical constituent transport within the lower reaches of the Athabasca River*. Environmental Science and Pollution Research, 2017. **24**(3): p. 2286-2303.
85. Dibike, Y.B., et al., *Modelling the potential effects of Oil-Sands tailings pond breach on the water and sediment quality of the Lower Athabasca River*. Science of the Total Environment, 2018. **642**: p. 1263-1281.
86. Gomez-Chova, L., et al., *Gridding artifacts on medium - resolution satellite image time series : MERIS case study*. IEEE transactions on geoscience and remote sensing, 2011. **49**(7): p. 2601-2611.
87. Goshtasby, A., *2-D and 3-D image registration for medical, remote sensing, and industrial applications*. 2005, John Wiley & Sons: Hoboken, N.J.
88. Unwin, D.J., *Selecting and using ground control points in image rectification and registration*. Geographical systems : the international journal of geographical information, analysis, theory and decision., 1999.
89. Rao, Y.R., *APPLICATION OF NORMALIZED CROSS CORRELATION TO IMAGE REGISTRATION*. International Journal of Research in Engineering and Technology, 2014. **03**(17): p. 12-16.
90. Shakibaeinia, A., et al., *An integrated numerical framework for water quality modelling in cold-region rivers: A case of the lower Athabasca River*. Science of the Total Environment, 2016. **569-570**: p. 634-646.
91. Hicks, F., *Personal communication* 2011.
92. CEMA. *Canadian Council of Ministers of the Environment, Lower Athabasca data*. 2012 [cited 2012 10 Nov]; Available from: http://ftp.cciw.ca/incoming/LowerAthabasca_data_.
93. Pietroniro, A.H., Faye; Andrishak, A; Watson, D; Boudreau, P; Kouwen, N, *Hydraulic routing of flows for the Mackenzie River*. 2011.
94. Deltares, D., *Delft3D-FLOW user manual* 2018.
95. Deltares. *QUICKIN user manual*. 2021; Available from: https://content.oss.deltares.nl/delft3d/manuals/QUICKIN_User_Manual.pdf.
96. She, Y. and F. Hicks, *Modeling ice jam release waves with consideration for ice effects*. Cold Regions Science and Technology, 2006. **45**(3): p. 137-147.

97. Beltaos, S., et al., *Erosion potential of dynamic ice breakup in Lower Athabasca River. Part I: Field measurements and initial quantification*. Cold Regions Science and Technology, 2018. **149**: p. 16-28.
98. Malverti, L., E. Lajeunesse, and F. Métivier, *Small is beautiful: Upscaling from microscale laminar to natural turbulent rivers*. Journal of Geophysical Research: Earth Surface, 2008. **113**(F4).
99. Le Coz, J., et al., *Performance of image-based velocimetry (LSPIV) applied to flash-flood discharge measurements in Mediterranean rivers*. Journal of Hydrology, 2010. **394**(1-2): p. 42-52.
100. Hauet, A., T. Morlot, and L.a. Daubagnan, *Velocity profile and depth-averaged to surface velocity in natural streams: A review over a large sample of rivers*. E3S Web of Conferences, 2018. **40**.
101. Yalin, M.S., *Mechanics of sediment transport*. 2e ed. ed. 1977, New York: Pergamon Press.
102. Krogstad, P.a., R.A. Antonia, and L.W.B. Browne, *Comparison between rough- and smooth-wall turbulent boundary layers*. Journal of Fluid Mechanics, 1992. **245**(-1): p. 599.
103. Kumari, S., S.K. Ghosh, and M.F. Buchroithner, *Measurement of glacier velocity at Pik Lenin, Tajikistan, by feature tracking*. The International Archives of the Photogrammetry, Remote Sensing and Spatial Information Sciences, 2014. **8**: p. 531-536.

APPENDIX A COMPARING DIFFERENT GEOREFERENCING METHODS

When a series of images are being studied, to detect or understand the differences between them (for instance, detecting an object), the images must be spatially aligned. The co-registration method gives this alignment to the images. There are different algorithms that can transfer a target image to a reference image. Here, a small stable object has been selected to be a benchmark to compare the location of this object after applying different co-registration methods to the target image. Figure A.1 shows the location of this benchmark point. The following images show the location of this object in the co-registered images compared to the reference image. The images on the right side show the location of this object in the target image after applying different co-registration methods. The images on the left side show the location of this object in the reference image. As much as this object is closer in the two images, the co-registration method is more functional. Figure 0.5 shows the smallest difference between the location of this object in the two images. This is an example of the results that already have been obtained earlier. The TPS method has the minimum value of the MRT and it is clear in the images that it does the co-registration better than other methods.

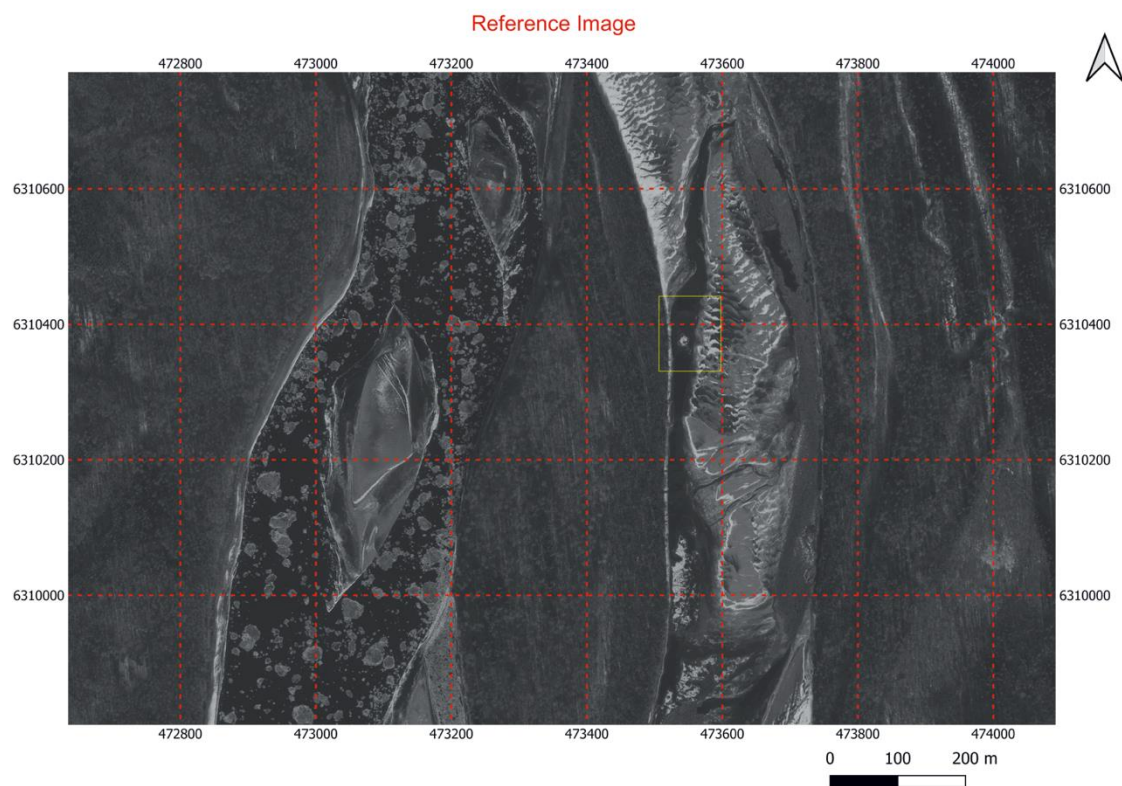


Figure A.1 Section of the Athabasca River in the reference image. The yellow rectangle shows the object which will be detected and compared after applying different co-registration methods on the target image with this reference image.

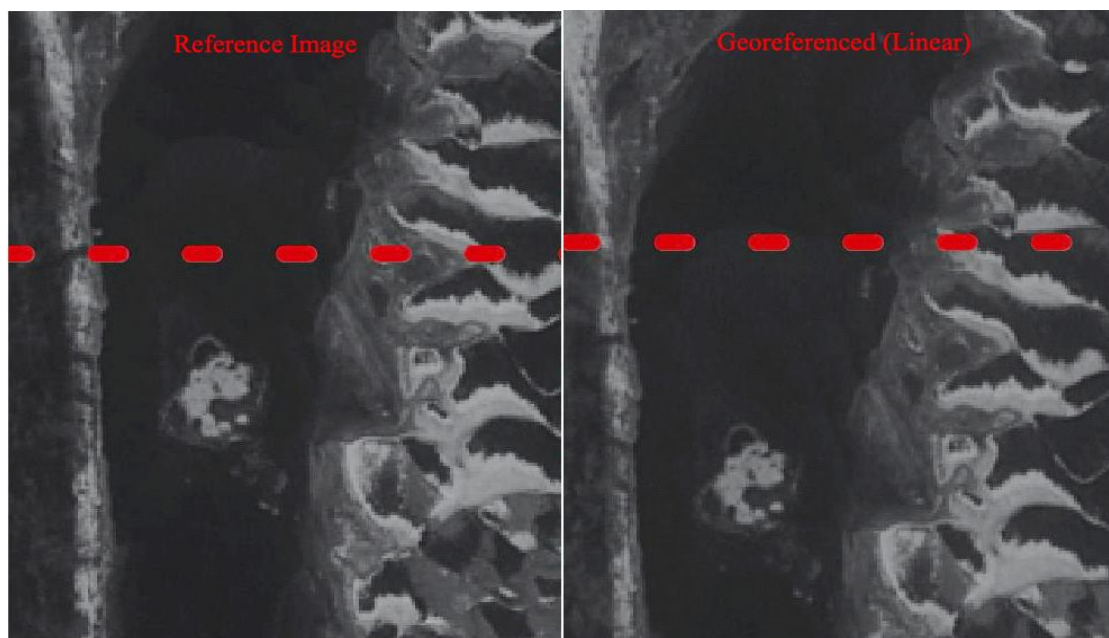


Figure A.2 Comparison between the Reference Image and Georeferenced image (co-registration method: Linear).

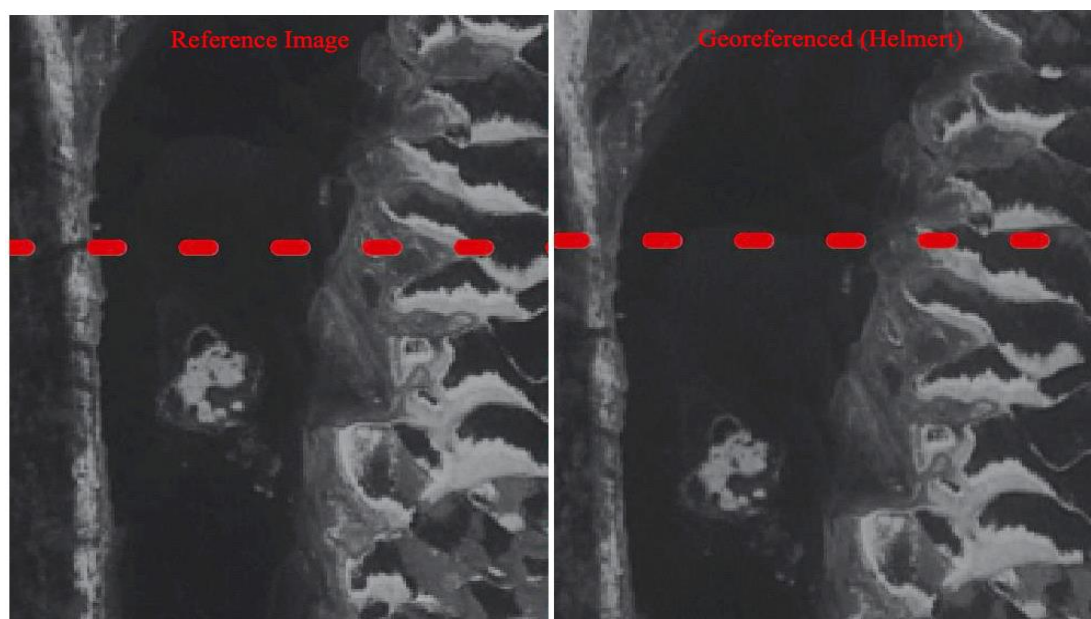


Figure 0.3 Comparison between the Reference Image and Georeferenced image (co-registration method: Helmert).

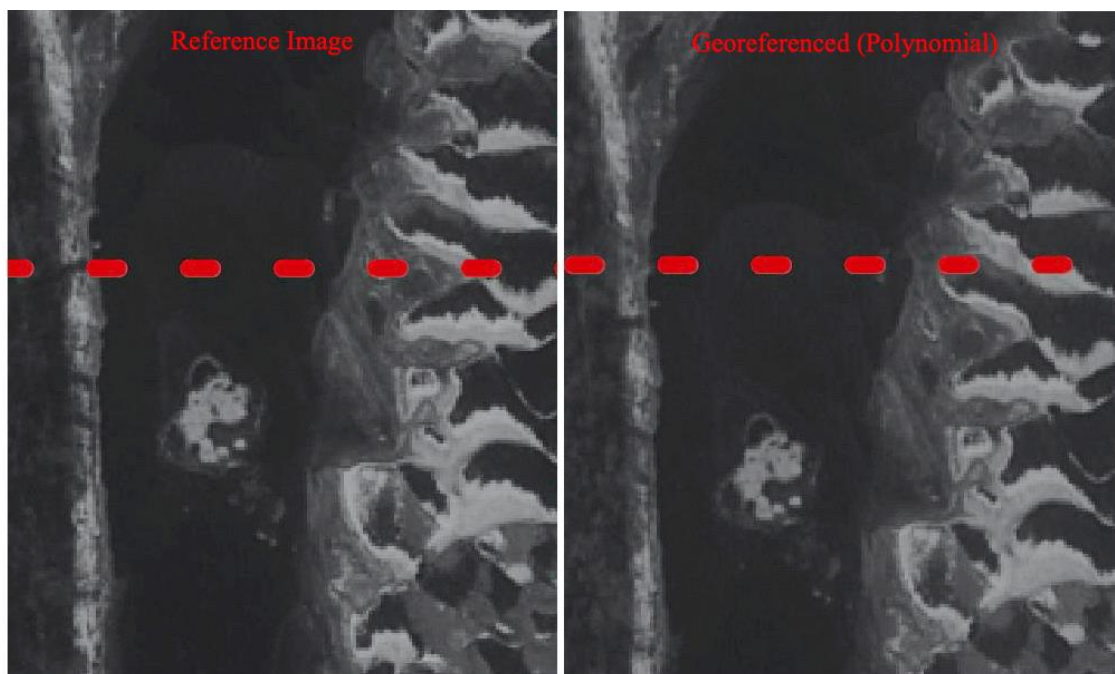


Figure A.4 Comparison between the Reference Image and Georeferenced image (co-registration method: Third-Order Polynomial).

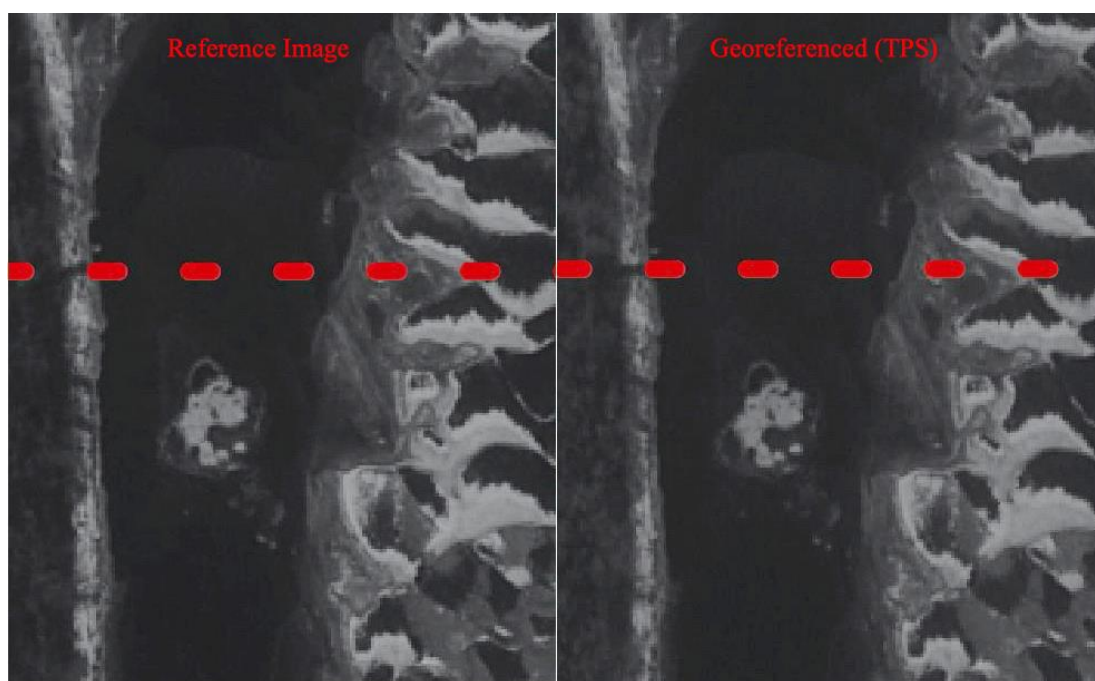


Figure 0.5 Comparison between the Reference Image and Georeferenced image (co-registration method: TPS).

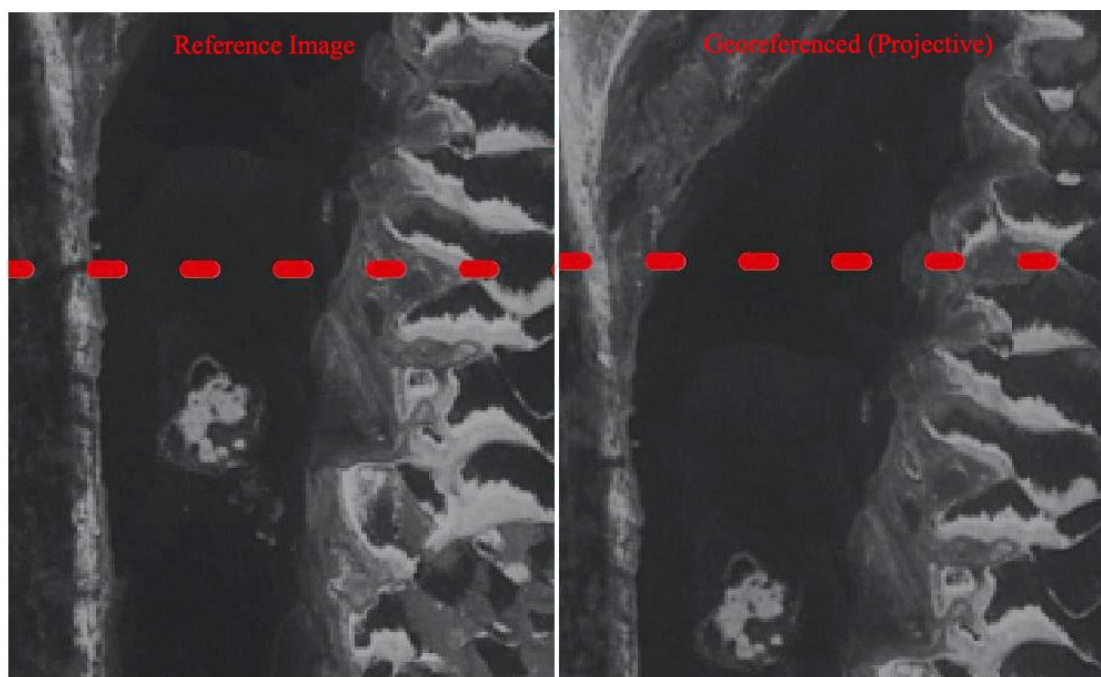


Figure A.6 Comparison between the Reference Image and Georeferenced image (co-registration method: Projective).

APPENDIX B DRY SURFACES

Here are two examples of the frozen surface on different parts of the river.

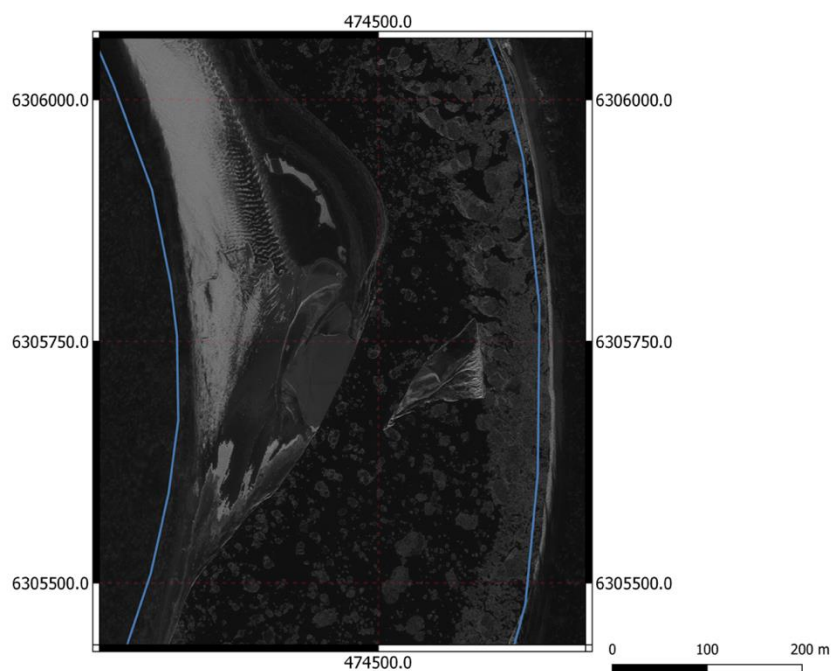


Figure 0.1 Sample of the dry surface on the left side of the section.

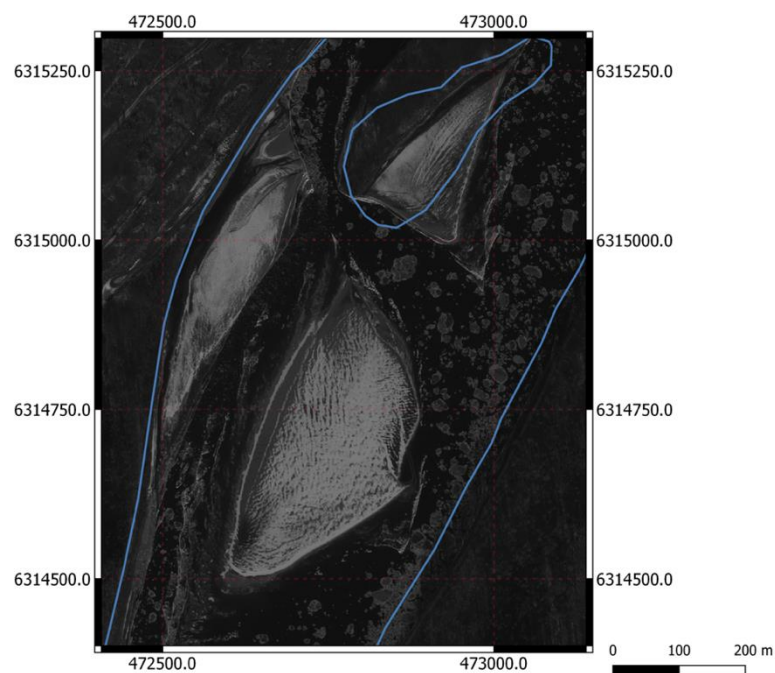


Figure B.2 Sample of the dry surface in the middle of the section.

APPENDIX C SECTION OF THE LAR IN THREE DIFFERENT TIMES OF THE YEAR



Figure C.1 Captured satellite images from a section of the Lower Athabasca River from Maxar company for a) 21 July 2009, b) 01 September 2009, and c) 11 November 2009